NOTICE

The quality of this microform is heavily dependent upon the quality of the original thesis submitted for microfilming. Every effort has been made to ensure the highest quality of reproduction possible.

If pages are missing, contact the university which granted the degree.

Some pages may have indistinct print especially if the original pages were typed with a poor typewriter ribbon or if the university sent us an inferior photocopy.

Reproduction in full or in part of this microform is governed by the Canadian Copyright Act, R.S.C. 1970, c. C-30, and subsequent amendments.

AVIS

La qualité de cette microforme dépend grandement de la qualité de la thèse soumise au microfilmage. Nous avons tout fait pour assurer une qualité supérieure de reproduction.

S'il manque des pages, veuillez communiquer avec l'université qui a conféré le grade.

La qualité d'impression de certaines pages peut laisser à désirer, surtout si les pages originales ont été dactylographiées à l'aide d'un ruban usé ou si l'université nous a fait parvenir une photocopie de qualité inférieure.

La reproduction, même partielle, de cette microforme est soumise à la Loi canadienne sur le droit d'auteur, SRC 1970, c. C-30, et ses amendements subséquents.

Finite Element Solutions of the Euler Equations in Primitive Variables Form

Guido Baruzzi

A Thesis

in

The Department

of

Mechanical Engineering

Presented in Partial Fulfillment of the Requirements
for the Degree of Master of Engineering at
Concordia University
Montréal, Québec, Canada

August 1989

ISBN 0-315-51400-0

ABSTRACT

Finite Element Solutions of the Euler Equations in Primitive Variables Form

Guido Baruzzi

Most of the current approaches to the solution of the Euler equations are based on explicit or semi-implicit time-marching schemes. These schemes suffer from poor convergence rates due to the time-step restrictions imposed by stability constraints.

In this thesis a new approach, based on solving the steady Euler equations, is presented and is shown to be a more efficient scheme to capture steady-state solutions. The scheme is constructed by adding dissipation terms, in the form of Laplacians of the solution variables, on the right-hand side of the governing equations. The residuals of the equations are minimized via the Galerkin weak form, allowing the recovery of contour integrals that yield natural boundary conditions. The finite element discretization also permits a natural approach to the extrapolation of boundary conditions necessary for hyperbolic systems, guaranteeing that the Euler equations are satisfied at the boundaries. The resulting equations are linearized by Newton's method and solved in a fully coupled manner by a direct solver to achieve quadratic convergence.

Solutions for internal and external transonic flows show that the scheme is practical and efficient. Furthermore, this thesis illustrates the non-uniqueness of the steady Euler equations by capturing multiple solutions for a class of internal flows.

ACKNOWLEDGEMENTS

The author wishes to thank his thesis supervisor, Professor W.G. Habashi for the support, guidance and patience shown during the course of this research and for providing an excellent role model to follow in the years to come. Thanks are also due to Professor M.M. Hafez, of the University of California, for his many valuable suggestions.

The author is greatly indebted to two of his colleagues: Mr. Grant Guevremont for supplying the C-grid generation program of external flows and for the many helpful discussions and Mr. Bao Nguyen of Pratt & Whitney Canada for his assistance in the preparation of the graphs for the two-dimensional results.

Finally, this thesis is dedicated to my parents Giorgio and Luciana Baruzzi who constantly provided the opportunities that made this thesis possible.

TABLE OF CONTENTS

LIST OF FIGURES

page

page

LIST OF TABLES

LIST OF SYMBOLS

$\boldsymbol{A}$	Jacobian of the 1-D and 2-D flux vector $\boldsymbol{F}$
A	Finite element surface of integration
a	Cross-sectional area of 1-D channels
$\boldsymbol{B}$	Jacobian of the 2-D flux vector $\boldsymbol{G}$
$\boldsymbol{C}$	Jacobian of the 1-D source vector $\boldsymbol{S}$
c	Speed of sound
Δt	Time increment
Δx	Space increment
e	Energy
$\boldsymbol{F}$	Flux vector in the x-direction
$\boldsymbol{G}$	Flux vector in the y-direction
γ	Specific heat ratio (constant, γ=1.4)
H_∞	Freestream total enthalpy
J	Jacobian
λ	Characteristic speed or eigenvalue
Λ	Diagonal matrix of eigenvalues
N	FEM shape function
$\bar{n}$	Normal direction
p	Pressure
q	Resultant velocity ($q^2=u^2+v^2$)
ρ	Density
$\boldsymbol{S}$	1-D souce vector
S	Finite element contour of integration

U	Variables vector
u	component of velocity in the x-direction
v	component of velocity in the y-direction
W	Characteristic variable vector
W	Weight function in Galerkin integrals
X	Matrix of eigenvectors

CHAPTER 1

1.1 Introduction

Many of the partial differential equations that govern the dynamics of physical systems do not permit an exact solution. Such solutions can only be obtained for special or simplified cases. In the engineering aerodynamics environment one deals with complex problems, consequently two different approaches can be pursued: the reliance on empirical information database gathered through experience or the development of algorithms for the numerical solution of the governing equations. Such computer simulations are becoming the norm in the aerospace industry and help reduce the development time and the investment required to produce a new aerodynamic design. The objective of these simulations is not to eliminate experimental testing but to selectively focus it, thus providing a more efficient and effective global design tool. In addition, in some engineering areas where experiments cannot be easily carried out, computer simulation provides the only way to determine the flow behavior.

Examples abound of the application of numerical codes to the design of aerodynamic shapes in the development of modern aircraft, space shuttles, missiles and the space plane. Codes developed for aerodynamics are also sometimes adapted to a variety of fields, from the design of the America's Cup winner to power and process applications.

While some numerical techniques for the approximate solution of partial differential equations were introduced before the appearance of the digital computer, it is only the power of such machines that has made possible their application to complex and practical problems. Computational Fluid Dynamics has therefore developed as a multidisciplinary endeavor between engineering, applied mathematics and computer science. It belongs to a

broad family of relatively new but growing sectors of the applied sciences that have come to maturity due the advances in the digital computer.

In the area of transonic aerodynamics, in particular, practical numerical techniques started emerging in the late '60s. Murman and Cole [1] were pioneers in the development of an upwind finite difference scheme for the solution of the Transonic Small Disturbance Equation. Their breakthrough consisted of switching from a centered stencil in subsonic regions to an upwind difference one in supersonic regions. Centered schemes allow both compression and entropy-violating expansion shocks to form during the numerical solution process. The Murman and Cole algorithm succeeded in selectively capturing compression shocks and suppressing the non-physical expansion ones, thereby handling the mixed elliptic-hyperbolic nature of the equation as the flow changes from subsonic to supersonic and vice versa. This, together with their use of a Successive Line Over Relaxation (SLOR) scheme, permitted successful transonic solutions.

Jameson [1] then showed that upwind finite difference stencils are equivalent to the combination of a central difference and a dissipation operator which resembles in nature the viscosity terms of the Navier-Stokes equations, hence the label artificial viscosity. This artificial viscosity introduces the necessary dissipation mechanism for the selective formation of compression shocks in an otherwise inviscid fluid. This concept of artificial viscosity, dissipation or upwinding, is used today, in one form or another, in all shock-capturing transonic schemes.

The numerical solution of the Full Potential Equation was the next milestone [1]. Results for arbitrary lifting transonic airfoils were obtained and subsequently the analysis of 3-D complex configurations and unsteady flows also became possible. Invariably the partial differential equations were discretized via finite difference or finite volume methods

because of the ease of shifting from central to upwind stencils between subsonic and supersonic regions of the flow.

1.2 Limitations of the Full Potential Equation

The Full Potential Equation has been recently shown to yield multiple solutions for certain ranges of Mach number and angles of attack for external transonic flows. This non-uniqueness problem, analyzed in detail by Salas, Jameson and Melnik [2], is attributable to the incomplete shock-jump conditions of the Full Potential Equation. It can be circumvented either by explicitly correcting the total pressure downstream of the shock, or by solving an additional Poisson equation for pressure, as proposed by Hafez et al. [3] and Habashi et al. [4].

For internal flows the Full Potential Equation suffers equally from non-uniqueness [4]. For choked flow in a nozzle, for example, purely isentropic exit flows are the only possible solutions. Should a shock form somewhere in the nozzle, its position would be arbitrary because its strength cannot affect the back pressure. Habashi et al. [4] resolved this difficulty by modifying the classical imposition of boundary conditions for internal choked flows. Their method, known as the Modified Potential, specifies an arbitrary value of the potential at the exit to produce intermediate choked solutions which, after calculating the proper total pressure loss across the shock, may not lead to the target back pressure. Successive corrections of this exit potential value are made until the desired back pressure is reached. The method has found application in supersonic choked turbomachinery

The Full and Modified Potentials are nevertheless irrotational models and do not account for the entropy generated downstream of strong curved shocks. An alternative is the Euler equations, solved either in primitive variables or in stream function forms. The latter is

attractive from the point of view of exact mass conservation, but suffers from the double-valuedness of the density vs mass flux for a given Mach number. It has been developed for external and internal transonic flows, for both finite differences [5] and finite elements [6], its extension to 3-D is not simple.

1.3 The Euler Equations

The introduction illustrated the current interest in the solution of the Euler and, consequently, of the Navier-Stokes equations. The Reynolds-Averaged Navier-Stokes equations describe the physics of viscous fluid flows, but their numerical solution was considered impractical until recently because of the large computer memory requirements associated with the solution of systems of equations in several variables and the fine grids necessary to accurately resolve the boundary layer regions. The Euler equations in primitive variables form, a system of quasi-linear hyperbolic equations, are the subset of the Navier-Stokes equations obtained by neglecting the viscous terms. Although no fluid can be really considered inviscid, the Euler equations provide a reasonable, but by no means complete, estimate of the behavior of a fluid when the Reynolds number becomes very large. Their numerical solution is an interesting and challenging problem en route towards the development of efficient schemes for the Navier-Stokes equations.

Since efficient elliptic solvers had already been developed for the solution of the Full Potential equation, hyperbolic algorithms for the Euler equations became the focus of very intense research efforts. Of the many computational schemes developed, three have become quite popular: the time-explicit Lax-Wendroff [7] and Jameson [8] schemes and the time-implicit, finite difference variation of the factored Beam and Warming [9] scheme attributable to Pulliam and Steger [10]. These schemes, based on the unsteady form of the equations, substitute time-marching procedures for the iterative process. Both the explicit

and implicit algorithms have slow convergence rates and require additional techniques to achieve reasonable computational efficiency. Nevertheless good results have been obtained for wing, wing-body combinations and entire aircraft with these techniques.

1.4 The Finite Element Method and High-Speed Computational Fluid Dynamics

The finite element method is known to be suited to problems involving irregular domains. For many years it has been the method of choice for the structural analysis of complex configurations but is still largely underdeveloped by the North American CFD community in spite of several important successes, especially among the Europeans.

The finite element method is based on the subdivision of the solution domain into a finite number of smaller regions, or elements. In each element a polynomial representation of the function(s) to be solved for is assumed. A minimization procedure, usually of the weighted residual type, discretizes the partial differential equations into a set of algebraic equations or ordinary differential equations. As the mesh is refined, the size of the elements becomes small and the approximate solution approaches the exact solution. The main advantages of the finite element method are:

- it does not require a global topological mapping to transform a complex domain into a regular form,
- it is based on a Weighted Residual formulation of the governing partial differential equations for which a minimum or a maximum can be identified,
- the approach generally yields physically relevant boundary conditions, easy to implement,

- a library of progressively sophisticated elements can be easily included in a computer code,
- Different variables may have different levels of interpolation over the same element, similar to the use of a staggered grid,
- it has a more implicit stencil than finite difference or finite volume because more grid points are connected together.

The classical approach in the finite element method requires the simultaneous solution of all the nodal unknowns in the field and hence is associated with the solution of large systems of equations. Memory limitations have therefore constituted one of the strongest objections to the use of this method. However, modern approaches have shown that it can be used with no difficulty in implicit, semi-implicit or even fully explicit manner.

Although the finite element method is generally based on symmetric operators, upwinding can be introduced at the expense of simplicity. Symmetric operators are optimal for the discretization of second-order partial differential equations like the Potential or the stream function, but first-order hyperbolic wave equations require either upwind-biased operators or the addition of artificial viscosity terms in the governing equations. The FEM simulation of transonic Potential flows with shocks became practical only with the application of the concept of artificial compressibility, an upwind correction of the density that is similar to an artificial viscosity, details of which are given in Ref. [3] and [4].

A successful finite element formulation of the Euler equations in primitive variables form can be considered a useful CFD tool. The Least-Squares scheme of Fletcher [11] for the solution of the steady Euler equations in primitive variables was perhaps among the first attempts at a finite element simulation of the hyperbolic system of equations. The extension of this solution to transonic flows was not attempted, however, for the absence of artificial

viscosity in the formulation. This formulation is quite novel because groups of variables, not single variables, are the unknowns.

Donea [12] analyzed several explicit time stepping schemes for the Euler equations and found that Taylor series expansions of the time derivatives were suitable for Galerkin FEM formulations. Löhner, Morgan and Zienkiewicz [13] extended one of the Taylor-Galerkin schemes of Donea, derived from the Lax-Wendroff scheme, to transonic flows by adding an artificial viscosity term and showed that it can be reduced to a characteristics scheme. Unfortunately, as it will be shown, this scheme does not provide a consistent set of boundary conditions even if its weak formulation is considered.

Angrand et al. [14] devised a time-explicit scheme with triangular finite elements. This weighted residual subdomain scheme is equivalent to a finite volume method because the weight function is unity and the integration is performed assuming lumped-mass elements. It will be shown in Chapter 3 of this thesis that the set of boundary conditions provided by the authors is inconsistent with the density boundary conditions on solid boundaries. Stoufflet [15] improved this method by extending it to second-order accuracy and by showing that an entire family of implicit and explicit schemes can be obtained from it.

Tezduyar and Hughes [16] have developed the Petrov-Galerkin formulation to construct streamline-upwind FEM schemes for the Euler equations, but their scheme is cumbersome as a result of the complications introduced by the upwind formulation.

Akay and Ecer [17] have explored the Clebsch transformation of the primitive variables to convert the Euler equations from first to second order. The Clebsch formulation advocates replacing the original variables with new ones, thereby reducing the size of the system of partial differential equations and reducing the computational effort, however special considerations must be made for rotational regions in the flow. In these regions the

velocity Potential part of the Clebsch formulation is no longer valid and must be replaced by a non-isentropic Potential which is not strictly consistent.

Bruneau, Laminie and Chattot [18] have studied vortex flows over delta wings through a finite element variational approach based on the least-squares weighted residual method and the Newton linearization. Similar to Fletcher they have not introduced any artificial viscosity and are hence limited to smooth flows without shocks. Moreover, their scheme does not yield a set of natural boundary conditions and is cumbersome to implement. One of their interesting conclusions is that the Euler equations, although inviscid, support separation in the case of vortex flow over delta wings even without the help of numerical dissipation.

1.5 Thesis Outline

The focus of this thesis is threefold. First, a comparison of several 1-D schemes is conducted to show that the use of time-marching explicit or implicit schemes for the steady-state solution is unnecessary and that a more efficient scheme can be constructed directly from the steady Euler equations via a Newton Method. This formulation is capable of handling any regime of flow, from incompressible to supersonic, with the convergence rate independent of the minimum mesh size.

The second part focuses on the methodology of developing a finite element algorithm for the Euler equations. The proposed finite element scheme shows no particular difficulties for steady-state hyperbolic systems of equations and presents some distinct benefits in the implementation of boundary conditions.

While a mathematical confirmation that the steady 2-D Euler equations, or for that matter the Potential equation, should yield unique solutions in the presence of a discontinuity

[19,20] has still not appeared, the third contribution of this thesis is to demonstrate non-unique solutions of the steady Euler equations for a particular class of 2-D transonic internal flows.

CHAPTER 2

2.1 1-D Explicit and Implicit Schemes for the Unsteady Euler Equations

The numerical solution of the compressible Euler equations in primitive variables, time-dependent conservation form is considered to be one of the classical problems of CFD. The need for primitive variables Euler algorithms arises from the various limitations of the simpler formulations, like the potential or the stream function approaches, which are unsuitable for modelling rotational problems.

The apparent simplicity of the compressible Euler equations belies their coupled, quasi-linear hyperbolic nature, therefore the construction of their numerical approximations must account for these factors, particularly in the treatment of the boundary conditions. Even though the equations can be written in conservative or non-conservative form, for flows with shocks the numerical scheme must be based on the conservative form to account for the correct shock-jump conditions.

Several explicit and implicit methods have been developed and among them one can cite the schemes of Lax-Wendroff, MacCormack, Jameson, Beam and Warming, Steger and Pulliam. These algorithms are based on Finite Difference or Finite Volume methods and take advantage of the characteristics of the hyperbolic system of equations by upwind differencing, while the Finite Element Method has lagged somewhat behind for its lack of such capability.

In this chapter a comparative analysis of four Euler schemes is conducted. The schemes are the explicit Taylor-Galerkin scheme, the two implicit methods of Lerat and the steady-state Newton scheme. All schemes are implemented in a finite element manner, although

the Lerat schemes had never been discretized that way before. The first three schemes are time-marching while the Newton method tackles the steady-state form of the equations.

It will be shown that a very large number of iterations (2500-8000) is required for reasonable convergence to steady-state for the explicit scheme and that Lerat's two methods are more efficient in terms of convergence rates and elapsed CPU times, even though they require more work and storage per iteration. Furthermore, it will be demonstrated that the time-marching schemes cannot compete with the Newton method in terms of convergence rates, CPU times and range of applicability. The convergence rate of the time-dependent schemes is a function of the minimum mesh size, while the Newton method is independent of it. Moreover the steady-state form of the Euler equations is applicable to the solution of any flow regime while the time-dependent form of the equations is overdetermined for incompressible flows, unless it is recast in a form that does not contain density as one of the dependent variables.

2.2 Quasi 1-D Isothermal Form of the Euler Equations

The isothermal case, although not likely to occur naturally, was chosen as a test case because it consists of only two equations, a considerable simplification compared to the three partial differential equations and the algebraic pressure equation of the general case. The procedures developed in this section are, however, generally valid for inviscid conservation laws.

The system of inviscid conservation laws can be stated in vector form as:

$$\frac{\partial U}{\partial t}+\frac{\partial F}{\partial x}=S \tag{2.1}$$

or in quasi-linear vector form as:

$$\frac{\partial U}{\partial t}+A\frac{\partial U}{\partial x}=S \tag{2.2}$$

where:

$$U=\begin{bmatrix} \rho a \\ \rho a u \end{bmatrix} \qquad F=\begin{bmatrix} \rho a u \\ \rho a(c^2+u^2) \end{bmatrix} \qquad S=\begin{bmatrix} 0 \\ \rho c^2 \frac{da}{dx} \end{bmatrix}$$

and

$$A=\frac{\partial F}{\partial U}=\begin{bmatrix} 0 & 1 \\ c^2-u^2 & 2u \end{bmatrix} \qquad C=\frac{\partial S}{\partial U}=\begin{bmatrix} 0 & 0 \\ \frac{c^2}{a}\frac{da}{dx} & 0 \end{bmatrix}$$

The system is hyperbolic if the Jacobian matrix A has real eigenvalues; the set of inviscid gas dynamics equations always satisfies this condition. The eigenvalues of A in the present case are:

$$\lambda_1 = u + c \qquad \lambda_2 = u - c$$

The eigenvalues of the equations of gas dynamics are also called characteristic speeds, or simply characteristics, and have a physical meaning: they represent the velocity of propagation (or convection) of the signals along the coordinate directions. It should be noted that the number of characteristics is always equal to the number of dependent variables, although each characteristic is not necessarily linked to any specific variable.

2.3 The Hyperbolic Nature of the Equations and its Implications

The hyperbolic nature of the Euler equations must be examined in detail before attempting to derive a new scheme or explain the construction of an existing one. The numerical treatment of systems of hyperbolic equations is fundamentally different from that of elliptic

equations: the Euler equations are a set of first-order wave equations and exhibit a series of features common to wave equations. In particular, the mathematical model of the equations shows that disturbances in the flow appear in the form of non-linear waves and that any disturbance is convected away from its source with at most m distinct characteristic wave speeds, where m is the number of partial differential equations under consideration. In addition, the waves are subject to all the phenomena associated with other wave models, like absorption, diffraction and reflection.

Suppose that the same smooth subsonic flow (no shocks) has to be solved using a scheme based on the Potential and one based on the primitive variables form. Both will produce the same results within a small numerical error for the same sample problem, however the treatment of the boundary conditions will be completely different from one scheme to the other because the Potential approach does not support the wave-like nature of the Euler equations.

For primitive variables formulations the numerical treatment of the solution schemes and their boundary conditions must be consistent not only with the physics of the flow itself but also with the wave-like nature of the equations. Pulliam [21], Chakravarthy [22] and Yee, Beam and Warming [23] provide an excellent discussion of the boundary treatment methods. Note that in the case of the Euler equations the number of boundary conditions required by the discrete approximation is always higher than the number of analytical (or Dirichlet) boundary conditions. Some of the variables cannot be determined a priori on certain boundaries, therefore the additional numerical boundary conditions required to completely define the system of equations on the boundary are generally obtained by extrapolating some quantities from the interior of the solution domain.

Consider the four different cases that can arise at the boundaries if the single-element solution domain of Fig. 1 is examined. The arrows in the time-space Cartesian coordinates

represent the disturbances coming from the solution at previous time levels and terminating at the boundary nodes at time t. When the two converging characteristics have opposite signs the flow is subsonic and when they have equal signs the flow is supersonic, since λ_1 is always positive and λ_2 is negative for $u < c$. Case (a) represents an element completely embedded in a subsonic region, case (b) is an element extending through a subsonic-supersonic transition interface, case (c) is an element embedded in a supersonic region and case (d) is an element extending through a supersonic-subsonic transition zone.

Referring to case (a) one notes that at node I one characteristic is coming from outside (+ve), the other (-ve) from inside the solution region. The positive characteristic carries information from the outside to the boundary of the element, while the negative one carries information to the boundary from within the solution domain. The conditions existing outside the solution region must be known a priori, hence one of the two variables must be constrained at node I, but since the characteristics are not related to any variable in particular, either of the solution variables ρa or $\rho a u$ can be specified. At this stage the positive characteristic will be arbitrarily associated with the particular variable that has been constrained. The other characteristic being (-ve) reaches node I from inside the solution region and carries all the information necessary to determine the second variable by extrapolation from the previous time level or from the nearest adjacent internal point: the value of that variable must be allowed to float. Node E can be treated in the same manner but with the order of the variables reversed. For subsonic flow two possibilities are therefore available: either the density may be specified at node I and the mass flow at node E, or vice-versa, and the solutions would be identical. The advantage of a FEM over other discrete methods is that at the boundaries no explicit extrapolation is required since all variables have a continuous representation through the element shape functions.

As a rule, the number of Dirichlet boundary conditions is the same as the number of characteristics coming from the outside of the solution region. In case (b), one boundary

condition is specified at node I and no boundary conditions at node E. In case (c), two are specified at node I, none at node E. Finally for case (d), two boundary conditions are specified at node I and one at node E. For transonic isothermal flows the only possibility is to constrain the mass-flow at node I and the density at node E.

In order to verify that the boundary conditions are mathematically well-posed it must be shown that they satisfy the partial differential equation. Consider the following transformation which always exists for the conservation laws of gas dynamics:

$$\Lambda_A = X^{-1} A X \tag{2.3}$$

where:

$$\Lambda_A = \begin{bmatrix} u+c & 0 \\ 0 & u-c \end{bmatrix} \qquad X = \begin{bmatrix} 1 & 1 \\ u+c & u-c \end{bmatrix} \qquad X^{-1} = \frac{1}{2c}\begin{bmatrix} c-u & 1 \\ c+u & -1 \end{bmatrix}$$

Λ_A is known as the diagonal matrix of the eigenvalues of A, while X is the matrix of the eigenvectors of A. Eq. (2.1) can be rewritten in the form:

$$\frac{\partial U}{\partial t} + X\Lambda_A X^{-1}\frac{\partial U}{\partial x} = S \tag{2.4}$$

After further simplification Eq. (2.4) is transformed into:

$$X^{-1}\frac{\partial U}{\partial t} + \Lambda_A X^{-1}\frac{\partial U}{\partial x} = X^{-1} S \tag{2.5}$$

Defining:

$$\frac{\partial Q}{\partial U} = X^{-1}$$

and applying the chain rule to Eq. (2.5), one obtains:

$$\frac{\partial Q}{\partial t} + \Lambda_A \frac{\partial Q}{\partial x} = X^{-1} S \tag{2.6}$$

Expressed in this form the system of equations is uncoupled and to each variable in Q is associated one of the characteristics, but the reader should remember that this correspondence is purely arbitrary since the diagonal elements of the eigenvalues matrix Λ_A can be distributed in any order. The variables in $Q = (Q_1, Q_2)^T$ are the characteristic variables.

The boundary conditions are of the type:

$$Q(U)=0 \qquad \text{or} \qquad \frac{\partial Q}{\partial t}=\frac{\partial Q}{\partial U}\frac{\partial U}{\partial t}=0$$

All known quantities will now be identified with a superscript K and the unknown ones with UK. In this case assume that ρa, now linked to the characteristic $u + c$, is specified at node I and ρua at node E as in case (a) discussed above, then:

$$Q_I^K=\begin{bmatrix} 0 \\ \rho au \end{bmatrix} \qquad\qquad Q_E^K=\begin{bmatrix} \rho a \\ 0 \end{bmatrix}$$

whose Jacobians with respect to the original variables vector are:

$$H_I^K=\frac{\partial Q_I^K}{\partial U}=\begin{bmatrix} 0 & 0 \\ 0 & 1 \end{bmatrix} \qquad H_E^K=\frac{\partial Q_E^K}{\partial U}=\begin{bmatrix} 1 & 0 \\ 0 & 0 \end{bmatrix}$$

$H_I{}^K$ and $H_E{}^K$ are the contributions from the boundary conditions to $X_I{}^{-1}$ and $X_E{}^{-1}$ respectively. The matrices $H_I{}^{UK}$ and $H_E{}^{UK}$ are defined at the boundaries as:

$$H_I^{UK}=\frac{1}{2c}\begin{bmatrix} c-u & 1 \\ 0 & 0 \end{bmatrix} \qquad H_E^{UK}=\frac{1}{2c}\begin{bmatrix} 0 & 0 \\ c+u & -1 \end{bmatrix}$$

The total contributions at the boundaries are the sum of the Dirichlet ($H_I{}^K$ and $H_E{}^K$) and the inverse eigenvector matrices ($H_I{}^{UK}$ and $H_E{}^{UK}$):

$$X_I^{-1} = H_I^K + H_I^{UK} = \begin{bmatrix} \frac{c-u}{2c} & \frac{1}{2c} \\ 0 & 1 \end{bmatrix} \qquad X_E^{-1} = H_E^K + H_E^{UK} = \begin{bmatrix} 1 & 0 \\ \frac{c+u}{2c} & -\frac{1}{2c} \end{bmatrix}$$

At the boundaries Eq. (2.5) must be rewritten as:

$$X_{IE}^{-1}\frac{\partial U}{\partial t} + \Lambda_A X_{IE}^{-1}\frac{\partial U}{\partial x} = X_{IE}^{-1} S \tag{2.7}$$

For the boundary conditions to be well-posed it is sufficient to show that X^{-1} exists, or that the determinant of X is non-zero so that Eq. (2.4) can be recovered. This can be readily verified by inspection, therefore showing that extrapolation at the boundary is a valid method of introducing some of the boundary conditions.

2.4 The Lax-Wendroff Scheme

The solution of hyperbolic systems of equations is traditionally obtained through time-marching algorithms. The Taylor-Galerkin[13] explicit scheme is an example of an explicit time-marching algorithm based on the one-step Lax-Wendroff[12] method. The scheme can be constructed by forming a Taylor series of the evolution of the solution through time. Thus:

$$U^{n+1} = U^n + \Delta t\frac{\partial U^n}{\partial t} + \frac{\Delta t^2}{2!}\frac{\partial^2 U^n}{\partial t^2} + \frac{\Delta t^3}{3!}\frac{\partial^3 U^n}{\partial t^3} + \ldots \tag{2.8}$$

The kth order derivatives:

$$\frac{\partial^k U^n}{\partial t^k} \qquad k=1,2,\ldots,\infty$$

can be obtained by rearranging Eq. (2.1). For example, the first order derivative (k=1) is:

$$\frac{\partial U^n}{\partial t} = \left(S - \frac{\partial F}{\partial x}\right)^n \tag{2.9}$$

Substituting Eq. (2.9) and the second-order derivative terms into Eq. (2.8) and setting

$$\Delta U^n = U^{n+1} - U^n$$

The Lax-Wendroff scheme can be written in the form:

$$\Delta U^n = \Delta t\left(S - \frac{\partial F}{\partial x}\right)^n + \frac{\Delta t^2}{2}\left[C\left(S - \frac{\partial F}{\partial x}\right) - \frac{\partial}{\partial x}\left[A\left(S - \frac{\partial F}{\partial x}\right)\right]\right]^n + O[\Delta t^3] \qquad (2.10)$$

The variables are uncoupled in ΔU^n, therefore the problem is reduced to the solution of two (three for the general isentropic case) tridiagonal matrices which need to be assembled and decomposed only once since the left-hand side of Eq. (2.10) is linear. Furthermore, Löhner, Morgan and Zienkiewicz[13] have shown that Eq. (2.10) can be derived by applying the method of characteristics to Eq. (2.1); the Lax-Wendroff scheme can then be called a characteristics modelling scheme. Assuming that the matrix A has constant coefficients, the linear stability analysis of Eq. (2.10) conducted by Löhner, Morgan and Zienkiewicz [13] shows that the scheme is conditionally stable for

$$C = \rho_A \frac{\Delta t}{\Delta x} \leq \frac{1}{\sqrt{3}}$$

where C is the Courant number and ρ_A is the largest eigenvalue, or spectral radius, of A.

2.5 The Taylor-Galerkin Scheme

The Taylor-Galerkin scheme is the Finite Element equivalent of the Lax-Wendroff scheme. Let any variable Φ be represented in its discrete form as:

$$\Phi = \sum_j \hat{\Phi}_j N_j \qquad (2.11)$$

where the subscript j indicates the element nodes local numbers, $\hat{\Phi}_j$ is the numerical value of Φ at the element nodes and N_j represents the shape functions. For linear 1-D elements (j=1,2) the dimensional shape functions are written as:

$$N_1 = \frac{x_2 - x}{x_2 - x_1} \qquad\qquad N_2 = \frac{x - x_1}{x_2 - x_1}$$

where the subscripts 1 and 2 denote local numbering of the nodes of the elements. A sketch of the shape functions is shown in Fig. 2.

The Galerkin principle is based on the minimization of the residue of the discrete equations. It belongs to the family of weighted residual methods and it is the most compact form, having weights identical to the shape functions. Denoting the solution domain, subdivided into finite elements, with A and its boundary with S, the Galerkin approach states that:

$$\int_A W_i \, [R] \, dA = 0 \tag{2.12}$$

where W_i is the weight function and R is the residual of the discrete equations. Applying the Galerkin principle to Eq. (2.10) yields the following integral:

$$\int_A W_i \Delta U^n dx = \int_A W_i \left\{ \Delta t \left(S - \frac{\partial F}{\partial x} \right)^n + \frac{\Delta t^2}{2} \left[C \left(S - \frac{\partial F}{\partial x} \right) - \frac{\partial}{\partial x} \left[A \left(S - \frac{\partial F}{\partial x} \right) \right] \right]^n \right\} dx \tag{2.13}$$

The last term in the RHS of Eq. (2.13) can be integrated by parts and the equation can be cast in the form:

$$\sum_{j=1}^{df} [M_{i,j}] \Delta \hat{U}_j = \Delta t \sum_j \{\hat{R}_j\}_i + \frac{\Delta t^2}{2} \sum_j \{\hat{T}_j\}_i \tag{2.14}$$

where:

$$[M_{i,j}] = \sum_j \int_A W_i N_j \, dx$$

$$\{\hat{R}_j\}_i = \int_A W_i \left(\hat{S}_f N_j - \hat{F}_f \frac{\partial N_j}{\partial x} \right)^n dx$$

$$\{\hat{T}_j\}_i = \sum_k \int_A \left\{ W_i \left[\hat{C}_k N_k \left(\hat{S}_f N_j - \hat{F}_f \frac{\partial N_j}{\partial x} \right) \right]^n + \left[\hat{A}_k N_k \left(\hat{S}_f N_j - \hat{F}_f \frac{\partial N_j}{\partial x} \right) \frac{\partial N_i}{\partial x} \right]^n \right\} dx$$

where $[M]$ is the local mass matrix, $\{\Delta U\}$ is the vector of unknowns and $\{R\}$ and $\{T\}$ form the RHS.

2.6 Artificial Viscosity for the Taylor-Galerkin Scheme

No meaningful solutions can be obtained for transonic flow from the Taylor-Galerkin scheme without the addition of an artificial viscosity, or dissipation, term. Augmenting Eq. (2.1) as:

$$\frac{\partial U}{\partial t} + \frac{\partial F}{\partial x} = S + \frac{\partial}{\partial x}\left(\mu \frac{\partial U}{\partial x} \right) \tag{2.15}$$

introduces a dissipation term in conservation form, required to ensure the correct shock-jump conditions and therefore the correct shock location. Performing the same procedure outlined for the Lax-Wendroff and Taylor-Galerkin scheme yields:

$$[M]\{\Delta U\} = \{R\} + \{T\} - C_v \Delta t \int_A \Delta x^2 \left| \frac{\partial u}{\partial x} \right| \frac{\partial U}{\partial x} \frac{\partial W_i}{\partial x} dx \tag{2.16}$$

where C_v is the dissipation coefficient. Since the system of equations is hyperbolic, this type of artificial viscosity must be applied throughout the solution domain, as opposed to Potential flow solvers where the artificial viscosity can be confined to supersonic regions.

2.7 Lerat's Implicit Methods

Lerat's methods [24] are predictor-corrector schemes based on an implicit correction of the truncation error of Eq. (2.13). A slight modification of Eq. (2.13) yields the predictor step:

$$\Delta W=\Delta t\left(S-\frac{\partial F}{\partial x}\right)^n+\frac{\Delta t^2}{2}\left[C\left(S-\frac{\partial F}{\partial x}\right)-\frac{\partial}{\partial x}\left[A\left(S-\frac{\partial F}{\partial x}\right)\right]\right]^n+O[\Delta t^3] \qquad (2.17)$$

The coupled implicit corrector step can be constructed from the truncation error of Eq. (2.17) – with the assumption that the source term S and its Jacobian C can be neglected – as follows:

$$O[\Delta t^3]=\frac{\Delta t^3}{3!}\frac{\partial}{\partial t}\left[C\left(S-\frac{\partial F}{\partial x}\right)-\frac{\partial}{\partial x}\left[A\left(S-\frac{\partial F}{\partial x}\right)\right]\right]\approx\frac{\Delta t^3}{3!}\frac{\partial}{\partial x}\left[A^2\frac{\partial}{\partial x}\left(\frac{\Delta U}{\Delta t}\right)\right] \qquad (2.18)$$

Therefore the corrector step will assume the form:

$$\Delta U+\beta\frac{\Delta t^2}{2}\frac{\partial}{\partial x}\left[A^2\frac{\partial}{\partial x}(\Delta U)\right]=\Delta W \qquad (2.19)$$

Eqs. (2.17) and (2.19) form Lerat's coupled implicit method; note that the Eqs. (2.19) are fully coupled and therefore must be assembled and decomposed at each iteration.

Lerat's linear stability analysis shows that the scheme is conditionally stable for $\beta \le -1/2$, therefore no restrictions are imposed on the time step; the fastest convergence rate is obtained by setting $\beta = -1$. The corrector step can be modified as follows:

$$\Delta U+\beta\frac{\Delta t^2}{2}\frac{\partial}{\partial x}\left[\rho_A^2\frac{\partial}{\partial x}(\Delta U)\right]=\Delta W \qquad (2.20)$$

where ρ_A is the spectral radius of A.

Eqs. (2.17) and (2.20) form Lerat's uncoupled scheme. Even though in this case Eqs. (2.20) are uncoupled, the left-hand sides are non-linear and must be assembled and

decomposed at each iteration. The scheme follows the same stability requirements of the coupled method, however the fastest convergence rate is now obtained by setting $\beta = -1/2$.

No explicit artificial viscosity terms are required in transonic cases for the uncoupled scheme, but no meaningful solutions can be obtained in transonic cases for the coupled scheme without such terms. A heuristic explanation for the upwinding effect of Eq. (2.20) is based on the theory of characteristics: the spectral radius $u + c$ in Eq. (2.20) acts as a filter by permitting only the propagation speed of the waves coming from upstream while all downstream contributions are filtered out. Eqs. (2.20), on the other hand, allows all wave speeds to influence the solution and no upwinding is produced.

Eq. (2.17) is treated in the same manner of Eq. (2.13), replacing ΔU by ΔW. Applying the Galerkin principle to Eq. (2.19) and (2.20) and successively discretizing yields respectively:

$$\sum_{j=1}^{df}\left[[M_{i,j}] - \beta\frac{\Delta t^2}{2}[E^A_{ij}] \right]\Delta\hat{U}_j = \sum_{j=1}^{df}[M_{i,j}]\Delta\hat{W}_j \tag{2.21}$$

$$\sum_{j=1}^{df}\left[[M_{i,j}] - \beta\frac{\Delta t^2}{2}[E^\rho_{ij}] \right]\Delta\hat{U}_j = \sum_{j=1}^{df}[M_{i,j}]\Delta\hat{W}_j \tag{2.22}$$

where:

$$[E^A_{ij}] = \sum_{j=1}^{df}\int_A (\hat{A}_k N_k)^2 \frac{\partial N_j}{\partial x}\frac{\partial W_i}{\partial x}dx$$

$$[E^\rho_{ij}] = \sum_{j=1}^{df}\int_A (\hat{\rho}_{A_k} N_k)^2 \frac{\partial N_j}{\partial x}\frac{\partial W_i}{\partial x}dx$$

Since Lerat's method is not based on an approximate factorization of the Lax-Wendroff scheme, the boundary conditions are the same for both the predictor and the corrector terms.

2.8 Steady-State Euler Equations

Traditionally the approach to the solution of the Euler equations has been based on the unsteady form of the equations, essentially because the unsteady term permits to solve easily for all the dependent variables and to construct simple explicit schemes. Most of the implicit schemes devised to date, on the other hand, must avail themselves of some clever linearization of the flux terms which conserves a certain degree of coupling among the equations, complicating the assembly of the discretized equations.

If the steady-state solution is the goal, the most efficient approach consists of solving the steady Euler equations. The hyperbolic nature of the equations is retained even after the unsteady terms are discarded and the boundary conditions follow the same guidelines set for the time-dependent equations, but now the variables vector $\boldsymbol{U}$ will not be used and the flux vectors can be linearized directly.

To study this approach, consider the following set of isentropic partial differential equations:

$$\frac{\partial}{\partial x}(\rho a u)=0 \tag{2.23a}$$

$$\frac{\partial}{\partial x}(\rho a u^2+p a)-p\frac{da}{dx}=0 \tag{2.23b}$$

Assuming that the total enthalpy (H_∞) is conserved, the energy equation can be written in the form:

$$p=\frac{\gamma-1}{\gamma}\rho\left(H_\infty-\frac{u^2}{2}\right) \tag{2.23c}$$

Eqs. (2.23) are the steady Euler equations with the assumption of constant total enthalpy. This form is valid only if no work and heat are produced.

A finite element discretization of these equations produces a type of scheme based on central operators which are not suitable for the solution of transonic flows with shocks, hence a conservative artificial viscosity term must be introduced explicitly in each partial differential equation, much like the term introduced in Eqs. (2.15).

$$\frac{\partial}{\partial x}(\rho a u) = \mu \frac{\partial^2 \rho}{\partial x^2} \tag{2.24a}$$

$$\frac{\partial}{\partial x}(\rho a u^2 + p a) - p \frac{da}{dx} = \mu \frac{\partial^2 u}{\partial x^2} \tag{2.24b}$$

Eqs. (2.24) will be accurate to second order almost everywhere except near regions with steep gradients. The constant μ controls the amount of dissipation, therefore the solution of the two equations will be more accurate when μ is a minimum. Before proceeding further in the development of the Newton scheme, it is beneficial to rewrite Eqs. (2.24) in non-dimensional form with respect to ρ_∞, U_∞ and L, respectively the free-stream fluid density and velocity and a characteristic length, such as the length of a nozzle. The system of equations can then be written in the form:

$$\frac{\partial}{\partial x}(\rho a u) = \nu_1 \frac{\partial^2 \rho}{\partial x^2} \tag{2.25a}$$

$$\frac{\partial}{\partial x}(\rho a u^2 + p a) - p \frac{da}{dx} = \nu_2 \frac{\partial^2 u}{\partial x^2} \tag{2.25b}$$

$$p = \frac{\gamma - 1}{\gamma} \rho \left(H_\infty - \frac{u^2}{2} \right) \tag{2.25c}$$

where:

$$\nu_1 = \frac{\mu}{U_\infty L^3} \qquad \nu_2 = \frac{\mu}{\rho_\infty U_\infty L^3}$$

The quantities ν_1 and ν_2 are the viscosity coefficients in non-dimensional form: their optimal value is of the order of $\Delta x/2$. In the following derivations all the variables are in non-dimensional form.

2.9 The Euler Newton-Galerkin Method

The Galerkin principle, Eq. (2.12), is applied individually to the continuity and x-momentum equations as follows:

$$\int_A W_i \left[\frac{\partial}{\partial x}(\rho a u) - \nu_1 \frac{\partial^2 \rho}{\partial x^2} \right] dx = 0 \tag{2.26a}$$

$$\int_A W_i \left[\frac{\partial}{\partial x}(\rho a u^2 + p a) - p \frac{da}{dx} - \nu_2 \frac{\partial^2 u}{\partial x^2} \right] dx = 0 \tag{2.26b}$$

After all terms are integrated by parts, the contour integrals will be neglected inside the solution domain A, i.e. between adjacent elements and will be accounted for only at the boundary S of the solution domain A. The formulation is now called a "weak" formulation because strict conservation of the fluxes at the interior element nodes is automatically satisfied.

The weak formulation of Eqs. (2.26) can be written in the form:

$$[W_i (\rho a u)]_S - \int_A (\rho a u) \frac{\partial W_i}{\partial x} dx + \nu_1 \int_A \frac{\partial \rho}{\partial x} \frac{\partial W_i}{\partial x} dx = 0 \tag{2.27a}$$

$$[W_i (\rho a u^2 + p a)]_S - \int_A (\rho a u^2 + p a) \frac{\partial W_i}{\partial x} dx - \int_A W_i p \frac{da}{dx} dx + \nu_2 \int_A \frac{\partial u}{\partial x} \frac{\partial W_i}{\partial x} dx = 0 \tag{2.27b}$$

Eq. (2.25c), the statement of constant total enthalpy, permits the elimination of the pressure from the x-momentum equation. The system of equations is reduced to two equations in two unknowns, ρ and u. Substituting Eq. (2.25c) into (2.27b) yields:

$$[W_i (\rho a u^2 + p a)]_S - \int_A \left(\frac{\gamma - 1}{\gamma} \rho a H_\infty + \frac{\gamma + 1}{2\gamma} \rho a u^2 \right) \frac{\partial W_i}{\partial x} dx - \frac{\gamma - 1}{\gamma} \int_A W_i \rho \left(H_\infty - \frac{u^2}{2} \right) \frac{da}{dx} dx -$$

$$+ \nu_2 \int_A \frac{\partial u}{\partial x} \frac{\partial W_i}{\partial x} dx = 0 \tag{2.28}$$

The system to be solved, Eq. (2.27a) and (2.28), is non-linear. The linearization procedure adopted is Newton's method, whose chief advantage lies in its quadratic convergence rate. The linearization is simply stated:

$$\rho^{n+1}=\rho^{n}+\Delta\rho \qquad u^{n+1}=u^{n}+\Delta u$$

The superscripts n+1 and n indicate the new and old values respectively. The continuity and x-momentum equations can be written in simple form as:

$$[J]\{\Delta(\rho,u)\}=\{r\}$$

where $[J]$ is the Jacobian of the linearization and $\{r\}$ indicates the residual of the FEM equations.

At convergence $\Delta\rho$ and Δu must vanish, hence the residuals also vanish. With this approach there is no uncertainty regarding the level of convergence of the iterative procedure: convergence is assessed directly from the residuals.

The procedure is completed by the introduction of the Finite Element discretization, Eq. (2.11). The continuity equation can be written as:

$$\sum_{j=1}^{df}[K^{\rho}_{i,j}]_{\rho}\Delta\hat{\rho}_j+\sum_{j=1}^{df}[K^{u}_{i,j}]_{\rho}\Delta\hat{u}_j=-\{R_i\}_{\rho}+[W_i(\rho au)]_S \qquad (2.29a)$$

where:

$$[K^{\rho}_{i,j}]_{\rho}=-\int_A (au)^n\frac{\partial W_i}{\partial x}N_j\,dx+\nu_1\int_A\frac{\partial W_i}{\partial x}\frac{\partial N_j}{\partial x}\,dx$$

$$[K^{u}_{i,j}]_{\rho}=-\int_A (a\rho)^n\frac{\partial W_i}{\partial x}N_j dx$$

$$\{R_i\}_{\rho}=-\int_A (\rho au)^n\frac{\partial W_i}{\partial x}N_j\,dx+\nu_1\int_A\frac{\partial W_i}{\partial x}\frac{\partial \rho^n}{\partial x}\,dx$$

Similarly the x-momentum equation can be written as:

$$\sum_{j=1}^{df}[K^{\rho}_{i,j}]_u \Delta\hat{\rho}_j + \sum_{j=1}^{df}[K^{u}_{i,j}]_u \Delta\hat{u}_j = {}_1R_i\}_u + [W_i(\rho a u^2 + pa)]_S \qquad (2.29b)$$

where:

$$[K^{\rho}_{i,j}]_u = -\frac{\gamma-1}{\gamma}H_\infty \int_A \left(\frac{\partial W_i}{\partial x}a + W_i\frac{da}{dx}\right)N_j\,dx - \frac{\gamma+1}{2\gamma}\int_A (au^2)^n \frac{\partial N_i}{\partial x}N_j\,dx + \frac{\gamma-1}{2\gamma}\int_A \left(\frac{da}{dx}u^2\right)^n W_i N_j\,dx$$

$$[K^{u}_{i,j}]_u = -\frac{\gamma+1}{\gamma}\int_A (\rho a u)^n \frac{\partial W_i}{\partial x}N_j\,dx + \frac{\gamma-1}{\gamma}\int_A \left(\rho\frac{da}{dx}u\right)^n W_i N_j\,dx + \nu_2\int_A \frac{\partial W_i}{\partial x}\frac{\partial N_j}{\partial x}\,dx$$

$$\{R_i\}_u = -\frac{\gamma-1}{\gamma}H_\infty \int_A \rho^n\left(\frac{\partial W_i}{\partial x}a + W_i\frac{da}{dx}\right)dx - \frac{\gamma+1}{2\gamma}\int_A (\rho a u^2)^n \frac{\partial W_i}{\partial x}\,dx + \frac{\gamma-1}{2\gamma}\int_A W_i\left(\rho\frac{da}{dx}u^2\right)^n dx$$

$$+ \nu_2\int_A \frac{\partial W_i}{\partial x}\frac{\partial u^n}{\partial x}\,dx$$

All the integrals are evaluated numerically, as opposed to the exact integrations of the time-dependent schemes. For 1-D cases the Gauss-Legendre integration procedure is exact if the proper number of sampling points is chosen.

Defining the non-dimensional shape functions, a sketch of which is shown in Fig. 3, as:

$$N_1 = \frac{1-\xi}{2} \qquad N_2 = \frac{1+\xi}{2}$$

Each integral can now be evaluated numerically using the equivalent form:

$$\int_A F(x)\,dx = \sum_{k=1}^{ngaus}[W_k F[x(\xi)]_k |J_k|] \qquad (2.30)$$

where W_k are the weights of the numerical integration and $J_k = \Delta x/\Delta\xi$ is the determinant of the Jacobian of the geometrical transformation of coordinates shown in Fig. 2 and 3. The subscript k indicates quantities evaluated at the Gaussian sampling points.

2.10 X-Momentum Contour Integral

The special manner in which the boundary conditions are specified for hyperbolic equations offers two possible ways of evaluating the contour integral of the x-momentum equation. The boundary pressure integral is evaluated differently depending on whether the pressure is known or not, while the remainder of the integral remains the same in both cases. For an unknown pressure the energy equation is again introduced to eliminate the pressure. The integral becomes:

$$[W_i(\rho au^2+pa)]_S=\left[W_i \left(\frac{\gamma+1}{2\gamma}\rho au^2+\frac{\gamma-1}{\gamma}\rho aH_\infty\right)\right]_S \tag{2.31}$$

For a known pressure, such as a specified back pressure, the integral becomes:

$$[W_i(\rho au^2+pa)]_S=[W_i\,\rho au^2]_S+[W_i p a]_S^n \tag{2.32}$$

where the last term is constant and can be evaluated on the right-hand side of Eq. (2.28).

CHAPTER 3

3.1 A Finite Element Scheme for the Solution of the Steady 2-D Euler Equations

Four schemes for the solution of the 1-D Euler equations were demonstrated in the preceding chapter in a finite element context. The Newton scheme has demonstrated to be the simplest and most rapid and will be extended to two dimensions in this chapter.

Before illustrating this scheme, some remarks about the time-dependent formulations are necessary. Aside from the poor rate of convergence of the Lax-Wendroff scheme, it is evident that none of the presented time-dependent formulations can take full advantage of the power of the Finite Element method in 3-D or even 2-D. One of the important attractions of a finite element formulation should be the occurrence of natural boundary conditions, but it has been demonstrated that these can be recovered neither from the Lax-Wendroff nor from the Lerat schemes. The enforcement of wall or symmetry line boundary conditions not originally present in – or not recoverable from – a finite element scheme conflicts with the essence of the method, whose chief appeal lies in the isolation of the numerical scheme from the geometrical complexities of the solution domain.

In the following derivation it will be shown that the shape functions of the Finite Element discretization can easily be used in 2-D as an effective boundary extrapolation method which does not complicate the formulation of the implicit scheme. This is not the case with other discretization procedures, such as Finite Differences or Finite Volume, which require the explicit introduction of the Riemann invariants or other extrapolation schemes to handle non-reflecting boundary conditions[21]. The distinction is a consequence of the nature of the discretization operators since, unlike the finite element method, the finite differences and finite volume stencils are based on pointwise operators that do not represent functions

continuously between nodes. In addition, the contour integrals generated by the weak formulation can also be exploited to impose no-penetration boundary conditions. Hence the Galerkin approach can take complete advantage of the Euler Equations without requiring extra add-on features like all the current schemes.

Among the useful characteristics of the Galerkin scheme is the recovery of the pressure contour integrals from the two momentum equations: they become very important in case the pressure is known somewhere on the boundary of the solution domain. It becomes clear that the Finite Element method is the only method which can really solve the Euler equations everywhere in the solution domain, including the boundaries. Furthermore it is the only method which can recover a set of natural boundary conditions directly from the equations.

3.2 2-D Euler Equations

Consider the 2-D Euler equations for a perfect gas, with the assumption of constant total enthalpy and $\gamma = 1.4$. The system of equations can be written as:

$$\frac{\partial}{\partial x}(\rho u)+\frac{\partial}{\partial y}(\rho v)=0 \tag{3.1a}$$

$$\frac{\partial}{\partial x}(\rho u^2+p)+\frac{\partial}{\partial y}(\rho uv)=0 \tag{3.1b}$$

$$\frac{\partial}{\partial x}(\rho uv)+\frac{\partial}{\partial y}(\rho v^2+p)=0 \tag{3.1c}$$

$$p=\frac{\gamma-1}{\gamma}\rho\left(H_\infty-\frac{u^2+v^2}{2}\right) \tag{3.1d}$$

As noted for the 1-D scheme, it is necessary to add some viscous terms to the central operator discretization in order to inhibit the formation of expansion shocks. There is an ample selection of types of artificial viscosity, however, for simplicity a Laplacian function

of the solution variables ρ, u and v was selected. The addition of these terms produces the following system of equations:

$$\frac{\partial}{\partial x}(\rho u)+\frac{\partial}{\partial y}(\rho v)=\mu\left(\frac{\partial^2 \rho}{\partial x^2}+\frac{\partial^2 \rho}{\partial y^2}\right) \tag{3.2a}$$

$$\frac{\partial}{\partial x}(\rho u^2+p)+\frac{\partial}{\partial y}(\rho uv)=\mu\left(\frac{\partial^2 u}{\partial x^2}+\frac{\partial^2 u}{\partial y^2}\right) \tag{3.2b}$$

$$\frac{\partial}{\partial x}(\rho uv)+\frac{\partial}{\partial y}(\rho v^2+p)=\mu\left(\frac{\partial^2 v}{\partial x^2}+\frac{\partial^2 v}{\partial y^2}\right) \tag{3.2c}$$

where μ is the artificial viscosity parameter. The equations are converted to a non-dimensional form with respect to the free-stream conditions ρ_∞, U_∞ and L, where L is a characteristic length such as the chord of an airfoil or the length of a nozzle. This transformation yields the non-dimensional form:

$$\frac{\partial}{\partial x}(\rho u)+\frac{\partial}{\partial y}(\rho v)=\upsilon_1\left(\frac{\partial^2 \rho}{\partial x^2}+\frac{\partial^2 \rho}{\partial y^2}\right) \tag{3.3a}$$

$$\frac{\partial}{\partial x}(\rho u^2+p)+\frac{\partial}{\partial y}(\rho uv)=\upsilon_2\left(\frac{\partial^2 u}{\partial x^2}+\frac{\partial^2 u}{\partial y^2}\right) \tag{3.3b}$$

$$\frac{\partial}{\partial x}(\rho uv)+\frac{\partial}{\partial y}(\rho v^2+p)=\upsilon_2\left(\frac{\partial^2 v}{\partial x^2}+\frac{\partial^2 v}{\partial y^2}\right) \tag{3.3c}$$

$$p=\frac{\gamma-1}{\gamma}\rho\left(H_\infty-\frac{u^2+v^2}{2}\right) \tag{3.3d}$$

$$\upsilon_1=\frac{\mu}{U_\infty L} \qquad\qquad \upsilon_2=\frac{\mu}{\rho_\infty U_\infty L}$$

Two artificial viscosity parameters now appear in Eqs. (3.3), both uniquely determined by the selection of μ and the free-stream conditions.

3.3 The Newton-Galerkin Finite Element Scheme

The Galerkin integral is constructed separately for each equation. Note that in the following outline the weights W_i are identical to the Finite Element shape functions, denoted by N_j. The surface of the solution region is denoted by A and its contour by S. Eqs. (3.3) can be recast in the integral form as follows:

$$\iint_A W_i\left[\frac{\partial}{\partial x}(\rho u)+\frac{\partial}{\partial y}(\rho v)-\upsilon_1\left(\frac{\partial^2\rho}{\partial x^2}+\frac{\partial^2\rho}{\partial y^2}\right)\right]dA=0 \tag{3.4a}$$

$$\iint_A W_i\left[\frac{\partial}{\partial x}(\rho u^2+p)+\frac{\partial}{\partial y}(\rho uv)-\upsilon_2\left(\frac{\partial^2 u}{\partial x^2}+\frac{\partial^2 u}{\partial y^2}\right)\right]dA=0 \tag{3.4b}$$

$$\iint_A W_i\left[\frac{\partial}{\partial x}(\rho uv)+\frac{\partial}{\partial y}(\rho v^2+p)-\upsilon_2\left(\frac{\partial^2 v}{\partial x^2}+\frac{\partial^2 v}{\partial y^2}\right)\right]dA=0 \tag{3.4c}$$

The pressure term can be recast in terms of the unknowns by introducing Eq. (3.3d). Thus:

$$\iint_A\left[(\rho u)\frac{\partial W_i}{\partial x}+(\rho v)\frac{\partial W_i}{\partial y}\right]dA-\upsilon_1\iint_A\left(\frac{\partial\rho}{\partial x}\frac{\partial W_i}{\partial x}+\frac{\partial\rho}{\partial y}\frac{\partial W_i}{\partial y}\right)dA$$

$$=\int_S W_i\,\rho(\vec{q}\cdot\vec{n})dS-\int_S W_i\frac{\partial\rho}{\partial n}dS \tag{3.5a}$$

$$\iint_A\left[\left(\frac{\gamma+1}{2\gamma}\rho u^2-\frac{\gamma-1}{2\gamma}\rho v^2+\frac{\gamma-1}{\gamma}\rho H_\infty\right)\frac{\partial W_i}{\partial x}+(\rho uv)\frac{\partial W_i}{\partial y}\right]dA-\upsilon_2\iint_A\left(\frac{\partial u}{\partial x}\frac{\partial W_i}{\partial x}+\frac{\partial u}{\partial y}\frac{\partial W_i}{\partial y}\right)dA$$

$$=\int_S W_i\,\rho u(\vec{q}\cdot\vec{n})\,dS+\int_S W_i p\frac{dy}{dS}\,dS-\int_S W_i\frac{\partial u}{\partial n}dS \tag{3.5b}$$

$$\iint_A\left[(\rho uv)\frac{\partial W_i}{\partial x}+\left(\frac{\gamma+1}{2\gamma}\rho v^2-\frac{\gamma-1}{2\gamma}\rho u^2+\frac{\gamma-1}{\gamma}\rho H_\infty\right)\frac{\partial W_i}{\partial y}\right]dA-\upsilon_2\iint_A\left(\frac{\partial v}{\partial x}\frac{\partial W_i}{\partial x}+\frac{\partial v}{\partial y}\frac{\partial W_i}{\partial y}\right)dA$$

$$=\int_S W_i\,\rho v(\vec{q}\cdot\vec{n})dS-\int_S W_i p\frac{dx}{dS}\,dS-\int_S W_i\frac{\partial v}{\partial n}dS \tag{3.5c}$$

where:

$$\vec{q}=u\vec{i}+v\vec{j}$$

and $\bar{n}$ is the local unit vector normal to the boundary.

The equations are non-linear and an iterative scheme is required for their solution. The Newton linearization can be introduced by setting:

$$\Delta U = U^{n+1} - U^{n}$$

where $U = (\rho, u, v)^{T}$ and neglecting all the products of order higher than ΔU.

The process is complete after introducing the finite element discretization of the dependent variables:

$$U = \sum_{j=1}^{df} N_j \hat{U}_j \tag{3.6}$$

where:

$$N_j = \frac{1}{4}(1+\xi\xi_j)(1+\eta\eta_j) \qquad j = 1,\ldots,4$$

are the shape functions for a linear quadrilateral isoparametric element such as the one shown in Fig. 4. The shape function derivatives can be obtained from the local element transformation[25]. Let:

$$\begin{bmatrix} \frac{\partial N_i}{\partial \xi} \\ \frac{\partial N_i}{\partial \eta} \end{bmatrix}^{(e)} = \begin{bmatrix} \frac{\partial x}{\partial \xi} & \frac{\partial y}{\partial \xi} \\ \frac{\partial x}{\partial \eta} & \frac{\partial y}{\partial \eta} \end{bmatrix}^{(e)} \begin{bmatrix} \frac{\partial N_i}{\partial x} \\ \frac{\partial N_i}{\partial y} \end{bmatrix}^{(e)} = [J]^{(e)} \begin{bmatrix} \frac{\partial N_i}{\partial x} \\ \frac{\partial N_i}{\partial y} \end{bmatrix}^{(e)}$$

where the entries of the Jacobian of the local transformations can be computed directly from the local shape function derivatives. For example the first term can be discretized in the form:

$$\frac{\partial x}{\partial \xi} = \sum_{j=1}^{df} \frac{\partial N_j}{\partial \xi} \hat{x}_j \tag{3.7}$$

where the $\hat{x}_j$s in Eq. (3.7) are the nodal x-coordinates. The other entries of the Jacobian are computed in the same fashion. The x- and y-derivatives can be found from the inverse of the Jacobian – a simple 2×2 matrix which can be inverted directly – as follows:

$$\begin{bmatrix} \frac{\partial N_i}{\partial x} \\ \frac{\partial N_i}{\partial y} \end{bmatrix}^{(e)} = [J]^{-1} \begin{bmatrix} \frac{\partial N_i}{\partial \xi} \\ \frac{\partial N_i}{\partial \eta} \end{bmatrix}^{(e)}$$

After introducing the above procedure on an element basis, the continuity equation can be recast in the form :

$$\sum_{j=1}^{df} [K_{ij}^{\rho}]\, \Delta\hat{\rho}_j + \sum_{j=1}^{df} [K_{ij}^{u}]_{\rho} \Delta\hat{u}_j + \sum_{j=1}^{df} [K_{ij}^{v}]_{\rho} \Delta\hat{v}_j = -\{R_i\}_{\rho}$$
$$+ \int_S W_i\, \rho(\vec{q}\cdot\vec{n})dS - \int_S W_i \frac{\partial \rho}{\partial n} dS \qquad (3.8a)$$

where:

$$[K_{ij}^{\rho}]_{\rho} = \int_A \int N_j \left(u^n \frac{\partial W_i}{\partial x} + v^n \frac{\partial W_i}{\partial y} \right) dA - \upsilon_1 \int_A \int \left(\frac{\partial W_i}{\partial x}\frac{\partial N_j}{\partial x} + \frac{\partial W_i}{\partial y}\frac{\partial N_j}{\partial y} \right) dA$$

$$[K_{ij}^{u}]_{\rho} = \int_A \int \rho^n N_j \frac{\partial W_i}{\partial x}\, dA$$

$$[K_{ij}^{v}]_{\rho} = \int_A \int \rho^n N_j \frac{\partial W_i}{\partial y}\, dA$$

$$\{R_i\}_{\rho} = \int_A \int \left[(\rho u)^n \frac{\partial W_i}{\partial x} + (\rho v)^n \frac{\partial W_i}{\partial y} \right] dA - \upsilon_1 \int_A \int \left(\frac{\partial W_i}{\partial x}\frac{\partial \rho^n}{\partial x} + \frac{\partial W_i}{\partial y}\frac{\partial \rho^n}{\partial y} \right) dA$$

Similarly the x-momentum equation becomes:

$$\sum_{j=1}^{df}[K_{ij}^{\rho}]_u\Delta\hat{\rho}_j+\sum_{j=1}^{df}[K_{ij}^{u}]_u\Delta\hat{u}_j+\sum_{j=1}^{df}[K_{ij}^{v}]_u\Delta\hat{v}_j=-\{R_i\}_u$$

$$+\int_S W_i\,\rho u(\vec{q}\cdot\vec{n})dS+\int_S W_i p\frac{\partial y}{\partial S}dS-\int_S W_i\frac{\partial u}{\partial n}dS \qquad (3.8b)$$

where:

$$[K_{ij}^{\rho}]_u=\int_A\int N_j\left[\left(\frac{\gamma+1}{2\gamma}(u^2)^n-\frac{\gamma-1}{2\gamma}(v^2)^n+\frac{\gamma-1}{\gamma}H_\infty\right)\frac{\partial W_i}{\partial x}+(uv)^n\frac{\partial W_i}{\partial y}\right]dA$$

$$[K_{ij}^{u}]_u=\int_A\int N_j\left[\frac{\gamma+1}{\gamma}(\rho u)^n\frac{\partial W_i}{\partial x}+(\rho v)^n\frac{\partial W_i}{\partial y}\right]dA-\upsilon_2\int_A\int\left(\frac{\partial W_i}{\partial x}\frac{\partial N_j}{\partial x}+\frac{\partial W_i}{\partial y}\frac{\partial N_j}{\partial y}\right)dA$$

$$[K_{ij}^{v}]_u=-\int_A\int N_j\left[\frac{\gamma-1}{\gamma}(\rho v)^n\frac{\partial W_i}{\partial x}-(\rho u)^n\frac{\partial W_i}{\partial y}\right]dA$$

$$\{R_i\}_u=\int_A\int\left[\left(\frac{\gamma+1}{2\gamma}(\rho u^2)^n-\frac{\gamma-1}{2\gamma}(\rho v^2)^n+\frac{\gamma-1}{\gamma}\rho H_\infty\right)\frac{\partial W_i}{\partial x}+(\rho uv)^n\frac{\partial W_i}{\partial y}\right]dA$$

$$-\upsilon_2\int_A\int\left(\frac{\partial W_i}{\partial x}\frac{\partial u^n}{\partial x}+\frac{\partial W_i}{\partial y}\frac{\partial u^n}{\partial y}\right)dA$$

And finally the y-momentum equation is in the form:

$$\sum_{j=1}^{df}[K_{ij}^{\rho}]_v\Delta\hat{\rho}_j+\sum_{j=1}^{df}[K_{ij}^{u}]_v\Delta\hat{u}_j+\sum_{j=1}^{df}[K_{ij}^{v}]_v\Delta\hat{v}_j=-\{R_i\}_v$$

$$+\int_S W_i\,\rho v(\vec{q}\cdot\vec{n})dS-\int_S W_i p\frac{\partial x}{\partial S}dS-\int_S W_i\frac{\partial v}{\partial n}dS \qquad (3.8c)$$

where:

$$[K_{ij}^{\rho}]_v=\int_A\int N_j\left[(uv)^n\frac{\partial W_i}{\partial x}+\left(\frac{\gamma+1}{2\gamma}(v^2)^n-\frac{\gamma-1}{2\gamma}(u^2)^n+\frac{\gamma-1}{\gamma}H_\infty\right)\frac{\partial W_i}{\partial y}\right]dA$$

$$[K_{ij}^{u}]_v=\int_A\int N_j\left[(\rho v)^n\frac{\partial W_i}{\partial x}-\frac{\gamma-1}{\gamma}(\rho u)^n\frac{\partial W_i}{\partial y}\right]dA$$

$$[K_{ij}^{v}]_v = \int_A\int N_j\left[(\rho u)^n \frac{\partial W_i}{\partial x} + \frac{\gamma+1}{\gamma}(\rho v)^n \frac{\partial W_i}{\partial y} \right] dA - \upsilon_2 \int_A\int \left(\frac{\partial W_i}{\partial x}\frac{\partial N_j}{\partial x} + \frac{\partial W_i}{\partial y}\frac{\partial N_j}{\partial y} \right) dA$$

$$\{R_i\}_v = \int_A\int \left[(\rho uv)^n \frac{\partial W_i}{\partial x} + \left(\frac{\gamma+1}{2\gamma}(\rho v^2)^n - \frac{\gamma-1}{2\gamma}(\rho u^2)^n + \frac{\gamma-1}{\gamma}\rho H_\infty \right) \frac{\partial W_i}{\partial y} \right] dA$$

$$- \upsilon_2 \int_A\int \left(\frac{\partial W_i}{\partial x}\frac{\partial v^n}{\partial x} + \frac{\partial W_i}{\partial y}\frac{\partial v^n}{\partial y} \right) dA$$

Eqs. (3.8) form a block-tridiagonal system of coupled linear equations. The integrals must be evaluated numerically, in this case by the Gauss-Legendre quadrature formula:

$$[K_{ij}] = \int_{-1}^{1}\int_{-1}^{1} k_{ij}[x(\xi,\eta), y(\xi,\eta)] \mid J \mid d\xi\, d\eta = \sum_{r=1}^{ngaus}\sum_{s=1}^{ngaus} W_r W_s \{k_{ij}[x(\xi,\eta), y(\xi,\eta)] \mid J \mid\}_{r,s}$$

where 'ngaus' is the number of Gaussian points in each local coordinate direction. For all the 2-D test cases reported here ngaus=3, permitting the exact integration of a polynomial up to degree 5. W indicates the weights of the Gaussian quadrature and the subscripts r and s denote quantities evaluated at the Gaussian points [26].

Note that the system of Eqs. (3.8) is not diagonally dominant and requires a Gauss solver, however it has been found that the ill-conditioning of the global matrix is not severe enough to require the introduction of pivoting.

3.4 Unsteady Flows

The steady-state formulation outlined in the previous section can be extended to the time-dependent Euler equations to analyze the stability of shock waves in converging-diverging channels. The method that will be outlined is only first-order accurate in time, however, the issue concerning the time accuracy of the solution is of secondary importance compared to the investigation of shock wave instability.

A time-marching scheme for the Euler equations can be constructed by adding discrete time terms to the steady-state formulation. For a truly unsteady formulation the assumption of constant H_∞ is not acceptable and the complete energy equation must be solved along with continuity and momentum. The time-dependent Euler equations with added dissipation terms can be cast in the form:

$$\frac{\partial}{\partial t}(\rho)+\frac{\partial}{\partial x}(\rho u)+\frac{\partial}{\partial y}(\rho v)=\upsilon_1\left(\frac{\partial^2\rho}{\partial x^2}+\frac{\partial^2\rho}{\partial y^2}\right) \tag{3.9a}$$

$$\frac{\partial}{\partial t}(\rho u)+\frac{\partial}{\partial x}(\rho u^2+p)+\frac{\partial}{\partial y}(\rho uv)=\upsilon_2\left(\frac{\partial^2 u}{\partial x^2}+\frac{\partial^2 u}{\partial y^2}\right) \tag{3.9b}$$

$$\frac{\partial}{\partial t}(\rho v)+\frac{\partial}{\partial x}(\rho uv)+\frac{\partial}{\partial y}(\rho v^2+p)=\upsilon_2\left(\frac{\partial^2 v}{\partial x^2}+\frac{\partial^2 v}{\partial y^2}\right) \tag{3.9c}$$

$$\frac{\partial}{\partial t}(\rho e)+\frac{\partial}{\partial x}[u(\rho e+p)]+\frac{\partial}{\partial y}[v(\rho e+p)]=\upsilon_2\left(\frac{\partial^2 e}{\partial x^2}+\frac{\partial^2 e}{\partial y^2}\right) \tag{3.9d}$$

$$p=(\gamma-1)\rho\left(e-\frac{u^2+v^2}{2}\right) \tag{3.9e}$$

where $\gamma=1.4$ as before.

The time derivatives can be discretized by a two point backward difference to produce a hybrid implicit scheme. The procedure is simple:

$$\frac{\rho^{n+1}-\rho^n}{\Delta t}+\frac{\partial}{\partial x}(\rho u)+\frac{\partial}{\partial y}(\rho v)=\upsilon_1\left(\frac{\partial^2\rho}{\partial x^2}+\frac{\partial^2\rho}{\partial y^2}\right) \tag{3.10a}$$

$$\frac{(\rho u)^{n+1}-(\rho u)^n}{\Delta t}+\frac{\partial}{\partial x}(\rho u^2+p)+\frac{\partial}{\partial y}(\rho uv)=\upsilon_2\left(\frac{\partial^2 u}{\partial x^2}+\frac{\partial^2 u}{\partial y^2}\right) \tag{3.10b}$$

$$\frac{(\rho v)^{n+1}-(\rho v)^n}{\Delta t}+\frac{\partial}{\partial x}(\rho uv)+\frac{\partial}{\partial y}(\rho v^2+p)=\upsilon_2\left(\frac{\partial^2 v}{\partial x^2}+\frac{\partial^2 v}{\partial y^2}\right) \tag{3.10c}$$

$$\frac{(\rho e)^{n+1}-(\rho e)^n}{\Delta t}+\frac{\partial}{\partial x}[u(\rho e+p)]+\frac{\partial}{\partial y}[v(\rho e+p)]=\upsilon_2\left(\frac{\partial^2 e}{\partial x^2}+\frac{\partial^2 e}{\partial y^2}\right) \tag{3.10d}$$

The backward time differences can be simplified even further once Newton's method is applied to the first term in Eqs. (3.10). The (n+1) time term for Eq. (3.10b), for example, reduces to the form:

$$\frac{(\rho u)^{n+1}-(\rho u)^n}{\Delta t}=\frac{(\rho^n+\Delta\rho)(u^n+\Delta u)-(\rho u)^n}{\Delta t}=\frac{u^n\Delta\rho+\rho^n\Delta u}{\Delta t}$$

The same principle applies to the other equations. The space discretization is based on the same procedure outlined for Eqs. (3.4) to (3.8). The finite element form of the continuity equation becomes:

$$\sum_{j=1}^{df}[K_{ij}^{\rho}]_{\rho}\Delta\hat{\rho}_j+\sum_{j=1}^{df}[K_{ij}^{u}]_{\rho}\Delta\hat{u}_j+\sum_{j=1}^{df}[K_{ij}^{v}]_{\rho}\Delta\hat{v}_j=-\{R_i\}_{\rho}-$$

$$\int_S W_i\,\rho(\bar{q}\cdot\bar{n})dS+\upsilon_1\int_S W_i\frac{\partial\rho}{\partial n}dS \qquad (3.11a)$$

where:

$$[K_{ij}^{\rho}]_{\rho}=\int_A\int N_j\left(\frac{W_i}{\Delta t}-u^n\frac{\partial W_i}{\partial x}-v^n\frac{\partial W_i}{\partial y}\right)dA+\upsilon_1\int_A\int\left(\frac{\partial W_i}{\partial x}\frac{\partial N_j}{\partial x}+\frac{\partial W_i}{\partial y}\frac{\partial N_j}{\partial y}\right)dA$$

$$[K_{ij}^{u}]_{\rho}=-\int_A\int\rho^n N_j\frac{\partial W_i}{\partial x}\,dA$$

$$[K_{ij}^{v}]_{\rho}=-\int_A\int\rho^n N_j\frac{\partial W_i}{\partial y}\,dA$$

$$\{R_i\}_{\rho}=-\int_A\int\left[(\rho u)^n\frac{\partial W_i}{\partial x}+(\rho v)^n\frac{\partial W_i}{\partial y}\right]dA+\upsilon_1\int_A\int\left(\frac{\partial W_i}{\partial x}\frac{\partial\rho^n}{\partial x}+\frac{\partial W_i}{\partial y}\frac{\partial\rho^n}{\partial y}\right)dA$$

Similarly the x-momentum equation becomes:

$$\sum_{j=1}^{df}[K_{ij}^{\rho}]_{u}\Delta\hat{\rho}_j+\sum_{j=1}^{df}[K_{ij}^{u}]_{u}\Delta\hat{u}_j+\sum_{j=1}^{df}[K_{ij}^{v}]_{u}\Delta\hat{v}_j+\sum_{j=1}^{df}[K_{ij}^{e}]_{u}\Delta\hat{e}_j=-\{R_i\}_{u}-$$

$$\int_S W_i\,\rho u(\bar{q}\cdot\bar{n})dS-(\gamma-1)\int_S W_i\rho\left(e-\frac{u^2+v^2}{2}\right)\frac{dy}{dS}dS+\upsilon_2\int_S W_i\frac{\partial u}{\partial n}dS \qquad (3.11b)$$

where:

$$[K^{\rho}_{ij}]_u=\int_A\int N_j\left[u^n\frac{W_i}{\Delta t}+\left(\frac{\gamma-3}{2}(u^2)^n+\frac{\gamma-1}{2}(v^2)^n-(\gamma-1)e^n\right)\frac{\partial W_i}{\partial x}-(uv)^n\frac{\partial W_i}{\partial y}\right]dA$$

$$[K^{u}_{ij}]_u=\int_A\int N_j\left[\rho^n\frac{W_i}{\Delta t}+(\gamma-3)(\rho u)^n\frac{\partial W_i}{\partial x}-(\rho v)^n\frac{\partial W_i}{\partial y}\right]dA+\upsilon_2\int_A\int\left(\frac{\partial W_i}{\partial x}\frac{\partial N_j}{\partial x}+\frac{\partial W_i}{\partial y}\frac{\partial N_j}{\partial y}\right)dA$$

$$[K^{v}_{ij}]_u=-\int_A\int N_j\left[(\gamma-1)(\rho v)^n\frac{\partial W_i}{\partial x}-(\rho u)^n\frac{\partial W_i}{\partial y}\right]dA$$

$$[K^{e}_{ij}]_u=-(\gamma-1)\int_A\int N_j\rho^n\frac{\partial W_i}{\partial x}dA$$

$$\{R_i\}_u=\int_A\int\left[\left(\frac{\gamma-3}{2}(\rho u^2)^n+\frac{\gamma-1}{2}(\rho v^2)^n-(\gamma-1)(\rho e)^n\right)\frac{\partial W_i}{\partial x}-(\rho uv)^n\frac{\partial W_i}{\partial y}\right]dA+$$

$$\upsilon_2\int_A\int\left(\frac{\partial W_i}{\partial x}\frac{\partial u^n}{\partial x}+\frac{\partial W_i}{\partial y}\frac{\partial u^n}{\partial y}\right)dA$$

The y-momentum becomes:

$$\sum_{j=1}^{df}[K^{\rho}_{ij}]_v\,\Delta\hat{\rho}_j+\sum_{j=1}^{df}[K^{u}_{ij}]_v\,\Delta\hat{u}_j+\sum_{j=1}^{df}[K^{v}_{ij}]_v\,\Delta\hat{v}_j+\sum_{j=1}^{df}[K^{e}_{ij}]_v\,\Delta\hat{e}_j=-\{R_i\}_v-$$

$$\int_S W_i\rho v(\tilde{q}\cdot\tilde{n})dS+(\gamma-1)\int_S W_i\rho\left(e-\frac{u^2+v^2}{2}\right)\frac{\partial x}{\partial S}dS+\upsilon_2\int_S W_i\frac{\partial v}{\partial n}dS \qquad (3.11c)$$

where:

$$[K^{\rho}_{ij}]_v=\int_A\int N_j\left[v^n\frac{W_i}{\Delta t}-(uv)^n\frac{\partial W_i}{\partial x}+\left(\frac{\gamma-1}{2}(u^2)^n+\frac{\gamma-3}{2}(v^2)^n-(\gamma-1)e^n\right)\frac{\partial W_i}{\partial y}\right]dA$$

$$[K^{u}_{ij}]_v=-\int_A\int N_j\left[(\rho v)^n\frac{\partial W_i}{\partial x}-(\gamma-1)(\rho u)^n\frac{\partial W_i}{\partial y}\right]dA$$

$$[K^{v}_{ij}]_v=-\int_A\int N_j\left[\rho^n\frac{W_i}{\Delta t}-(\rho u)^n\frac{\partial W_i}{\partial x}-(\gamma-3)(\rho v)^n\frac{\partial W_i}{\partial y}\right]dA+\upsilon_2\int_A\int\left(\frac{\partial W_i}{\partial x}\frac{\partial N_j}{\partial x}+\frac{\partial W_i}{\partial y}\frac{\partial N_j}{\partial y}\right)dA$$

$$[K^{e}_{ij}]_v=-(\gamma-1)\int_A\int N_j\rho^n\frac{\partial W_i}{\partial y}dA$$

$$\{R_i\}_v=-\iint_A\left[(\rho uv)^n\frac{\partial W_i}{\partial x}-\left(\frac{\gamma-1}{2}(\rho u^2)^n+\frac{\gamma-3}{2}(\rho v^2)^n-(\gamma-1)(\rho e)^n\right)\frac{\partial W_i}{\partial y}\right]dA+$$

$$\upsilon_2\iint_A\left(\frac{\partial W_i}{\partial x}\frac{\partial v^n}{\partial x}+\frac{\partial W_i}{\partial y}\frac{\partial v^n}{\partial y}\right)dA$$

Finally the energy equation assumes the form:

$$\sum_{j=1}^{df}[K^{\rho}_{ij}]_e\Delta\hat{\rho}_j+\sum_{j=1}^{df}[K^{u}_{ij}]_e\Delta\hat{u}_j+\sum_{j=1}^{df}[K^{v}_{ij}]_e\Delta\hat{v}_j+\sum_{j=1}^{df}[K^{e}_{ij}]_e\Delta\hat{e}_j=-\{R_i\}_e-$$

$$\int_S W_i\,\rho\left[\gamma e-\frac{\gamma-1}{2}(u^2+v^2)\right](\vec{q}\cdot\vec{n})dS+\upsilon_2\int_S W_i\frac{\partial e}{\partial n}dS \qquad (3.11d)$$

where:

$$[K^{\rho}_{ij}]_e=\iint_A N_j\left[e^n\frac{W_i}{\Delta t}-\left(\gamma e-\frac{\gamma-1}{2}(u^2+v^2)\right)^n\left(u^n\frac{\partial W_i}{\partial x}+v^n\frac{\partial W_i}{\partial y}\right)\right]dA$$

$$[K^{u}_{ij}]_e=-\iint_A N_j\rho^n\left[\left(\gamma e-\frac{\gamma-1}{2}(3u^2+v^2)\right)^n\frac{\partial W_i}{\partial x}-(\gamma-1)(uv)^n\frac{\partial W_i}{\partial y}\right]dA$$

$$[K^{v}_{ij}]_e=\iint_A N_j\rho^n\left[(\gamma-1)(uv)^n\frac{\partial W_i}{\partial x}-\left(\gamma e-\frac{\gamma-1}{2}(u^2+3v^2)\right)^n\frac{\partial W_i}{\partial y}\right]dA$$

$$[K^{e}_{ij}]_e=\iint_A N_j\rho^n\left[\frac{W_i}{\Delta t}-\gamma\left(u^n\frac{\partial W_i}{\partial x}+v^n\frac{\partial W_i}{\partial y}\right)\right]dA+\upsilon_2\iint_A\left(\frac{\partial W_i}{\partial x}\frac{\partial N_j}{\partial x}+\frac{\partial W_i}{\partial y}\frac{\partial N_j}{\partial y}\right)dA$$

$$\{R_i\}_e=-\iint_A\left[\left(\gamma e-\frac{\gamma-1}{2}(u^2+v^2)\right)^n\left((\rho u)^n\frac{\partial W_i}{\partial x}+(\rho v)^n\frac{\partial W_i}{\partial y}\right)\right]dA+$$

$$\upsilon_2\iint_A\left(\frac{\partial W_i}{\partial x}\frac{\partial e^n}{\partial x}+\frac{\partial W_i}{\partial y}\frac{\partial e^n}{\partial y}\right)dA$$

Eqs. (3.11) form a coupled implicit time-marching scheme which requires the solution of a block tridiagonal system of linear equations at each iteration. The integration of the influence matrices is obtained by the same method used for Eqs. (3.8). The value of the time increment Δt is kept constant during the unsteady analysis. Note that for $\Delta t = \infty$ Newton's method is recovered and Eqs. (3.11) will converge quadratically to the steady-state solution of Eqs. (3.9).

3.5 Boundary Conditions

The description of the two schemes outlined in the previous sections would not be complete without a discussion of their boundary conditions. To put the 2-D Euler equations in a form more suited for analysis, consider Eqs. (3.1) rewritten in their vector notation:

$$\frac{\partial U}{\partial t}+\frac{\partial F}{\partial x}+\frac{\partial G}{\partial y}=0 \tag{3.12}$$

where, for four equations, the vector terms are defined as:

$$U=\begin{bmatrix}\rho\\ \rho u\\ \rho v\\ \rho e\end{bmatrix} \qquad F=\begin{bmatrix}\rho u\\ \rho u^2+p\\ \rho uv\\ u(\rho e+p)\end{bmatrix} \qquad G=\begin{bmatrix}\rho v\\ \rho uv\\ \rho v^2+p\\ v(\rho e+p)\end{bmatrix}$$

At this point Eqs. (3.12) can identify both a system of three conservation laws, such as Eqs. (3.1), or a system of four conservation laws like Eqs. (3.9). In general the expression "three equations model" is used to identify three partial differential equations – continuity and two momentum equations – while "four equations model" refers to four partial differential equations – continuity, the two momentum and the energy equation. The presence of the equation of state in terms of pressure, while taken for granted in both systems, is not mentioned explicitly because it is an algebraic relation that does not influence the hyperbolic nature of the system of equations. Note that the assumption that the total enthalpy H_∞ is constant everywhere when the system of equation reaches the steady-state has an innocuous appearance, nonetheless it also has a subtle effect on the treatment of the boundary conditions.

Proceeding with the analysis of the boundary conditions, Eq. (3.12) can be recast in the quasi-linear form:

$$\frac{\partial U}{\partial t}+A\frac{\partial U}{\partial x}+B\frac{\partial U}{\partial y}=0 \tag{3.13}$$

where $A=\partial F/\partial U$, $B=\partial G/\partial U$ and the matrices for the four equations model are defined as follows:

$$A=\begin{bmatrix} 0 & 1 & 0 & 0 \\ \frac{\gamma-3}{2}u^2+\frac{\gamma-1}{2}v^2 & -(\gamma-3)u & -(\gamma-1)v & (\gamma-1) \\ -uv & v & u & 0 \\ -\gamma ue+(\gamma-1)u(u^2+v^2) & \gamma e-\frac{\gamma-1}{2}(3u^2+v^2) & -(\gamma-1)uv & \gamma u \end{bmatrix}$$

$$B=\begin{bmatrix} 0 & 0 & 1 & 0 \\ uv & v & u & 0 \\ \frac{\gamma-3}{2}v^2+\frac{\gamma-1}{2}u^2 & -(\gamma-1)u & -(\gamma-3)v & (\gamma-1) \\ -\gamma ve+(\gamma-1)v(u^2+v^2) & -(\gamma-1)uv & \gamma e-\frac{\gamma-1}{2}(3v^2+u^2) & \gamma v \end{bmatrix}$$

The Jacobian A has four real eigenvalues:

$$\lambda_1=u \qquad \lambda_2=u \qquad \lambda_3=u+c \qquad \lambda_4=u-c$$

where c is the speed of sound. Similarly the Jacobian B has four real eigenvalues:

$$\lambda_1=v \qquad \lambda_2=v \qquad \lambda_3=v+c \qquad \lambda_4=v-c$$

Since all the eigenvalues are real it follows that Eqs. (3.12) or Eqs. (3.13) are hyperbolic with respect to time. In the case of the steady-state formulation the classification of the nature of the equations appears to be more complex.

In all the known finite difference and finite volume formulations the time-dependent terms are always used as a vehicle to capture the steady-state solution, but often additional techniques, such as the residual averaging and enthalpy damping of Jameson or the more widely used multigrid acceleration [8], are incorporated to improve the notoriously poor convergence rate of the basic explicit schemes. Most of the schemes modified in this fashion are no longer time-accurate, however they still conserve their hyperbolic nature, which is clearly independent of the intrinsic definition of time. In substance the modified schemes which are no longer time-accurate can be thought of as being hyperbolic with respect to a pseudo-time. If the time-dependent terms are eliminated altogether, as in the present formulation, the classification of the system changes from hybrid for subsonic flows (some eigenvalues are real, some are imaginary) to hyperbolic for supersonic flows[27,28].

The boundary conditions for the Newton-Galerkin formulation are introduced in accordance with the theory of characteristics outlined in Chapter 2. The hybrid nature does not create difficulties if the system is treated as the limiting case of a time-dependent formulation as the transient terms vanish. Note that it appears that there are now eight eigenvalues for Eqs. (3.12), however the eigenvalues to be considered are the four vector sums – consistent with the local streamline direction – of the eigenvalues of $\boldsymbol{A}$ and $\boldsymbol{B}$. Typically for the four equation model four types of boundary conditions may be imposed:

a) For a subsonic inlet ρ, u and v are specified.

b) For a supersonic inlet ρ, u, v and e are specified.

c) For a subsonic exit p is specified.

d) For a supersonic exit none of the variables needs to be specified.

The variables that are not constrained must be extrapolated from the interior of the solution domain, a mechanism already implicitly provided by the finite element shape functions.

As already anticipated at the beginning of this section, it is necessary to consider the implications of the simplification introduced by the constant total enthalpy. Consider the steady partial differential equation for energy:

$$\frac{\partial}{\partial x}[u(\rho e+p)]+\frac{\partial}{\partial y}[v(\rho e+p)]=0 \tag{3.14}$$

Before exploring the effect of constant total enthalpy, consider the normal definition of pressure based on energy:

$$p=(\gamma-1)\rho\left(e-\frac{q^2}{2}\right) \tag{3.15}$$

where q denotes the total magnitude of the velocity.

Eq. (3.14) and (3.15) are generally encountered in the four equation model. Substituting Eq. (3.15) into Eq. (3.14) yields:

$$\frac{\partial}{\partial x}\left[u\left(\gamma\rho e-\frac{\gamma-1}{2}\rho q^2\right)\right]+\frac{\partial}{\partial y}\left[v\left(\gamma\rho e-\frac{\gamma-1}{2}\rho q^2\right)\right]=0 \tag{3.16}$$

The next step focuses on showing whether the assumption of constant total enthalpy is true. In this case the pressure can be defined as:

$$p=\frac{\gamma-1}{\gamma}\rho\left(H_\infty-\frac{q^2}{2}\right) \tag{3.17}$$

where H_∞ denotes the freestream total enthalpy. Substituting Eq. (3.17) into Eq. (3.14) yields:

$$\frac{\partial}{\partial x}\left[\frac{u}{\gamma}\left(\gamma\rho e-\frac{\gamma-1}{2}\rho q^2\right)+\frac{\gamma-1}{\gamma}\rho u H_\infty\right]+\frac{\partial}{\partial y}\left[\frac{v}{\gamma}\left(\gamma\rho e-\frac{\gamma-1}{2}\rho q^2\right)+\frac{\gamma-1}{\gamma}\rho v H_\infty\right]=0 \tag{3.18}$$

Introducing Eq. (3.16) into Eq. (3.18) yields the simple equation:

$$\frac{\partial}{\partial x}\left[\frac{\gamma-1}{\gamma}\rho u H_\infty\right]+\frac{\partial}{\partial y}\left[\frac{\gamma-1}{\gamma}\rho v H_\infty\right]=0 \tag{3.19}$$

After applying the chain rule to the partial derivatives and introducing the continuity equation it can be shown that Eq. (3.19) is satisfied identically if γ is a constant. Since it is necessary to assume the validity of Eq. (3.16) to complete the derivation, it is clear that the assumption of constant total enthalpy is valid only for the steady Euler equations. Furthermore even though it is not necessary to solve Eq. (3.14) explicitly, it still is a part of the system of equations and manifests itself in the selection of the boundary conditions.

It would be incorrect to assume that the three equation model has only three eigenvalues; they are in fact still four, including the eigenvalue generated by the energy equation, therefore the Dirichlet boundary conditions are the same of the full system of equations except for the fact that the energy equation is not present. For the three equation model the boundary conditions are introduced according to the following scheme:

- For a subsonic inlet ρ, u and v are specified.
- For a supersonic inlet ρ, u, v are specified.
- For a subsonic exit p is specified.
- For a supersonic exit none of the variables is specified.

Pressure is introduced at the exit boundary through the contour integrals in the two momentum equations, except in the case of a supersonic exit.

The solid wall, or no-penetration, boundary conditions are one of the most elegant features of the Newton-Galerkin formulation. The current practice for finite differences and finite volume schemes requires scaling the two components of velocity at a wall so that the resultant vector points in the tangential direction of the surface, an operation that must be

introduced explicitly and whose accuracy is strongly dependent on the orthogonality of the mesh near the wall [21,29]. In contrast, the Newton-Galerkin formulation imposes no-penetration by simply neglecting the contour integral carrying the term $(\bar{q}\cdot\bar{n})$ in Eq. (3.5a). This term states that the mass flux normal to the wall vanishes, is not affected by the local orthogonality of the mesh, does not require the explicit extrapolation of $\bar{q}$ at the wall and accounts for both x- and y-components of velocity in a single operation.

The last remaining boundary condition involves the determination of the density at a solid boundary. The practice in finite difference or finite volume schemes is to extrapolate the normal derivative of pressure at the wall and obtain the corresponding density from the normal momentum equation. This operation is carried out explicitly and is also dependent on the orthogonality of the mesh. Again the finite element model provides a more elegant approach: the contour integrals containing the term $(\bar{q}\cdot\bar{n})$ in the two momentum equations are evaluated and stored in the global matrix and right-hand side. No further operations are necessary since the shape functions of the finite element method implicitly contribute to the extrapolation of density to the wall and in addition – since the two momentum equations are solved in full form – the correct value of density will be computed. Note that even though the term $(\bar{q}\cdot\bar{n})$ is analytically zero at the wall, the two component of momentum that carry this term may not necessarily be zero numerically in the finite approximation, therefore it would be incorrect to eliminate the contour integrals entirely since their absence would introduce errors in density, on the discrete level, at the wall.

CHAPTER 4

4.1 Quasi-1D Subsonic Flow in a Channel

The following sections describe the details of the quasi-1D numerical tests conducted to verify the time-dependent and Newton-Galerkin codes. All the results for the 1-D test cases are compared to the respective exact solutions. Consider the converging-diverging channel [13] whose area distribution is described by the equation:

$$a = 1 + \frac{2}{25}\left(x - \frac{5}{2}\right)^2 \qquad 0 \le x \le 5 \tag{4.1}$$

The first test case examined is a purely subsonic isothermal flow with an inlet Mach number of 0.4 and incompressible flow as the initial guess. Inlet static temperature and pressure are assumed to be T=290 °K and p=110 kPa. The boundary conditions are ρau known at the inlet and ρa known at the exit, in accordance with the signs of the two characteristics for subsonic inlet and exit conditions. Each test is conducted with 40 equally spaced elements with Δx=0.125 and the iterative procedure is stopped when the L_2-norm of the residual is below 1.0×10^{-6}.

The exact solution can be obtained by combining the continuity and momentum equations and solving for the area as a function of the Mach number as follows:

$$\frac{a_2}{a_1} = \frac{M_1}{M_2} e^{\frac{M_2^2 - M_1^2}{2}} \tag{4.2}$$

Since the channel area is given, the exact Mach number distribution can be found from Eq. (4.2) after solving for M_2 iteratively.

4.1.1 Subsonic Taylor-Galerkin Scheme

The Mach number distribution obtained for the Taylor-Galerkin explicit scheme is shown in Fig. 5. There is virtually no difference between the results of the numerical scheme and the exact solution and no artificial viscosity is required for subsonic flow.

The convergence history, with the value of the residual sampled every 50 iterations, is shown in Fig. 6. The number of iterations required to reach the target convergence limit is 5013. Such slow convergence, typical of explicit Euler schemes, is a symptom of the restrictive limitations imposed on the Courant number by the requirements of numerical stability.

4.1.2 Subsonic Lerat's Exact Method

The Mach number distribution obtained for Lerat's exact implicit scheme is shown in Fig. 7. Again there is virtually no difference between the results of the numerical scheme and the exact solution. The convergence history for the test case is shown in Fig. 8 with the value of the residual sampled at intervals of 10 iterations. A dramatic improvement in the convergence rate with respect to the Taylor-Galerkin scheme is noted, with convergence in 86 iterations. It should be noted that the time per iteration is greater than that of the explicit scheme because the corrector step requires the assembly and decomposition of two additional matrices.

4.1.3 Subsonic Lerat's Approximate Method

The Mach number distribution obtained for Lerat's approximate implicit scheme is shown in Fig. 9. There is no difference between the results of the numerical scheme and the exact solution. The convergence history for the test case is shown in Fig. 10 with the value of

the residual sampled at intervals of 50 iterations. The convergence rate deteriorates with respect to the exact scheme and convergence to the chosen limit requires 648 iterations.

4.1.4 Subsonic Newton-Galerkin Method

This scheme is based on an isentropic formulation. The Mach number distribution obtained for the Newton-Galerkin implicit scheme is shown in Fig. 11. The inlet Mach number is 0.4 and the initial guess is uniform flow. There are no differences between the results of the numerical scheme and the exact solution. For this subsonic test case the artificial viscosity parameters ν_1 and ν_2 are both 0.

The convergence history – shown in Fig. 12 – is quadratic and reaches machine accuracy in 7 iterations. Fig. 12 also demonstrates that the residual cannot decrease below machine limit after iteration 7 and that 10 iterations were completed. Note that only five iterations are required to reach the less demanding convergence limit set for the time dependent schemes.

4.1.5 Performance of the Subsonic Schemes

The details concerning the performance of the various schemes for the subsonic test case can be viewed in Table 1. All the CPU times quoted were measured on the VAX 8550 at Concordia University.

Table 1 Performance comparison for the subsonic tests

Scheme	No. iterations	CPU time (sec.)
Taylor-Galerkin	5013	148
Lerat's Exact	86	7
Lerat's Approximate	648	27
Newton-Galerkin	10	2.68

From Fig. 12 one can observe that for the Newton-Galerkin scheme only five iterations are necessary to reach the same convergence limit imposed on the time-dependent schemes and in this cese the elapsed CPU time would be marginally greater than one second

4.2 Quasi-1-D Transonic Flow in a Channel

This is the most interesting aspect of the testing of the quasi-1-D schemes since the flow can experience a sudden discontinuity in the form of a shock wave.

In order to obtain an exact transonic solution the isothermal shock-jump conditions must be derived from the momentum equation. Denoting the upstream and downstream surfaces of the shock wave with the subscripts u and d respectively, the isothermal Mach number shock jump condition becomes:

$$M_d = \frac{1}{M_u} \tag{4.3}$$

The static pressure jump, a function solely of the upstream Mach number, can be formulated as follows:

$$P_d = P_u M_u^2 \tag{4.4}$$

Eqs. (4.2) to (4.4) are sufficient to determine the Mach number distribution in the nozzle for a predetermined back pressure.

The throat-to-inlet area ratio defines the choking Mach number as 0.4468 and the selected inlet and back pressures are P_f=110 kPa and P_b=100 kPa which produce a shock located at x=4.1043. Note that even for the exact solution the shock location is determined iteratively until the desired back pressure is satisfied.

The initial guess is again obtained by linearly interpolating ρa between the inlet and exit values and setting the distribution proportional to the inverse of the channel area, while $\rho a u$ is held constant throughout. For the isothermal formulation the back pressure must be converted to the corresponding value of density which can be easily computed from the ideal gas law. The boundary conditions are the same as those of the subsonic test case since the boundaries still experience a locally subsonic flow.

4.2.1 Transonic Taylor-Galerkin Scheme

This test case requires the introduction of artificial viscosity to suppress the non-physical expansion shock that would otherwise be captured. The Mach number distribution obtained is shown in Fig. 13. There are some noticeable oscillations before and after the shock, caused by a low value of the artificial viscosity parameter. These oscillations would disappear if more artificial viscosity were introduced, however the shock would be smeared over several elements. The convergence history for the test case is shown in Fig. 14. Convergence to the preset limit is achieved in 1713 iterations.

4.2.2 Transonic Lerat's Approximate Method

This scheme does not allow control of the level of artificial viscosity introduced. The Mach number distribution obtained is shown in Fig. 15. There is an overshoot in the distribution

just upstream of the shock, apparently caused by the misalignment of the elements with respect to the exact shock location, however the shock is captured within a single element. The convergence history for the test case is shown in Fig. 16. Convergence to the preset limit is achieved in 393 iterations.

4.2.3 Transonic Newton-Galerkin Method

This scheme allows control of the level of artificial viscosity introduced, a very important feature that can be exploited to overcome the convergence problems encountered when Newton's method is started on a poor initial guess. The Mach number distribution obtained for this isentropic test case is shown in Fig. 17. The inlet Mach number is M_∞=0.43025, the inlet static pressure is p=101 kPa and the back pressure is p_b=90 kPa.

The uniform flow initial guess is not close enough to the final solution and Newton's method will not converge. The artificial viscosity parameter is used to overcome this situation. The iterative procedure is started with a high value of μ until the residual drops to an intermediate limit, say 10^{-3}, then the value of μ is decreased and the iterative procedure is restarted from the previous results, until the intermediate residual limit is reached again. This cycle is repeated until the final value of μ is introduced, in which case the iterative procedure is terminated only when the residual drops to machine limit.

The convergence history for the test case is shown in Fig. 18. Convergence to machine limit is achieved in 13 iterations with 2 global iterative cycles and values of μ=7.0 and 3.2. The final value of μ corresponds to ν_1=0.02186 and ν_2=0.01807.

4.2.4 Performance of the Transonic Schemes

The details concerning the performance of the various schemes for the transonic test case can be viewed in Table 2. All the CPU times quoted were measured on the VAX 8550 at Concordia University.

Table 2 Performance comparison for the transonic tests

Scheme	No. iterations	CPU time (sec.)
Taylor-Galerkin	1713	58
Lerat's Approximate	393	17
Newton-Galerkin	13	2.9

4.3 Influence of Grid Adapting on Convergence and Accuracy

The introduction of a grid adapting routine in the iterative procedure of the Euler schemes has some beneficial effects. This technique attempts to decrease the truncation error introduced by the discretization schemes by refining the mesh where the gradients of the solution are large. The truncation error is proportional to the mesh size and the higher order derivatives of the solution; while no control can be exerted on the higher order derivatives, the truncation error can be reduced by a local refinement of the mesh, at the expense of the size of the elements in regions where the error is small. In order to improve the accuracy of the results three mesh adapting methods are available,:

a) Mesh refinement through the introduction of additional elements.

b) Mesh refinement through the relocation of the nodes of the elements.

c) Introduction of additional nodes within an element to switch to higher order shape functions.

All three methods have favorable and unfavorable characteristics. For example, case a) requires a complete revision of the nodal connectivity table and the addition of the extra

elements increases the computational effort. This method is extendable to 2-D and 3-D formulations only in conjunction with triangular and tetrahedral elements respectively. Method b) requires the recalculation of the shape function derivatives. Method c) is suitable only for the finite element method and requires both a revision of the nodal connectivity table and the recalculation of the shape function derivatives. Furthermore it is not well suited to the simulation of phenomena that include sharp discontinuities in the solution, as in the case of transonic flows. In view of the potential for extension to 2-D quadrilateral elements, a variant of method b) was selected.

This mesh adapting scheme is based on a spring analogy developed by Nakahashi and Deiwert [30]. The advantage of this approach is that the minimum and maximum mesh spacings are controllable and the spring constants are a function of any one of the fluid properties, in this case the gradient of the Mach number.

4.3.1 Grid Adapting Transonic Taylor-Galerkin Test Case

The initial guess and the back pressure are unchanged from the non-adapting test case. The Mach number distribution obtained is shown in Fig. 19. Note that the pre-shock oscillations have virtually disappeared. The convergence history for this test case is shown in Fig. 20. Convergence to the pre-set limit occurs in 1554 iterations. The convergence history shows three spikes that occur when the residual drops below 10^{-3}, 10^{-4} and 10^{-5} which correspond to the preset limits for the grid refinements. The minimum element size is 2, 4, 8 times smaller than the uniform mesh spacing for each successive grid refinement respectively. The spikes in the convergence curve are caused by the linear interpolation of the nodal variables from one grid to the next In spite of this simplistic approach the self-adapting Taylor-Galerkin scheme converges faster than the non-adapting method in terms of the number of iterations, however the CPU time required increases slightly due to the iterative nature of the mesh adapting mechanism.

4.3.2 Grid Adapting Transonic Lerat's Test Case

This scheme exhibits the most dramatic improvement in conjunction with the mesh adapting routine, as illustrated by the Mach number distribution shown in Fig. 21. The convergence history for this test case is shown in Fig. 22. Convergence to the preset limit requires 479 iterations. Note that the pre-shock oscillation has virtually disappeared and the shock is captured over a single element. The convergence history shows three spikes that occur when the residual drops below the mesh refinement limits. Unfortunately the approximate Lerat's method shows a marked deterioration in the overall convergence rate and execution time with respect to the non-adapting method.

4.3.3 Grid Adapting Transonic Newton-Galerkin Test Case

The Mach number distribution is shown in Fig. 23 while the convergence history for the test case is shown in Fig. 24. Convergence to the preset limit requires 17 iterations. Note that the shock sharpness has improved as expected. The convergence history shows the three spikes that occur when the artificial viscosity parameter is decreased and the mesh refinement takes place; moreover it is evident that within each global iterative step the convergence rate is always quadratic. The intermediate values of μ selected for this test case are 4.0, 2.0 and the final value is 1.45, corresponding to the values ν_1=0.009907 and ν_2=0.008189, which are considerably lower than for the non-adapting test case. Even in this case the timing indicates that the total execution time deteriorates when the grid adapting is combined with an implicit scheme

4.3.4 Influence of Grid Adapting on Performance

The details concerning the performance of the various schemes for the grid adapting transonic test case can be viewed in Table 3. All the CPU times quoted were measured on the VAX 8550 at Concordia University.

Table 3 Performance comparison for the grid adapting tests

Scheme	No. iterations	CPU time (sec.)
Taylor-Galerkin	1554	62
Lerat's Approximate	479	53
Newton-Galerkin	17	4

4.4 Comparison of the 1-D Schemes

The results of the test cases discussed in the previous sections are not sufficient for a detailed comparison of the four Euler schemes, however some conclusions can be drawn with respect to the effectiveness of each method.

The Taylor-Galerkin scheme is one of the workhorses of FEM CFD, however it is beginning to lose favour because of its notoriously poor convergence rate. This flaw requires the introduction of the multigrid acceleration technique in order to speed up convergence. While this technique is based on a simple concept, its practical implementation is quite complex and cumbersome. It appears that Lerat's exact method is much simpler and quicker to introduce than multigrid acceleration, however the absence of artificial viscosity in this scheme prevents its extension to the solution of transonic flows. The approximate method is not as quick, however the decay in convergence rate is offset by the high accuracy of the solution, particularly the high resolution of shocks. Note that the accuracy of the solution is sensitive to the mesh spacing distribution and the small overshoot before the shock was eliminated with the introduction of the self-adapting mesh refinement method

The Newton-Galerkin method is considerably faster than any of the time marching procedures, even more than it appears from a superficial examination of the number of iterations or the CPU times quoted in Tables 1-3. It must be underlined that the Newton-Galerkin test cases where started with uniform flow as the initial guess and are converged to machine limit, as opposed to the incompressible solution and the convergence limit set at 10^{-6} for the time-marching schemes. The time-marching schemes would require a considerable increase of computational effort if they were run under the constraints of the Newton-Galerkin scheme, furthermore they do not offer a clear indication of the value of the residual and the convergence is measured on the values of ΔU.

The Newton-Galerkin scheme shows that the introduction of a linear artificial viscosity model produces shocks smeared over several elements. A non-linear model would certainly improve the resolution of sharp gradients, however the investigation of different artificial viscosity models was not intended to be the subject of this Thesis.

4.5 High speed flow in 2-D channels

This section is the summary of several internal flow tests conducted to evaluate the Newton-Galerkin scheme in two dimensions. Two types of channels are considered:

- A short channel with a 10% thick circular arc bump of length 1.0 with an inlet and exit sections of the same length and height of 1.0. The finite element grid is 64X16 for a total of 1024 elements and 1105 nodes.

- A short channel with the same dimensions and grid of the previous channel but with a 4% circular arc bump.

These channels have become standard tests for Euler schemes and results for the various test cases are readily available in the literature.

4.5.1 Subsonic flow in a channel with a 10% circular arc bump

The geometry and details of the finite element grid for this channel are shown in fig 25. Note that the grid is clustered in the y-direction near the wall to improve the interpolation of the values of density from the interior of the channel to the wall.

The initial conditions of this test case are uniform flow at M_∞=0.5 with inlet static pressure and temperature set at 100 kPa and 288°K respectively. The following boundary conditions are applied:

- At the inlet ρ, u and v must be specified
- At outflow p is introduced through the pressure contour integrals in the momentum equations
- At boundaries where p is unknown the pressure contour integrals must be recast in terms of H_∞, ρ, u and v following Eq. (3.3d)
- The contour integral containing the $(\vec{q}\cdot\vec{n})$ term in the continuity equation vanishes identically on walls
- All other contour integrals must be evaluated everywhere

The contours of constant Mach number are shown in Fig. 26. The Mach number distributions on the upper and lower walls are compared to the results of Ni [7] in Fig. 27, showing excellent agreement.

Quadratic convergence to machine accuracy, shown in Fig. 28, is attained in 6 iterations, requiring 3 min 32 sec CPU time. The timing of the execution indicates that for each iteration the assembly of the global matrix requires approximately 12 sec and the factorization and solution require 21 sec while the impact of all the other operations performed during the iteration is negligible. A single global iteration on the artificial viscosity parameter is required, with the value $\mu = 0.1$ resulting in the coefficients $\nu_1 = 0.0005879$ and $\nu_2 = 0.0004860$.

4.5.2 Transonic flow in a channel with a 10% circular arc bump

The initial conditions of this test case are uniform flow at $M_\infty = 0.675$ with inlet static pressure and temperature set at 100 kPa and 288 °K respectively. At the outflow boundary the value of pressure is required: since the channel will not choke, the static pressure is again set to the inflow value. The boundary conditions are the same used in sec.4.5.1.

The contours of constant Mach number are shown in Fig. 29, where a shock is now clearly visible near the trailing edge of the bump. The Mach number distributions on the upper and lower walls are compared to the results of Ni [7] in Fig. 30, again showing excellent agreement.

Quadratic convergence to machine accuracy, shown in Fig. 31, requires in 9 iterations, equivalent to 4 min 44 sec CPU time on a VAX 8550 with a standard banded Gauss elimination solver. Note that the residual oscillates during the first iterations until the shock location is captured accurately. A single global iteration on the artificial viscosity parameter is required, with the value set at $\mu = 0.55$ resulting in the coefficients $\nu_1 = 0.002395$ and $\nu_2 = 0.001980$.

4.5.3 Supersonic flow in a channel with a 4% circular arc bump

The geometry and the detail of the finite element grid for this channel are shown in Fig 32. Note that aside for the thinner bump the configuration is identical to that of Fig.25.

The initial conditions of this test case are uniform flow at $M_\infty = 1.4$ with inlet static pressure and temperature set at 100 kPa and 288 °K respectively. At the outflow boundary the value of pressure is unknown: since the flow is purely supersonic the static pressure in the contour integrals is recast in terms of the three dependent variables and H_∞ using Eq. (3.3d); aside from the pressure, all other boundary conditions follow the procedure outlined in sec. 4.5.1.

The contours of constant Mach number are shown in Fig. 33. Note the two oblique shocks at the leading and trailing edges of the bump. The leading edge shock should reflect on the upper surface before vanishing in the expansion fan over the bump, however the grid is too coarse to capture the details of the reflecting shock. The Mach number distributions on the upper and lower walls are compared to the results of Ni [7] in Fig. 34, showing good agreement.

Quadratic convergence to machine accuracy, shown in Fig. 35, is attained in 6 iterations, requiring 3 min 4 sec CPU time. Note that the convergence curve does not show oscillations since the two oblique shocks are relatively weak. A single global iteration on the artificial viscosity parameter is required, with the value $\mu = 2.5$ resulting in the coefficients $\nu_1 = 0.005249$ and $\nu_2 = 0.004339$.

4.6 High speed external flow: the AGARD02 test case

The AGARD02 test case is the second in a series of five tests for the evaluation of the performance of Euler solvers applied to external lifting flows [31]. The lifting body is the familiar NACA 0012 airfoil set at 1.0° angle of attack.and the far-field flow speed is set at $M_\infty = 0.85$.

The NACA 0012 does not have a closed trailing edge at the unit chord length, rather the trailing edge is considered to be closed at $c_{TE} = 1.008930411365$ where the thickness of the trailing edge is less than 10^{-13}. For this test case the airfoil must be constructed with a closed trailing edge and subsequently rescaled to unit chord length to ensure consistency with the published results.

Two possible types of grids can be constructed around an airfoil:

- O-grids are constructed by mapping the airfoil to a circle which becomes the starting point for a radial mesh. When mapped back to the original physical plane the elements are clustered around the leading and trailing edges with poor control of the element size on the surface of the airfoil. The elements surrounding the trailing edge are usually badly skewed, particularly if the trailing edge is cusped. This type of mesh is ideal in conjunction with schemes that require a coordinate mapping.

- C-grids do not require any mapping. They are constructed by means of simple algebraic formulae or with the help of variational principles to maximize orthogonality and smoothness. This type of grid offers optimal control of the orthogonality and dimension of the elements in the proximity of the trailing edge, provides a more efficient clustering of the elements on the wake line for cases which require that a slip line or a complex wake be modelled.

For this particular experiment the logical choice is a C-grid with 254 bilinear elements wrapped around and 30 elements in the radial direction for a total of 7620 elements and 7879 nodes; the airfoil itself is surrounded by 204 elements and 204 nodes. The far-field boundary of the finite element grid is at 30 chords from the surface of the airfoil. The full finite element grid is shown in Fig. 36 where the airfoil – situated at the center of the picture – is barely visible, however a detail of the airfoil and its surrounding elements is shown in Fig. 37.

The initial conditions are uniform flow everywhere and the inflow static pressure and temperature are 100 kPa and 288°K respectively. Fig.38 shows a schematic C-grid for the purpose of illustrating the application of the boundary conditions which are imposed as follows:

- At the far-field boundary, segment ABC, ρ, u and v must be specified
- At the outflow, segment AC, p is introduced through the pressure contour integrals of the momentum equations
- At the airfoil surface the contour integral containing the term $(\bar{q}\cdot\hat{n})$ in the continuity equation vanishes identically
- At the airfoil surface where p is unknown the pressure contour integrals must be recast in terms of H_∞, ρ, u and v following Eq. (3.3d)
- All other contour integrals must be evaluated everywhere
- No Kutta condition is imposed across the trailing edge

The Mach number contours are shown in Fig. 39. The two shocks on the airfoil can be clearly seen. Their unequal strengths cause a peculiar phenomenon: the static pressure is

fixed at the outflow boundary and the static pressure at the trailing edge of the airfoil is continuous from the upper to the lower surface, therefore the velocity of the fluid must be discontinuous across the wake since the total pressure loss across the shock on the upper surface is higher than that produced across the other shock. The C-grid permits to capture this slip line much more accurately than an O-grid.

Fig. 40 shows that the constant pressure contours are smooth across the wake, therefore the static pressure is continuous across the wake and the slip line occurs only in the velocity variables. Fig. 41 compares the values of C_p on the surface of the airfoil to the results of Jameson found in the original AGARD report, showing good agreement. Fig. 42 shows the same values compared to the results of Pulliam [29] which were too late to be included in the AGARD report.

It should be noted that Pulliam's original contribution to the AGARD report did not produce accurate results, however Pulliam re-evaluated all the test cases at a later time with an improved version of his implicit finite difference code ARC2D using 561X65 grids (36465 nodes!) on a CRAY-XMP. These grids are heavily clustered near the shocks and across the wake line, accounting for most of the improvement in the accuracy of his results. To this day these numerical results are the most accurate, but for our purpose solutions on grids of this nature are outside the performance range of the available computers.

Fig. 43 shows the convergence curve. Three iterations on the value of μ are required since the flow exhibits several discontinuities: two shocks, a slip line and a leading edge stagnation point. The intermediate values of μ are 5.0 and 0.75, the final value is 0.25 which leads to $\nu_1 = 0.0008646$ and $\nu_2 = 0.0007147$. A total of 17 iterations are completed and the convergence history shows that convergence is always quadratic. The intermediate convergence limits are set at 10^{-5} and the results are converged to machine accuracy.

The computation was performed on a Silicon Graphics Power Series IRIS 4D/240GTX with 4 processors with clock frequency of 25Mhz. The matrix assembly time requires approximately 55 sec CPU time, the solution by a banded Gauss elimination algorithm requires 330 sec. and the total CPU time per iteration is 385 sec.

4.7 Conclusions

In the previous chapters a finite element scheme for the solution of the steady Euler equations was presented: this new formulation takes full advantage of the power of the finite element method to introduce improvements in areas in which the finite difference and finite volume method are weak. In particular the recovery of the natural boundary conditions in the form of flux contour integrals and the implicit accounting on the boundary of the extrapolation of variables that do not require a Dirichlet boundary condition can be considered extremely important. The boundary extrapolation technique is carried out implicitly so that the Euler equations are actually solved at the boundary, compared to the extrapolation procedures used in conjunction with the other two methods which must solve either a one-dimensional local approximation to the Euler equations (Riemann invariants) or do not solve the equations at all (linear extrapolation).

The solutions of the test cases shown in this chapter show good agreement with the results found in the literature. Clearly Newton's method is the most efficient algorithm for the linearization of hyperbolic systems of equations when the steady-state solution is the objective. The artificial viscosity adopted for the finite element scheme is based on a linear model and not ideally suited to capture sharp discontinuities. This model can be easily replaced with a more sophisticated one and in the limit it is possible to construct a high resolution TVD[32,33] version of the scheme, although the linear model should be retained

as the starting block for the continuation procedure necessary to overcome the instability of Newton's method caused by poor initial guesses.

CHAPTER 5

5.1 Consequences of the Non-Uniqueness of the Potential Formulation

The discovery of the non-uniqueness of the Potential formulation [2] generated a considerable amount of debate in the CFD community and caused a shift in favor of the solution of the Euler equations in primitive variable form, thought to yield a unique solution. It should be underlined that the appearance of multiple solutions in the Potential formulation is a phenomenon limited to some conditions and in general it cannot be observed in smooth flows but only in certain transonic regimes of flow around an isolated airfoil. Hafez et al. [3] and Habashi et al. [4] have shown that the spurious solutions are generated by the absence of the correct shock jump conditions and that the introduction of the Rankine-Hugoniot shock conditions for the calculation of density completely eliminates the appearance of multiple solutions. In spite of all the turmoil provoked by the multiple solutions considerable research is still being conducted on the Potential formulation [34,35] which is deemed attractive for its simplicity, a far cry from the complex environment of the Euler or Navier-Stokes schemes.

Following the problems encountered with the Potential formulation it is only logical to question the uniqueness of the solutions of the Euler and Navier-Stokes equations. Not surprisingly some papers have already started to appear on the subject.

5.2 Non-Uniqueness of the Discrete Euler Solvers

Although it is possible to prove that smooth solutions of the Euler equations are unique, to the present day no mathematical theory can analyze the uniqueness of the solutions of the

inviscid and viscous equations of gas dynamics in the presence of a discontinuity. In the following discussion two specific classes of non-unique solutions will be distinguished: the first arises from the non-uniqueness of the discrete system of equations, the second deals with the nature of the partial differential equations.

Salas et al. [36] have analyzed some model equations and the quasi 1-D Euler equations and shown that the boundary approximations of the discrete system of equations, as well as large time steps for implicit schemes, may induce spurious solutions. Stephens [37] has shown that some finite difference schemes may lead to non-unique solutions and that while a Galerkin approximation to a non-homogeneous model equation gives unique solutions, the corresponding central difference approximation produces multiple ones. These two examples are considered as multiple solutions of the first kind as defined above since they stem entirely from the discrete systems and say nothing about the PDEs themselves.

The non-uniqueness problem is quite serious since for several space dimensions it is nearly impossible to find exact solutions to test cases that provide the necessary foundation for the comparison of results, hence the doubt concerning the validity of a particular scheme is never completely cleared.

It is possible to show that the steady Euler equations produce multiple solutions for a particular class of problems. The following sections illustrate this non-unique behavior of the second kind.

5.3 Non-Uniqueness of the Euler Equations

Consider the flow in a converging-diverging nozzle. Several operating ranges are possible:

a) subsonic inlet flow, nozzle not choked, subsonic outflow

b) subsonic inlet flow, nozzle choked, subsonic outflow

c) subsonic inlet flow, nozzle choked, supersonic outflow

d) supersonic inlet flow, nozzle choked, subsonic outflow

e) supersonic inlet flow, nozzle choked, supersonic outflow

If a back pressure other than the corresponding isentropic exit pressure is specified a compression shock can be observed in the divergent portion of the nozzle. The steady Euler equations, however, are capable of supporting a stable compression shock both in the convergent and divergent sections of the nozzle for the same boundary conditions but with different initial guesses. A stability analysis of the shock in the convergent section reveals that this shock is unstable and will move out towards the inlet or the exit if its position is slightly perturbed in those directions. Hafez, Palaniswamy and Mariani [19] have demonstrated this phenomenon via a quasi 1-D finite differences scheme, but the occurrence of multiple solutions in 2-D has not been demonstrated before.

A numerical experiment is conducted on the supersonic inflow in a nozzle with a 15% restriction, having a profile described by a cosine function and a length of five inlet diameters. An illustration of the nozzle discretized by 100 X 30 elements is shown in Fig 44. The choice of the cosine function is deliberate: a sharp corner on the inlet plane of the nozzle would generate a conical oblique shock in 3-D which would reflect inside the nozzle and form a complex pattern of compression and rarefaction waves, with no possible normal shocks in the converging or diverging sections.

The critical supersonic inlet Mach number for this restriction is $M_{ci} = 1.50$ ($\gamma = 1.4$). A higher inlet Mach number would generate the necessary conditions for this experiment, consequently it is fixed at $M_i = 1.65$ and the inlet static pressure is set at an arbitrary value

of 1 bar. A smooth, fully supersonic solution can be obtained by not constraining the exit pressure and a shock can be captured if the back pressure is selected with a value higher than the isentropic one. In this case the desired pressure ratio between inlet and exit was fixed at 3.4. A smooth, fully subsonic solution, can be generated with an inlet pressure of 3.4 bar and an inlet Mach number lower than the subsonic critical value.

The two smooth solutions can be spliced in different locations to construct two initial guesses, one with a shock in the converging section and one with a shock positioned in the diverging section. These two initial sets of values are used to initialize the Newton-Galerkin Euler solver to capture multiple solutions for the same boundary conditions.

The Mach number distributions of the two shocks are shown in Fig. 45 and 46, compared to the exact quasi 1-D solutions. Fig 47 and 48 show the Mach number and static pressure contours for the two solutions as well as the Prandtl-Meyer compression and expansion fans at the inlet of the nozzle. Both solutions converge to machine limit in 6 iterations.

The time marching algorithm of Eqs. (3.11) can analyze the stability of the two solutions when the shock location is perturbed. In the first example the unstable shock is displaced towards the inlet of the nozzle. The time marching code shows that the new initial guess is unstable and the shock moves toward the inlet. The three frames of Fig. 49 illustrate the motion through the Mach number contours. The three frames in Fig. 50 show the motion of the unstable shock after being displaced towards the throat; the shock is swallowed by the throat, reemerges in the divergence section and eventually settles down in the stable position. Finally, if the shock is displaced near the outflow boundary it tends to move upstream and settle in the stable position, as shown in Fig. 51.

Fig. 52 to 54 show a more detailed correlation of the shock location as a function of time. It should be remarked that the time marching code is run with a constant time step. Fig. 55 to 57 show the residuals as a function of time: clearly the solution with the unstable shock

moves towards the inlet and never converges; the solution with the shock moving downstream as well as the one with the shock moving upstream from the exit to the stable position do not converge until the shock arrives to the stable location.

5.4 Consequences of the Non-Uniqueness of the Steady Euler Equations

At the present time an analysis of the consequences of the non-uniqueness of the steady Euler equations is limited to speculation. Solutions to several test cases have been shown and other results that do not appear in this thesis have been obtained. The multiple solutions, however, have been demonstrated only in supersonic convergent-divergent nozzles, both with the 1-D and 2-D finite element schemes. If any doubts regarding the multiplicity of the solutions should arise, the time marching analysis of the results is sufficient to verify the stability of the steady solution.

REFERENCES

[1] South, J.C., "A Historical Perspective and Overview of Computational Transonics," *Advances in Computational Transonics*, W.G. Habashi (Ed), Pineridge Press, Swansea, 1985, pp. 1-20.

[2] Salas, M.D., Jameson, A. and Melnik, R.E., "A Comparative Study of the Nonuniqueness Problem of the Potential Equation," AIAA Paper 83-1888, Danvers, Massachusetts, 1983.

[3] Hafez, M., South, J. and Murman, E., "Artificial Compressibility Methods for Numerical Solutions of Transonic Full Potential Equation," *AIAA Journal*, Vol. 17, August 1979, pp. 838-844.

[4] Habashi, W.G., Hafez, M.M. and Kotiuga, P.L., "Computation of Choked and Supersonic Turbomachinery Flows by a Modified Potential Method," *AIAA Journal*, Vol. 23, February 1985, pp.214-220.

[5] Hafez, M. and Lovell, D., "Numerical Solution of Transonic Stream Function Equation," *AIAA Journal*, Vol. 21, No. 3, March 1983, pp.327-335.

[6] Habashi, W.G. and Hafez, M.M., "Finite Element Stream Function Solutions for Transonic Turbomachinery Flows," AIAA Paper 82-1268, Cleveland, Ohio, June 1982.

[7] Ni, R., "A Multiple Grid Scheme for Solving the Euler Equations," AIAA Paper 81-1025, Palo Alto, California, 1981.

[8] Jameson, A., "Numerical Solution of the Euler Equation for Compressible Inviscid Fluids," in: *Numerical Methods for the Euler Equations of Fluid Dynamics*, F. Angrand et al. (Eds), SIAM, Philadelphia, 1985, pp. 199-245.

[9] Beam, R.M. and Warming, R.F., "An Implicit Finite-Difference Algorithm for Hyperbolic Systems in Conservation-Law Form," Journal of Computational Physics, Vol. 22, 1986, pp. 87-110.

[10] Pulliam, T.H. and Steger, J.L., " Implicit Finite Difference Simulation of Three-Dimensional Compressible Flow," *AIAA Journal*, Vol. 18, No. 2, February 1980, pp.159-167.

[11] Fletcher, C.A.J., "A Primitive Variable Finite Element Formulation for Inviscid, Compressible Flow," *Journal of Computational Physics*, Vol. 33, 1979, pp. 301-312.

[12] Donea, J., "A Taylor-Galerkin Method for Convective Transport Problems," *International Journal for Numerical Methods in Engineering*, Vol. 20, 1984, pp.101-119.

[13] Löhner, R., Morgan, K. and Zienkiewicz, O.C., "The Solution of Non-Linear Hyperbolic Equation Systems by the Finite Element Method," *International Journal for Numerical Methods in Fluids*, Vol. 4, November 1984, pp. 1043-1063.

[14] Angrand, F., et al., "Transonic Euler Simulations by Means of Finite Element Explicit Schemes," AIAA Paper 83-1924, Danvers, Massachusetts, 1983.

[15] Stoufflet, B., "Implicit Finite Element Methods for the Euler Equations," in: *Numerical Methods for the Euler Equations of Fluid Dynamics*, F. Angrand et al. (Eds), SIAM, Philadelphia, 1985, pp. 409-434.

[16] Tezduyar, T.E. and Hughes, T.J.R., "Finite Element Formulations for Convection Dominated Flows with Particular Emphasis on the Compressible Euler Equations," AIAA Paper 83-0125, Reno, Nevada, 1983.

[17] Akay, H.U., Ecer, A. and Willhite, P.G., "Finite Element Solutions of Euler Equations for Lifting Airfoils," *AIAA Journal*, Vol. 24, April 1986, pp.562-569.

[18] Bruneau, C.H., Laminie, J. and Chattot, J.J., "Computation of 3D Vortex flows Past a Flat Plate at Incidence Through a Variational Approach of the Full Steady Euler Equations," *International Journal for Numerical Methods in Fluids*, Vol. 9, March 1989, pp. 305-323.

[19] Hafez, M., Palaniswamy, S. and Mariani, P., "Calculation of Transonic Flows with Shocks Using Newton's Method and Direct Solver, Part II," AIAA Paper 88-0226, Reno, Nevada, 1988.

[20] Hafez, M. and Lovell, D., "Entropy and Vorticity Corrections for Transonic Flows," *International Journal for Numerical Methods in Fluids*, Vol. 8, January 1988, pp. 31-53.

[21] Pulliam, T.H., "Implicit Finite-Differenece Methods for the Euler Equations," in: *Advances in Computational Transonics*, W.G. Habashi (Ed), Pineridge Press, Swansea, 1985, pp. 503-542.

[22] Chakravarthy, S.R., "Euler Equations-Implicit Schemes and Boundary Conditions," *AIAA Journal*, Vol. 21, March 1983, pp. 699-706.

[23] Yee, H.C., Beam, R.M. and Warming, R.F., "Boundary Approximations for Implicit Schemes for One-Dimensional Inviscid Equations of Gasdynamics," *AIAA Journal*, Vol. 20, September 1982, pp. 1203-1211.

[24] Lerat, A., "Implicit Methods of Second-Order Accuracy for the Euler Equations," *AIAA Journal*, Vol. 23, January 1985, pp. 33-40.

[25] Zienkiewicz, O.C., "The Finite Element Method," McGraw-Hill, New York, 1983, pp. 189-190.

[26] Burden, R.L., Faires, J.D. and Reynolds, A.C., "Numerical Analysis," Prindle, Weber & Schmidt, Boston, 1981, pp. 165-176.

[27] Anderson, D.A., Tannehill, J.C. and Pletcher, R.H., "Computational Fluid Mechanics and Heat Transfer," McGraw-Hill, New York, 1984, pp. 31-35.

[28] Dick, E., "The Calculation of Steady Transonic Flow by Euler Equations with Relaxation Methods," in: *Computational Methods for Turbulent, Transonic, and Viscous Flows*, J.A. Essers (Ed), Springer-Verlag, New York, 1983, pp. 291-349.

[29] Pulliam, T.H. and Barton, T.J., "Euler Computations of AGARD Group 07 Airfoil Test Cases," AIAA Paper 85-0018, Reno, Nevada, 1985.

[30] Nakahashi, K. and Deiwert, G.S., "Self-Adaptive-Grid Method with Application to Airfoil Flow," *AIAA Journal*, Vol. 25, No. 4, April 1987, pp. 513-520.

[31] AGARD Working Group 07, "Test Cases for Inviscid Flow Field Methods," AGARD -AR-211, 1985.

[32] Yee, H.C.and Harten, A., "Implicit TVD Scemes for Hyperbolic Conservation Laws in Curvilinear Coordinates," *AIAA Journal*, Vol. 25, No. 2, February 1987, pp.266-274.

[33] Sweby, P.K., "Flux Limiters," in: *Numerical Methods for the Euler Equations of Fluid Dynamics*, F. Angrand et al. (Eds), SIAM, Philadelphia, 1985, pp. 48-65.

[34] Hafez, M., Whitlow, W. and Osher, S., "Improved Finite-Difference Schemes for Transonic Potential Flow Calculations," *AIAA Journal*, Vol. 25, No. 11, November 1987, pp.1456-1452.

[35] Volpe, G. and Jameson, A., "Transonic Potential Flow Calculations by Two Artificial Density Methods," *AIAA Journal*, Vol. 26, No. 4, April 1988, pp.425-429.

[36] Salas, M.D., Abarbanel, S. and Gottlieb, G., "Multiple Steady-States for Characteristic Initial Value Problems," ICASE report no. 84-57.

[37] Stephens, A.B., "Multiple Solutions of Finite Difference Approximations to Some Steady Problems of Fluid Dynamics," Proceedings of the 10th IMACS World Congress on System Simulation and Scientific Computation, Montreal, 1982, Vol 1, pp. 218-220.

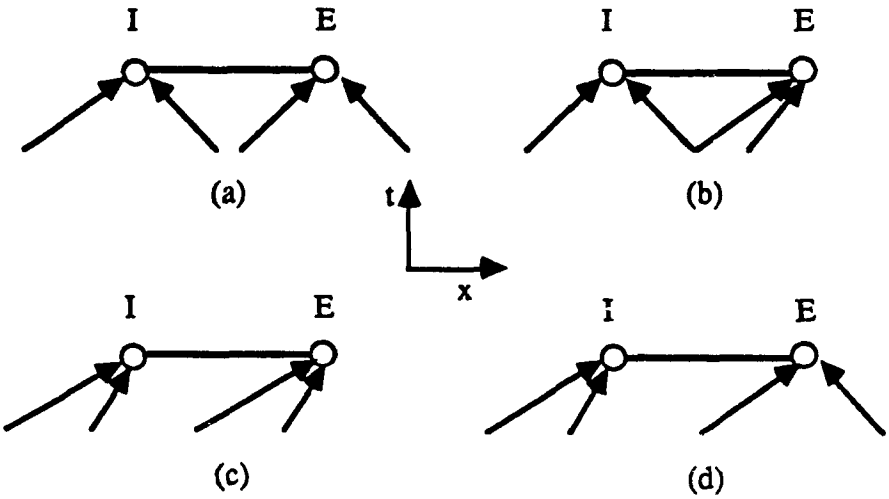

Fig. 1 Influence of the characteristics on an element

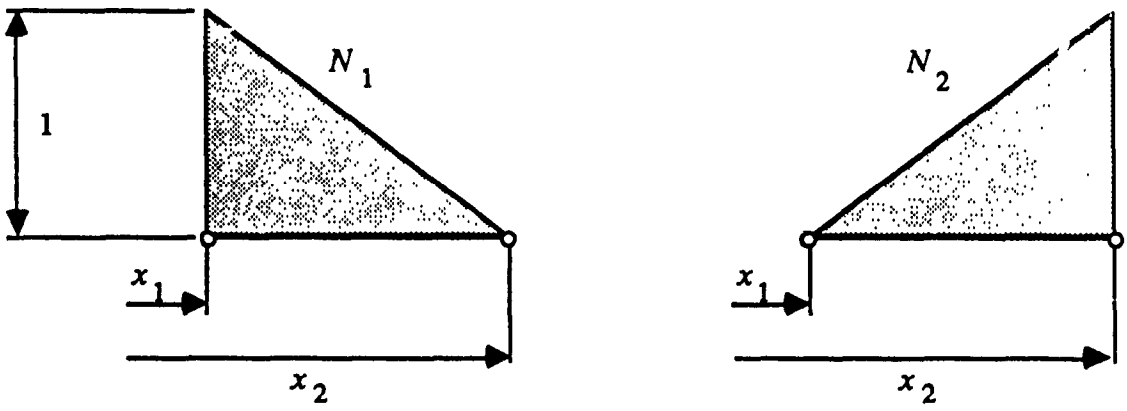

Fig. 2 Dimensional shape functions for linear 1-D elements

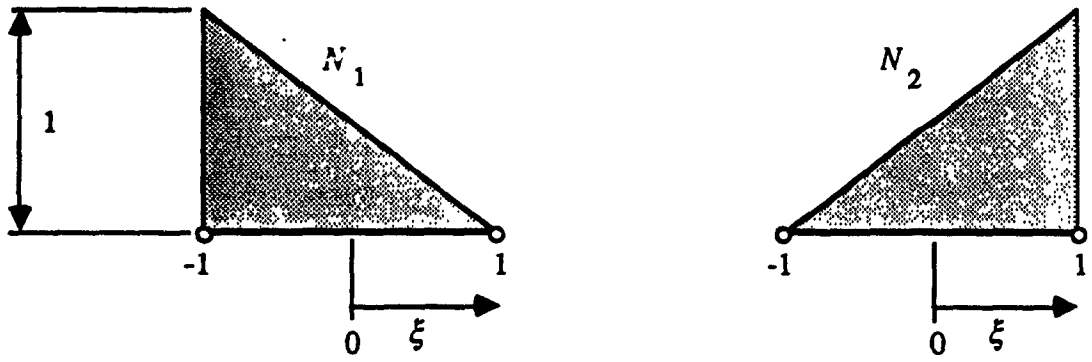

Fig. 3 Non-dimensional shape functions for linear 1-D elements

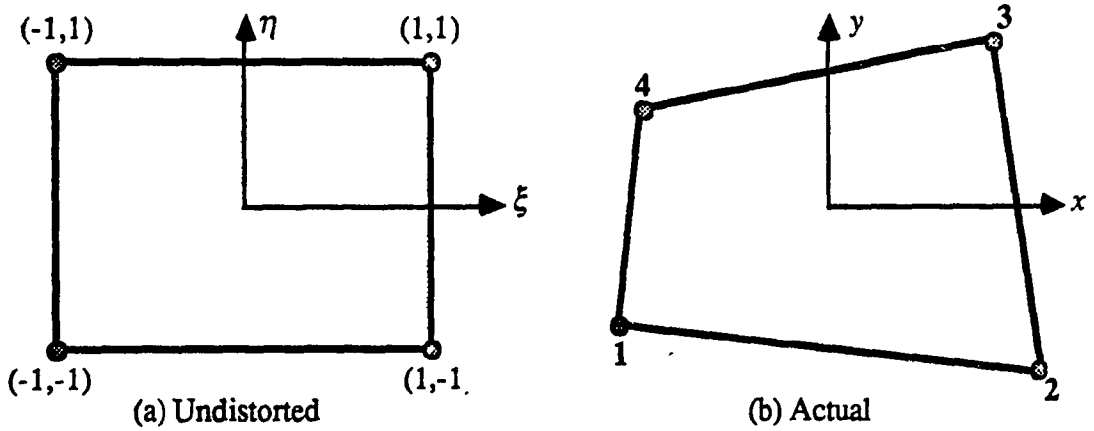

Fig. 4 2-D Element transformation

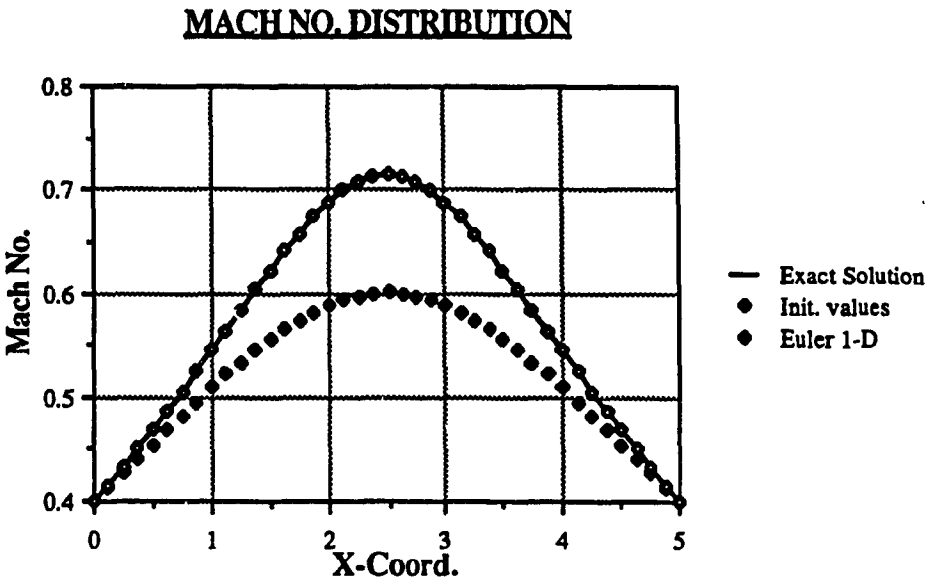

Fig. 5 Taylor-Galerkin subsonic test case

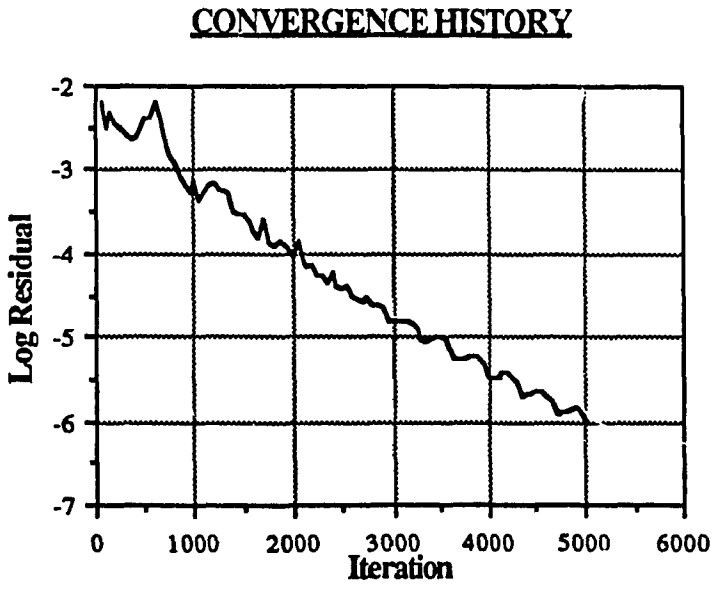

Fig. 6 Convergence history of the Taylor-Galerkin subsonic test case

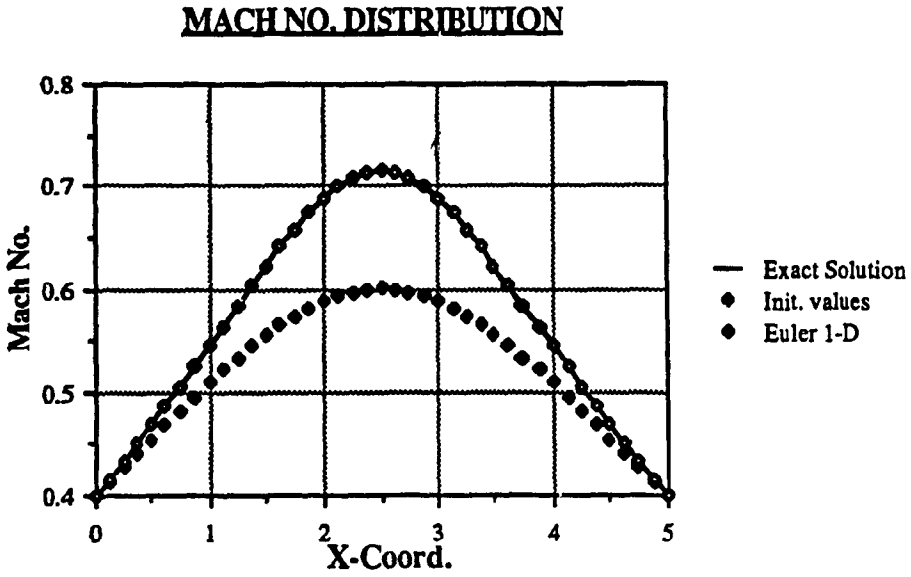

Fig. 7 Lerat's Exact Method subsonic test case

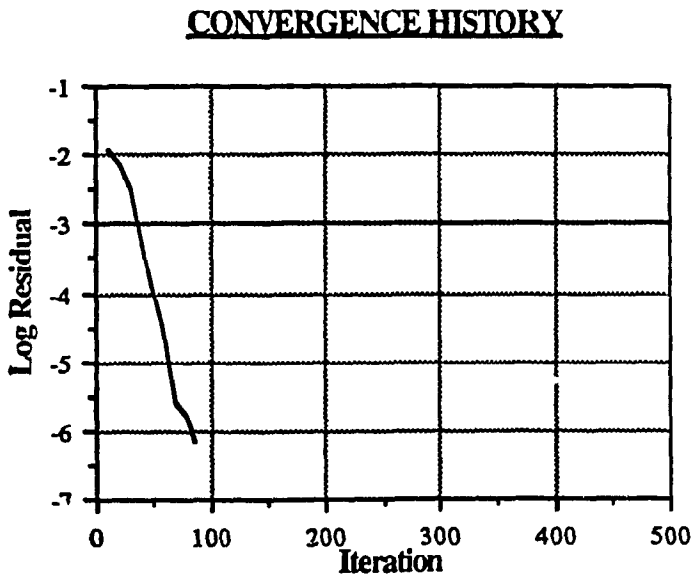

Fig. 8 Convergence history for Lerat's Exact Method subsonic test case

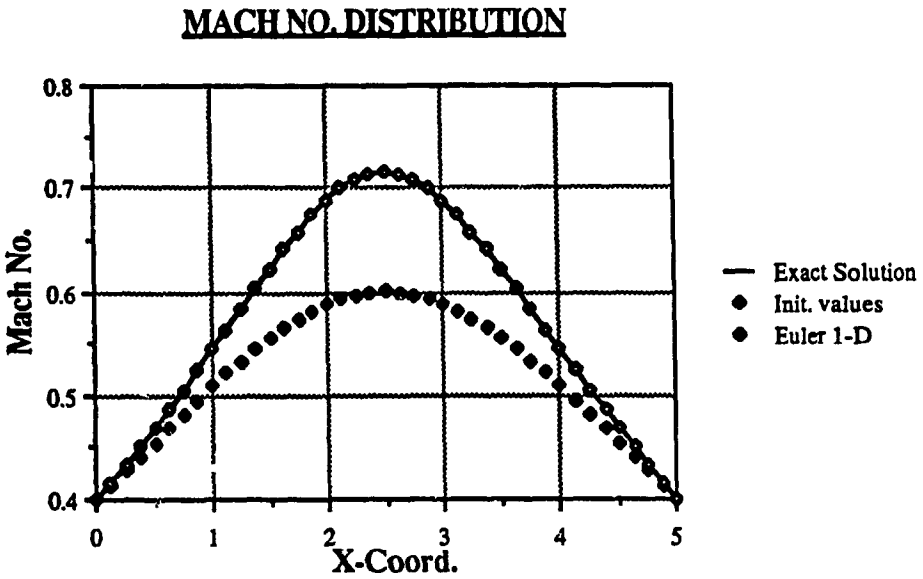

Fig. 9 Lerat's Approximate Method subsonic test case

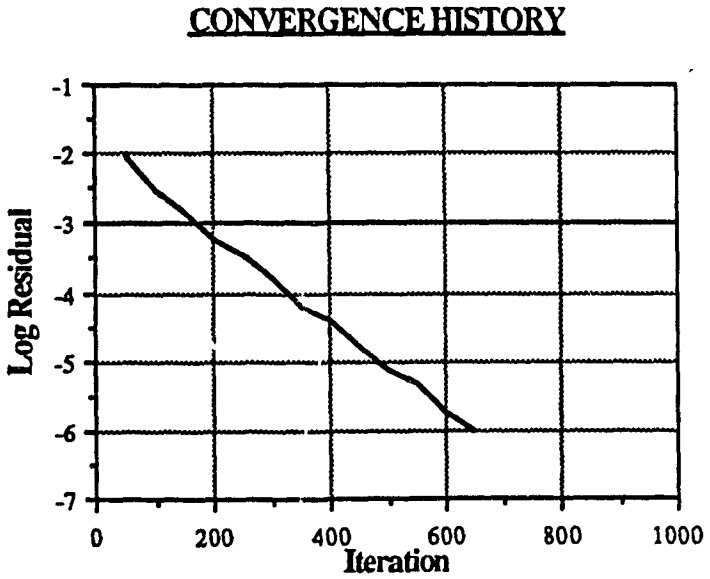

Fig. 10 Convergence history for Lerat's Approximate Method subsonic test case

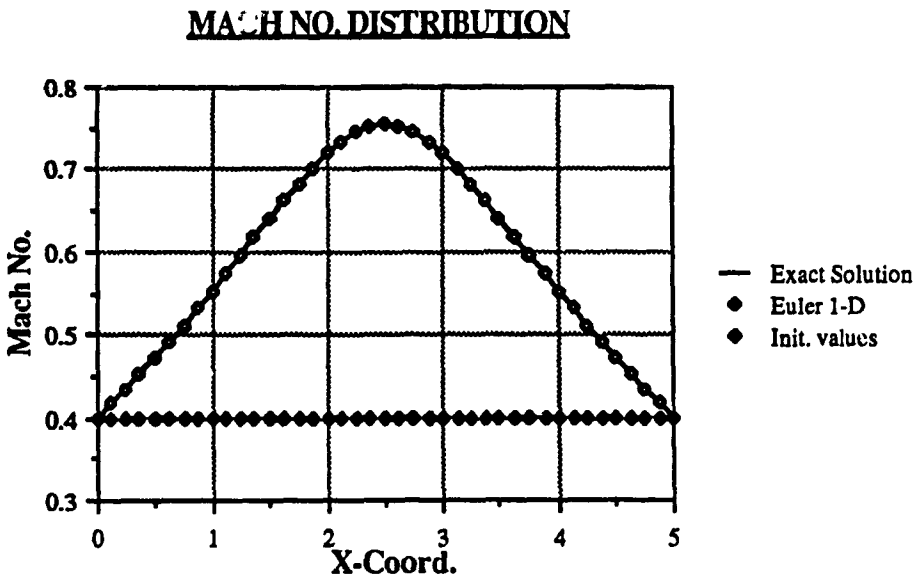

Fig. 11 Newton-Galerkin subsonic test case

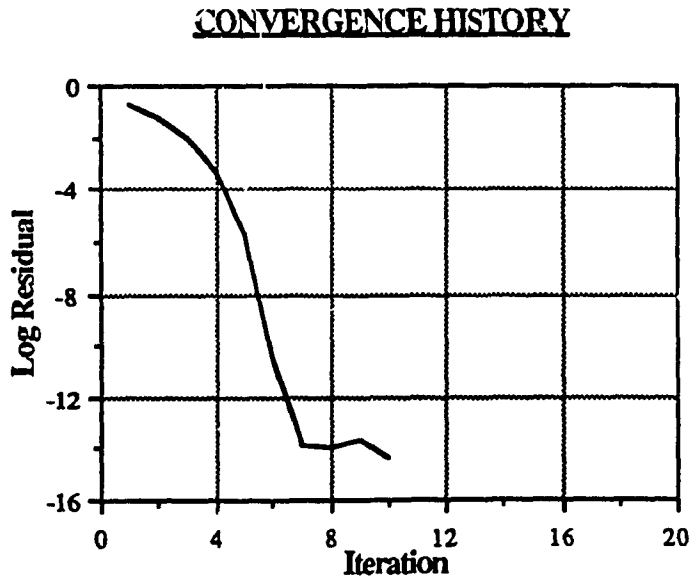

Fig. 12 Convergence history for the Newton-Galerkin subsonic test case

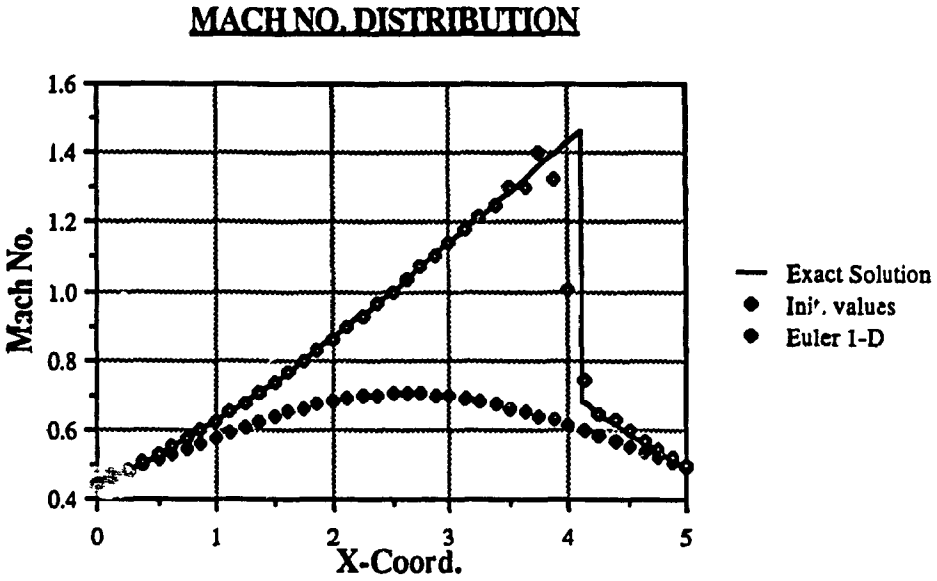

Fig. 13 Taylor-Galerkin transonic test case

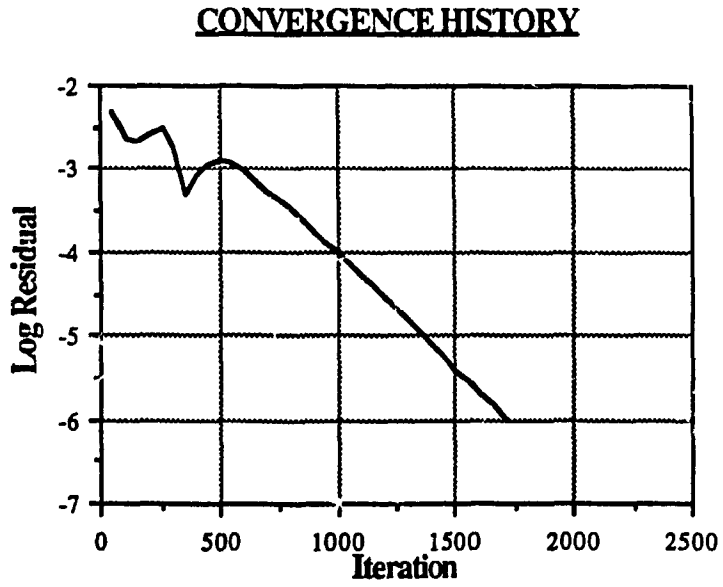

Fig. 14 Convergence history for the Taylor-Galerkin transonic test case

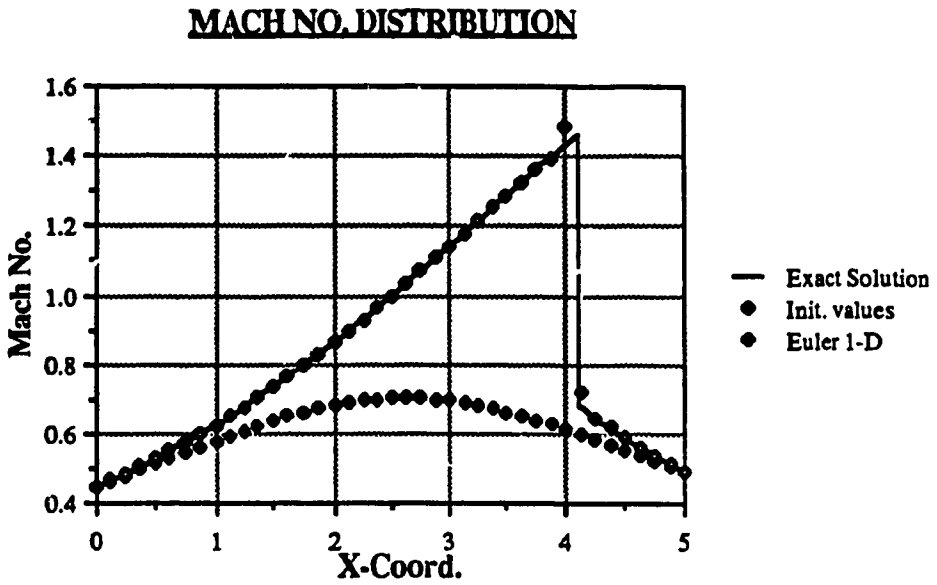

Fig. 15 Lerat's Approximate Method transonic test case

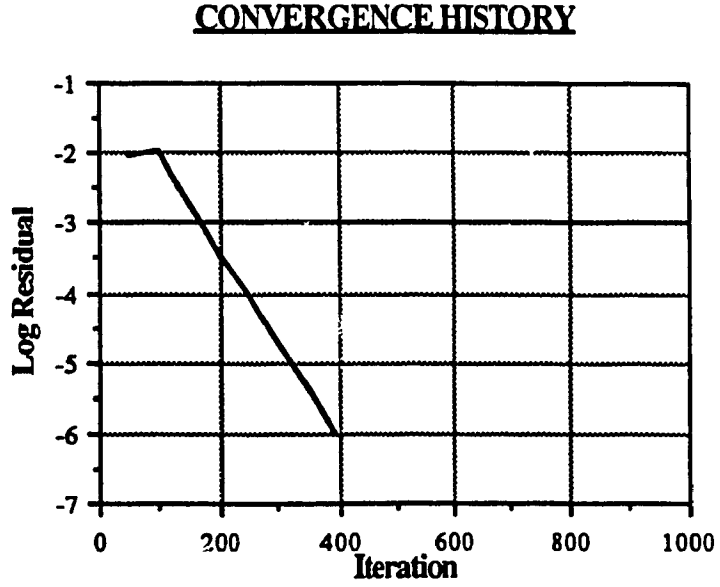

Fig. 16 Convergence history for Lerat's Approximate Method transonic test case

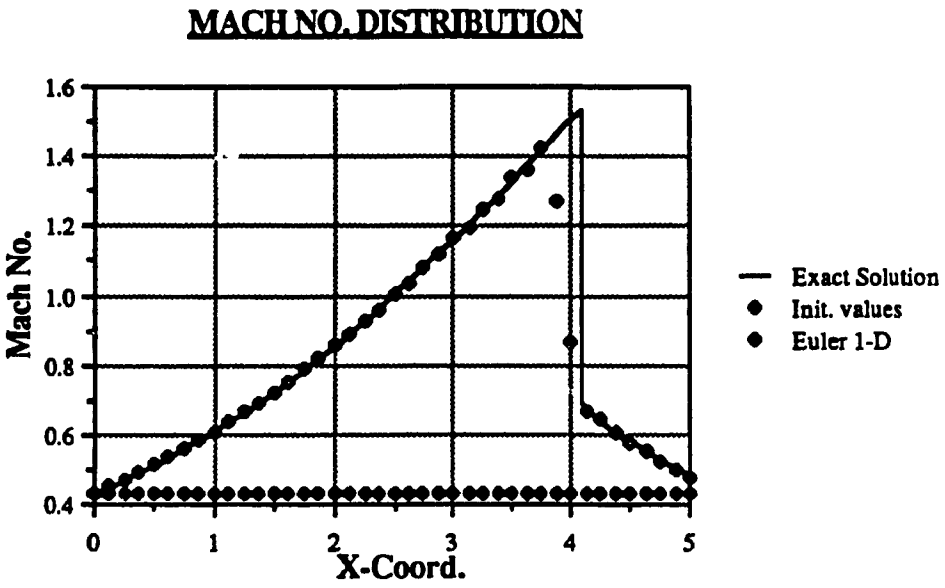

Fig. 17 Newton-Galerkin transonic test case

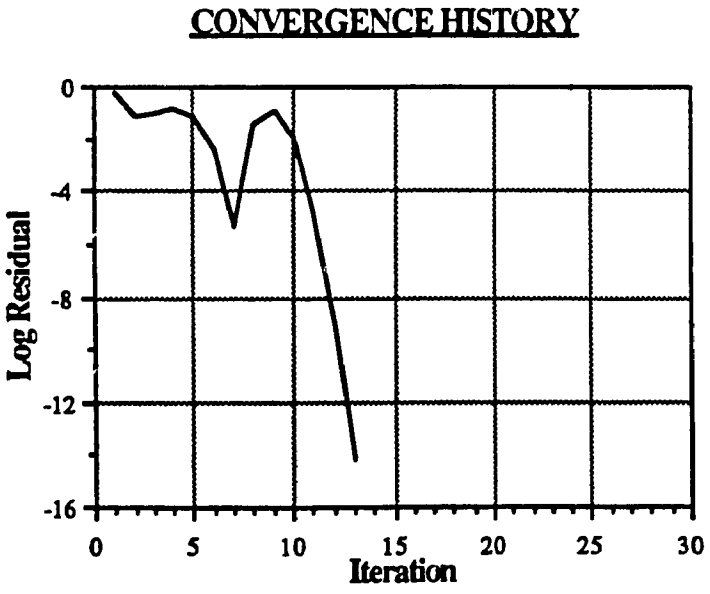

Fig. 18 Convergence history for the Newton-Galerkin transonic test case

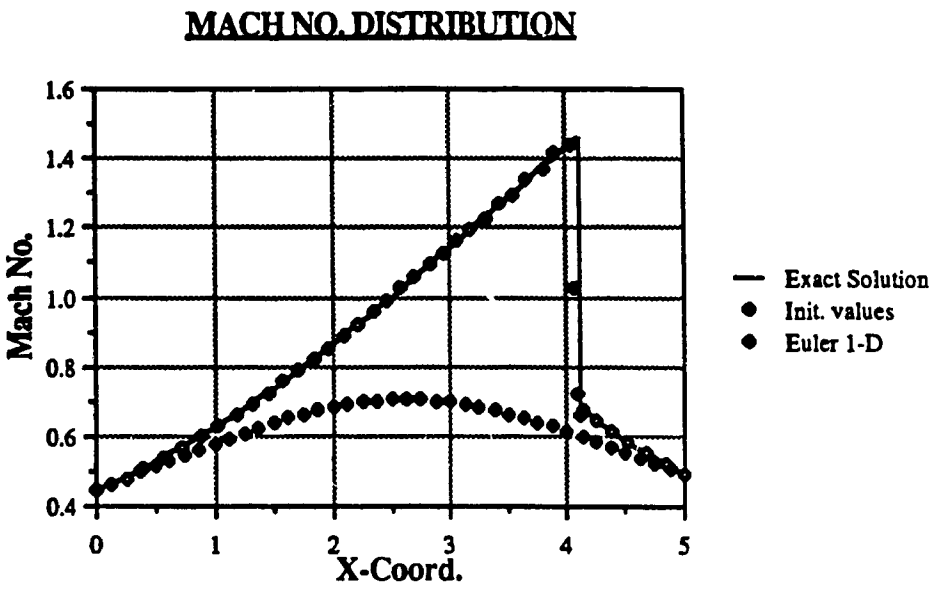

Fig. 19 Influence of mesh refinement on the Taylor-Galerkin scheme

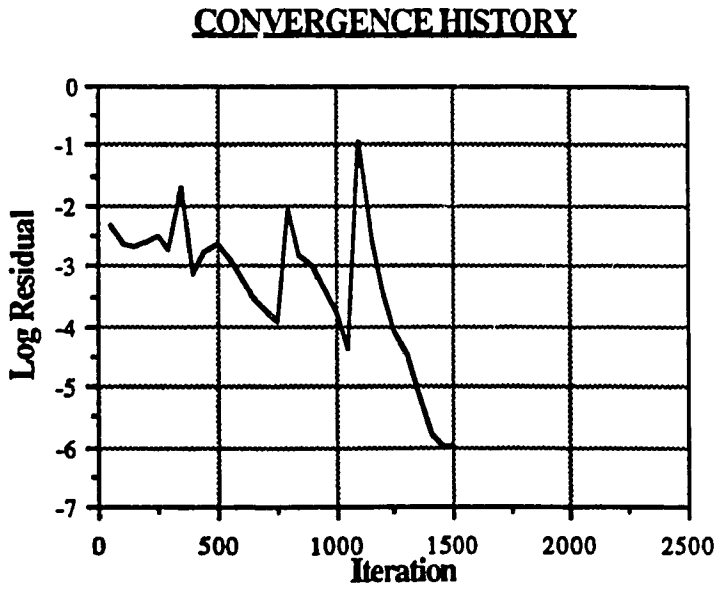

Fig. 20 Convergence history for the Taylor-Galerkin mesh adapting test case

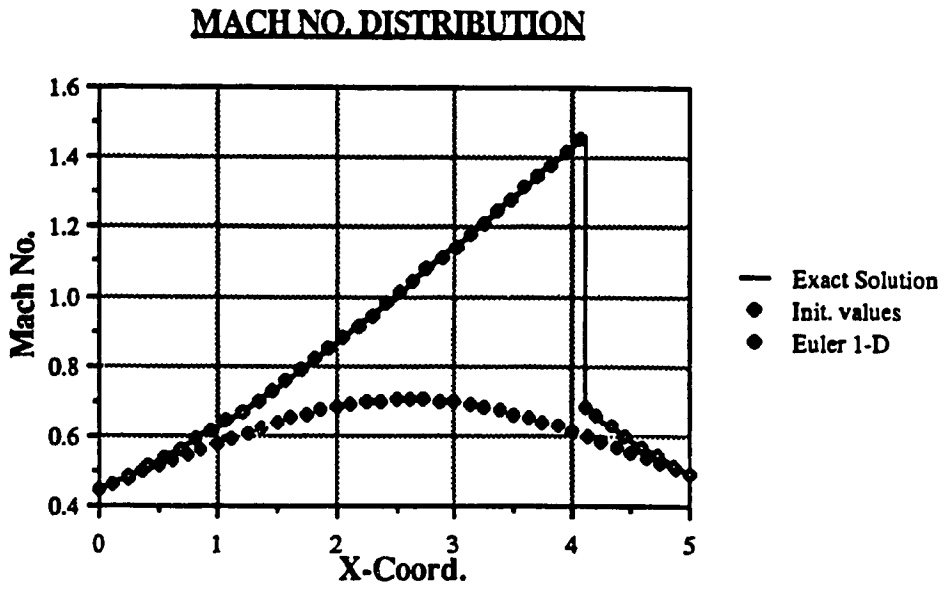

Fig. 21 Influence of mesh adapting on Lerat's Approximate Method

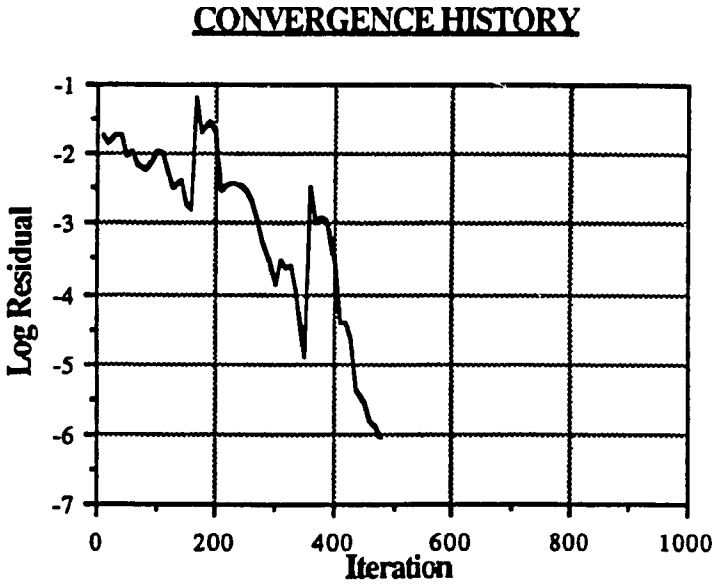

Fig. 22 Convergence history for Lerat's Approximate Method mesh adapting test case

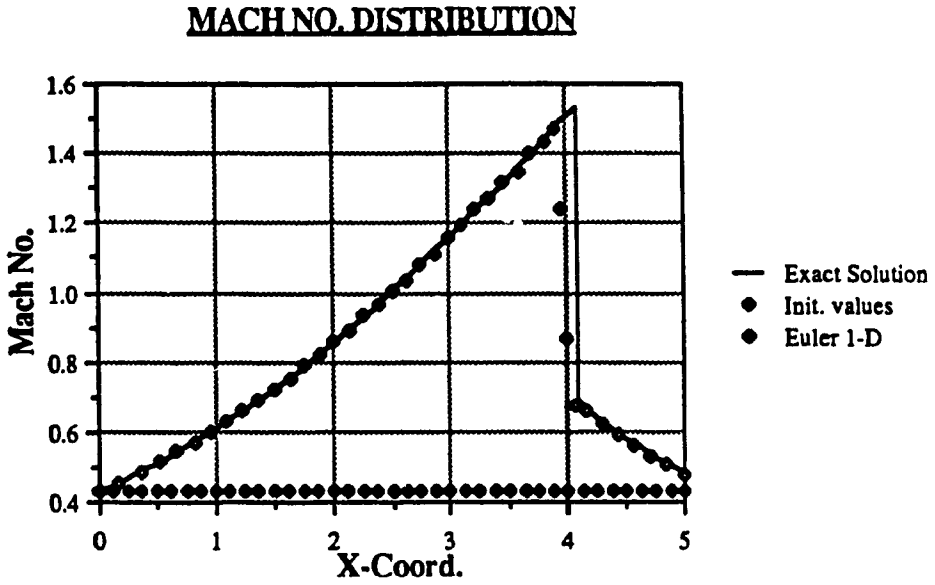

Fig. 23 Influence of mesh adapting on the Newton-Galerkin scheme

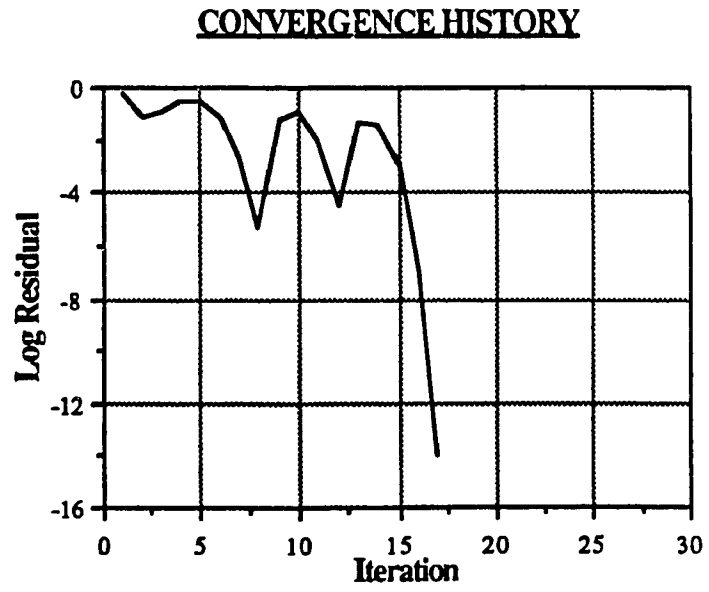

Fig. 24 Convergence history for the Newton-Galerkin mesh adapting test case

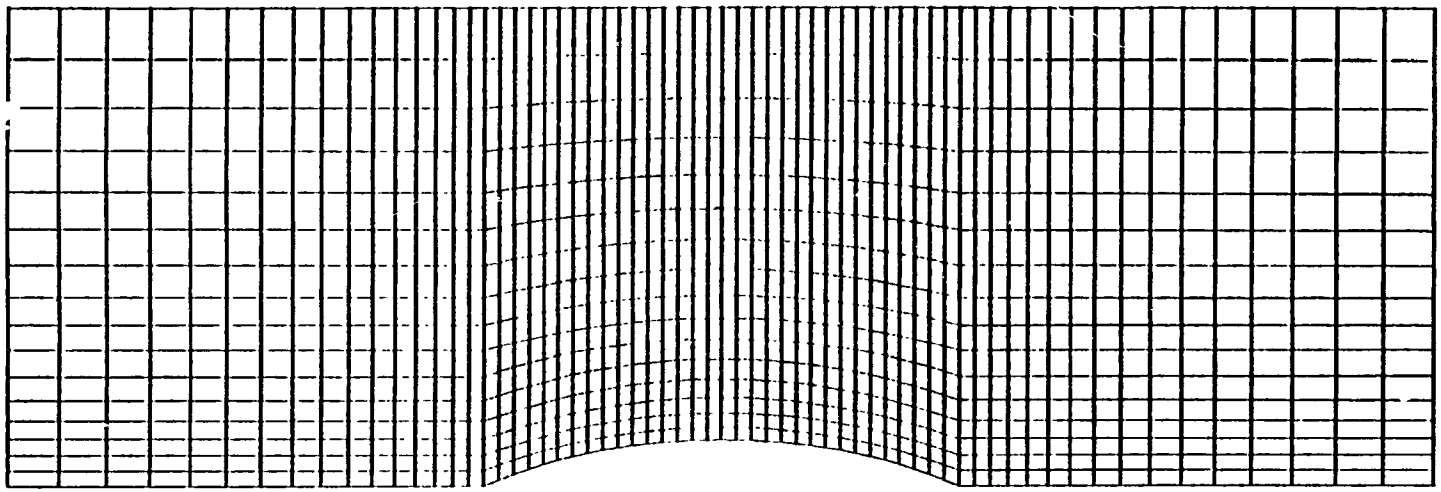

Fig. 23 Finite element grid for a channel with a 10% circular arc bump

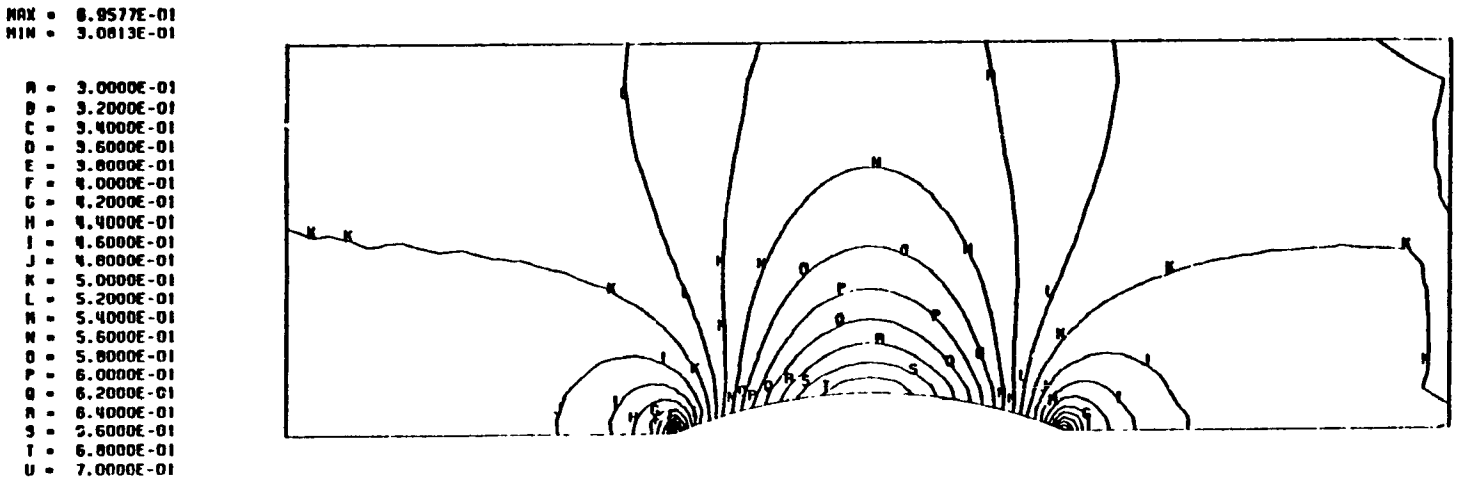

Fig. 26 Mach number contours for subsonic flow in a channel

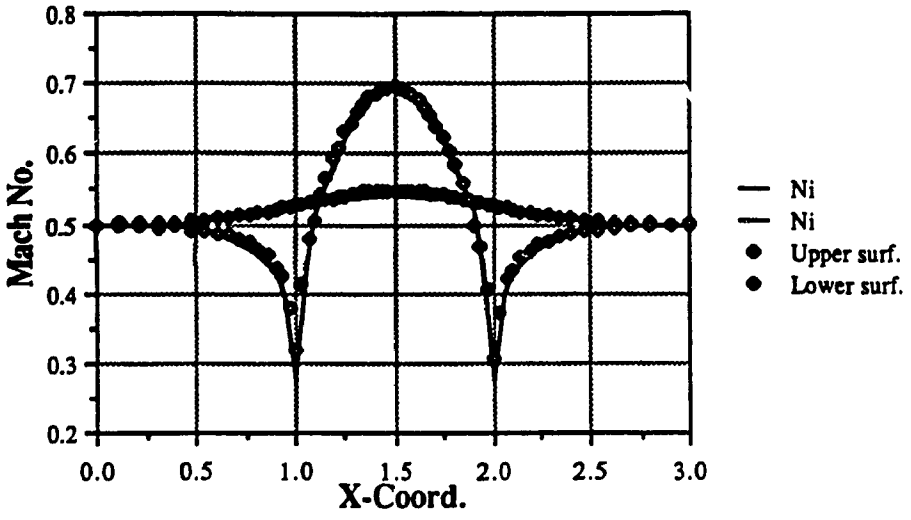

Fig. 27 Mach number distribution for subsonic flow in a channel

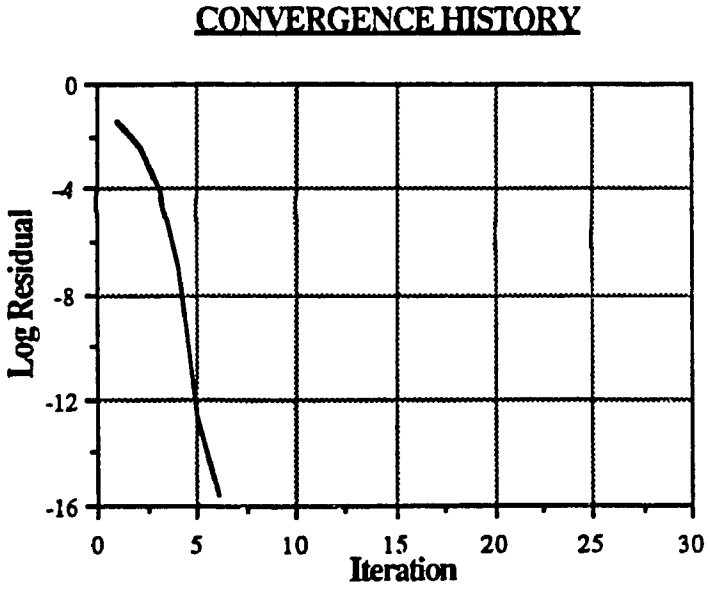

Fig. 28 Convergence history for subsonic flow in a channel

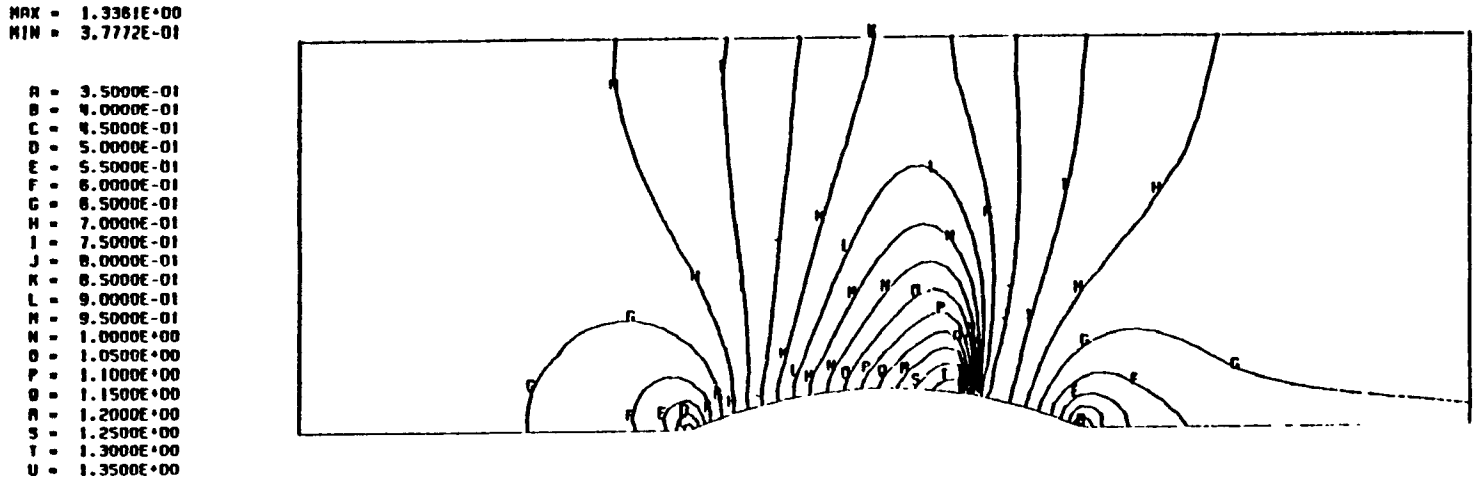

Fig. 29 Mach number contours for transonic flow in a channel

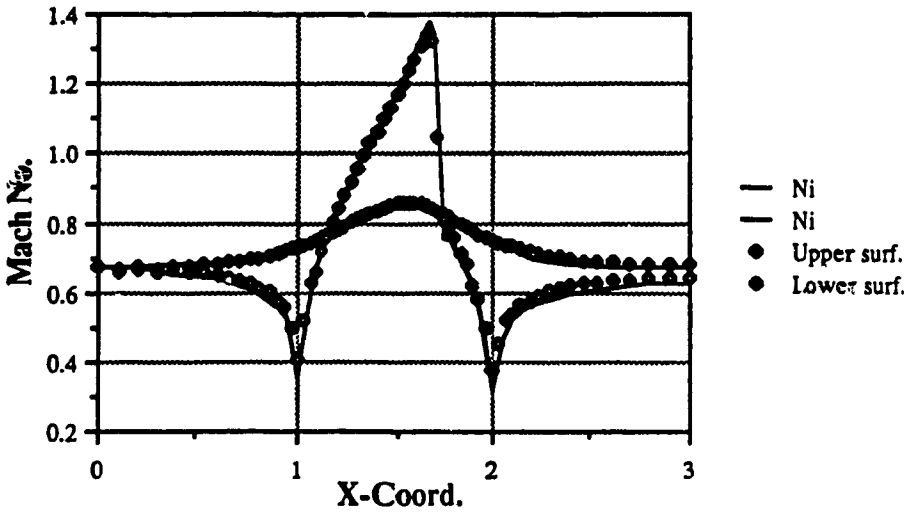

Fig. 30 Mach number distribution for transonic flow in a channel

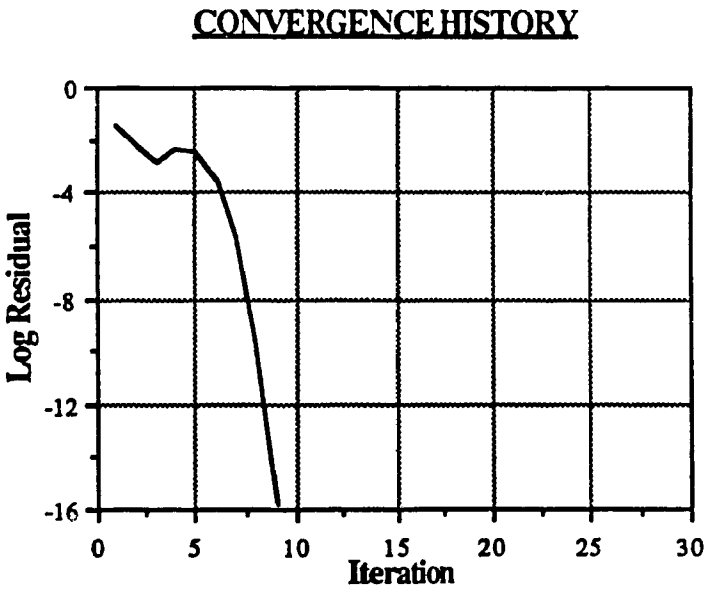

Fig. 31 Convergence history for transonic flow in a channel

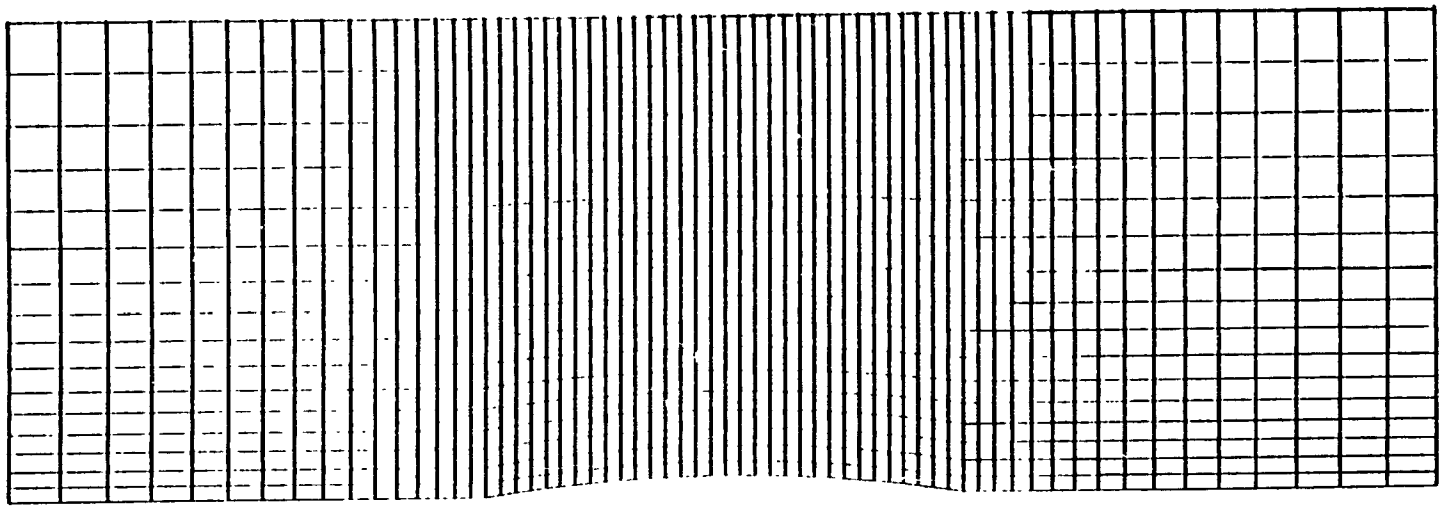

Fig. 32 Finite element grid for a channel with a 4% circular arc bump

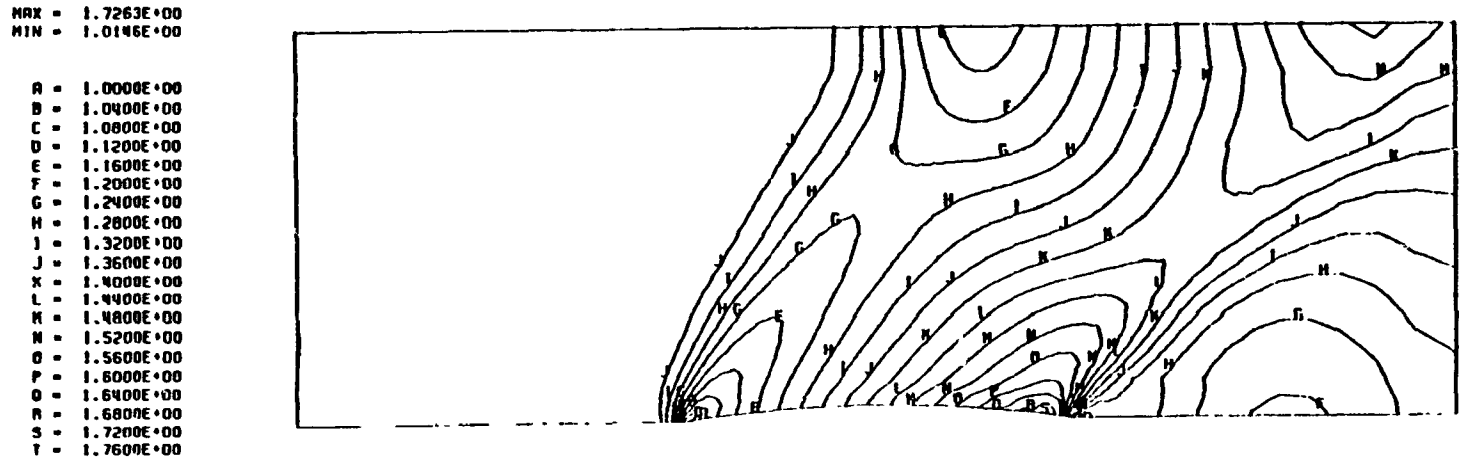

Fig. 33 Mach number contours for supersonic flow in a channel

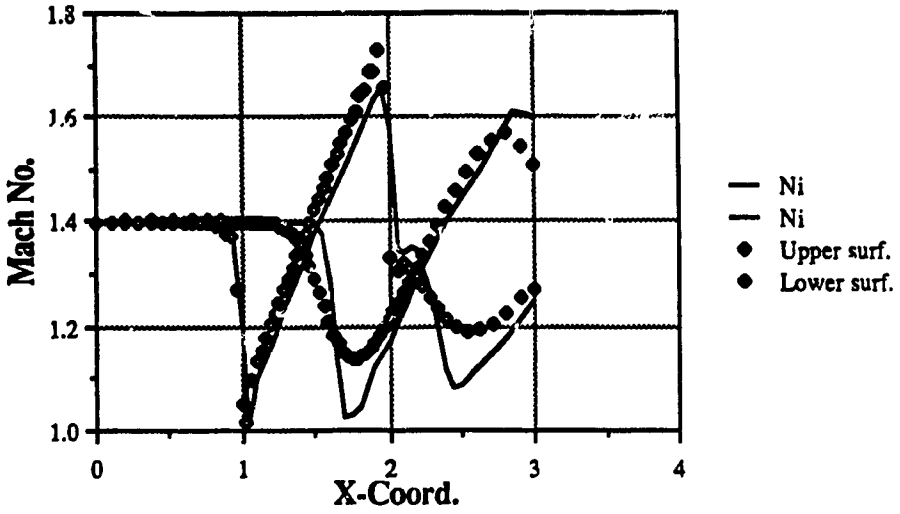

Fig. 34 Mach number distribution for supersonic flow in a channel

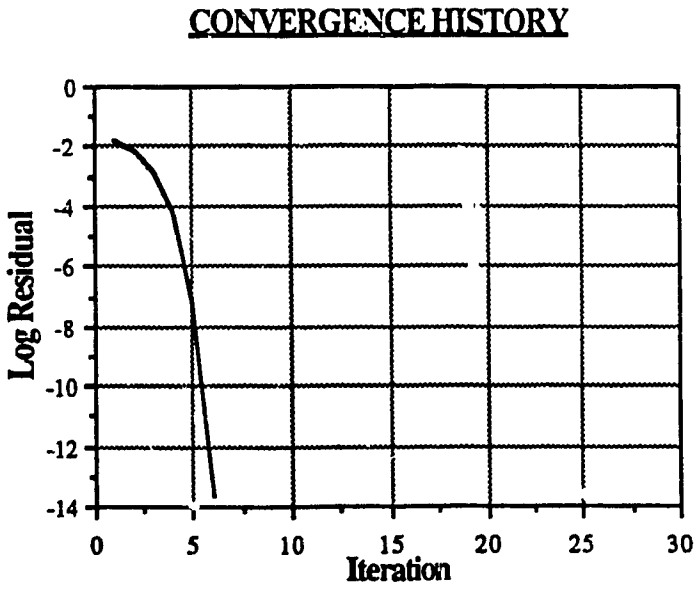

Fig. 35 Convergence history for supersonic flow in a channel

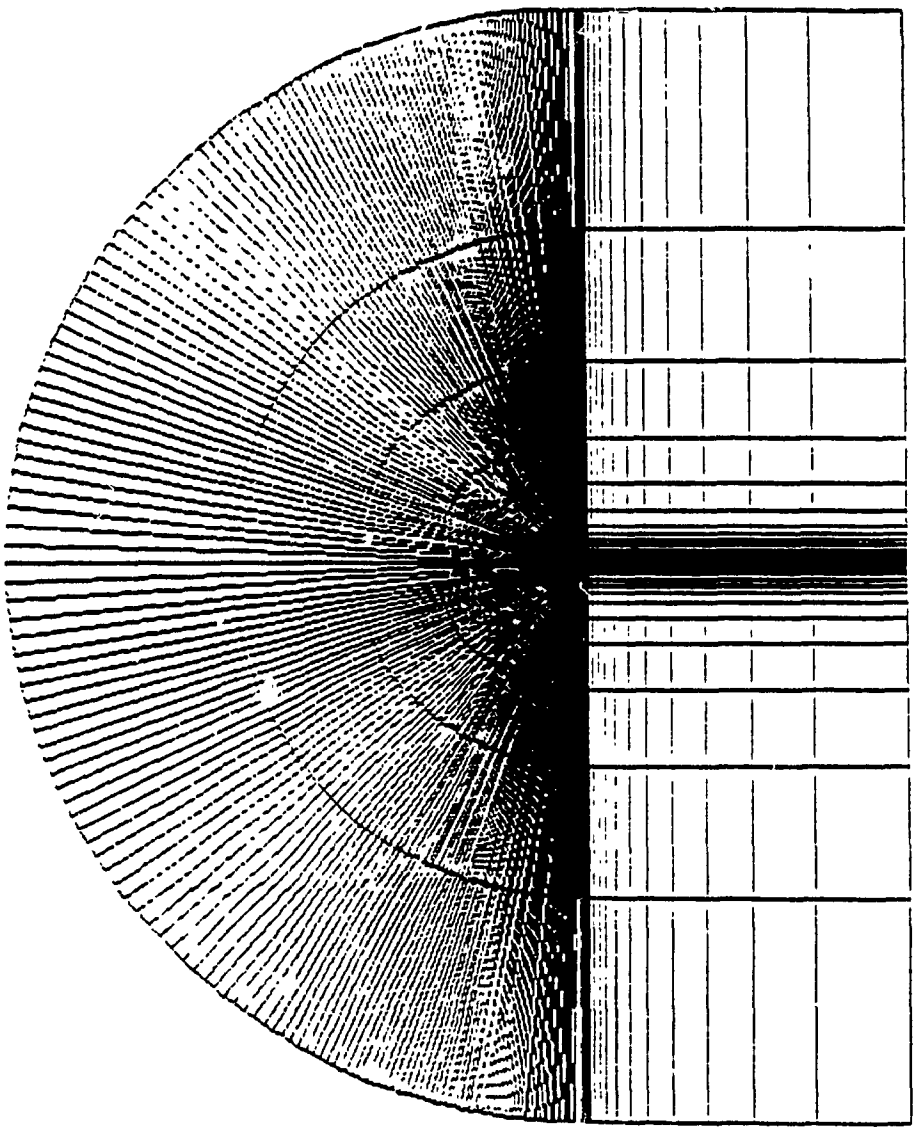

Fig. 36 Finite element grid around a NACA 0012 airfoil

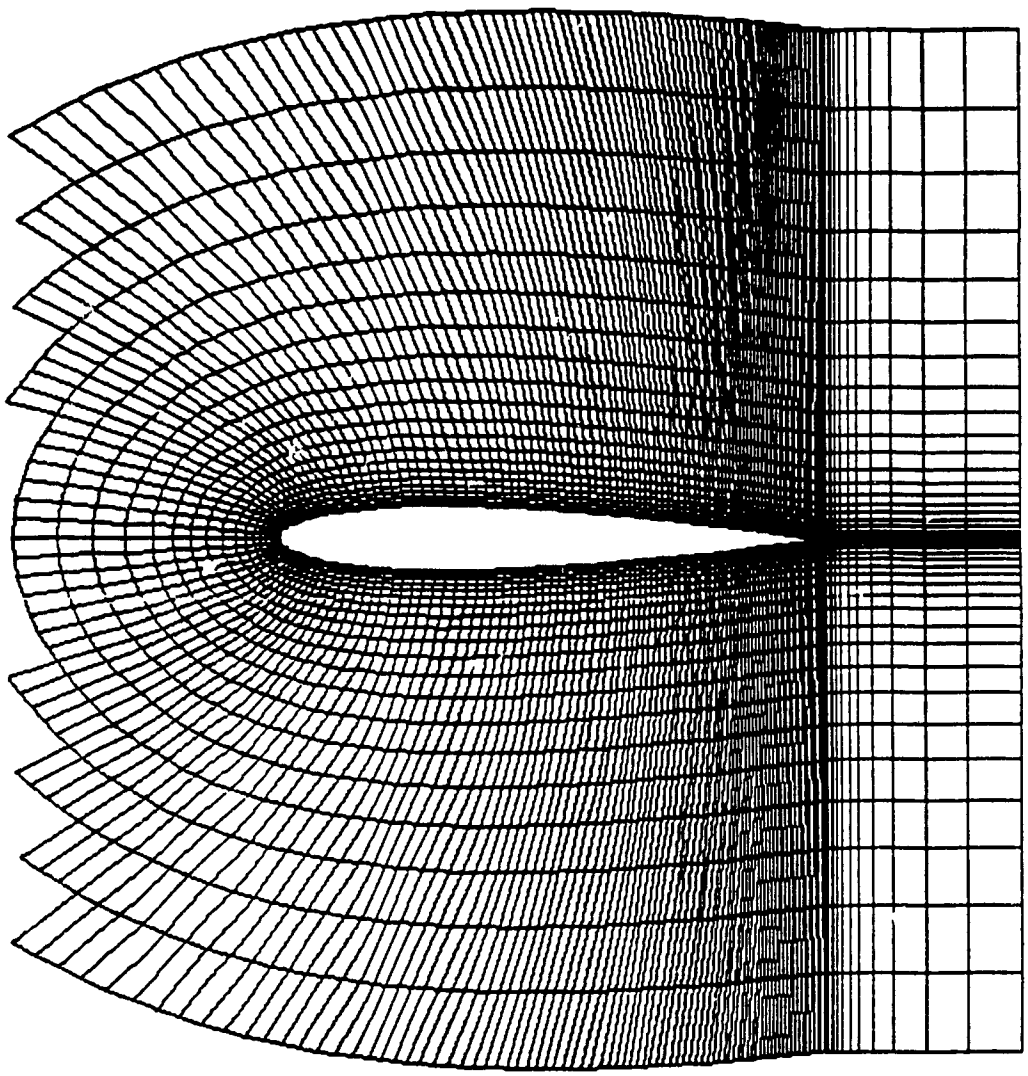

Fig. 37 Detail of the finite element grid around a NACA 0012 airfoil

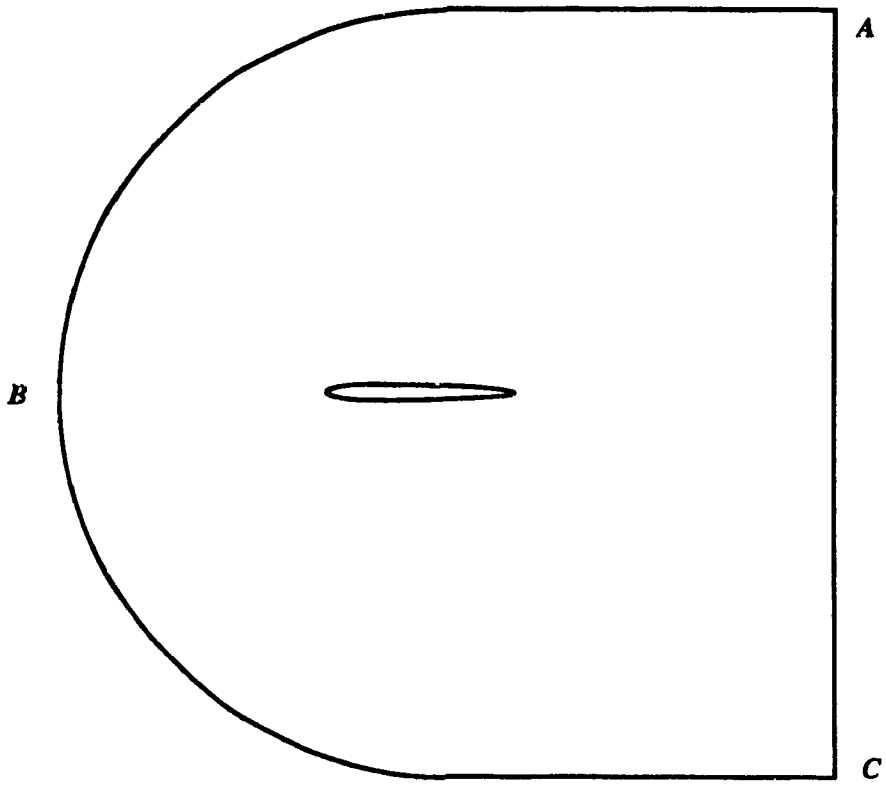

Fig. 38 Schematic C-grid

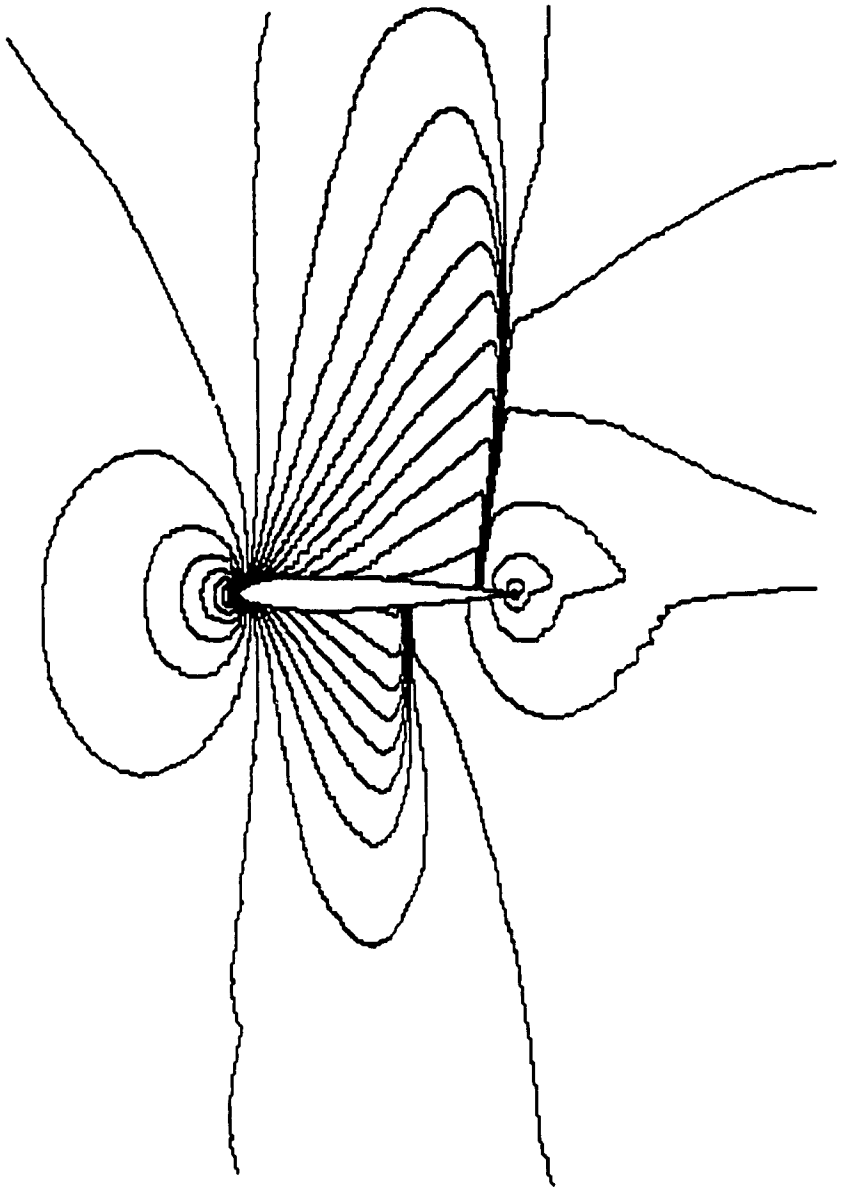

Fig. 39 Mach number contours for the AGARD02 test case

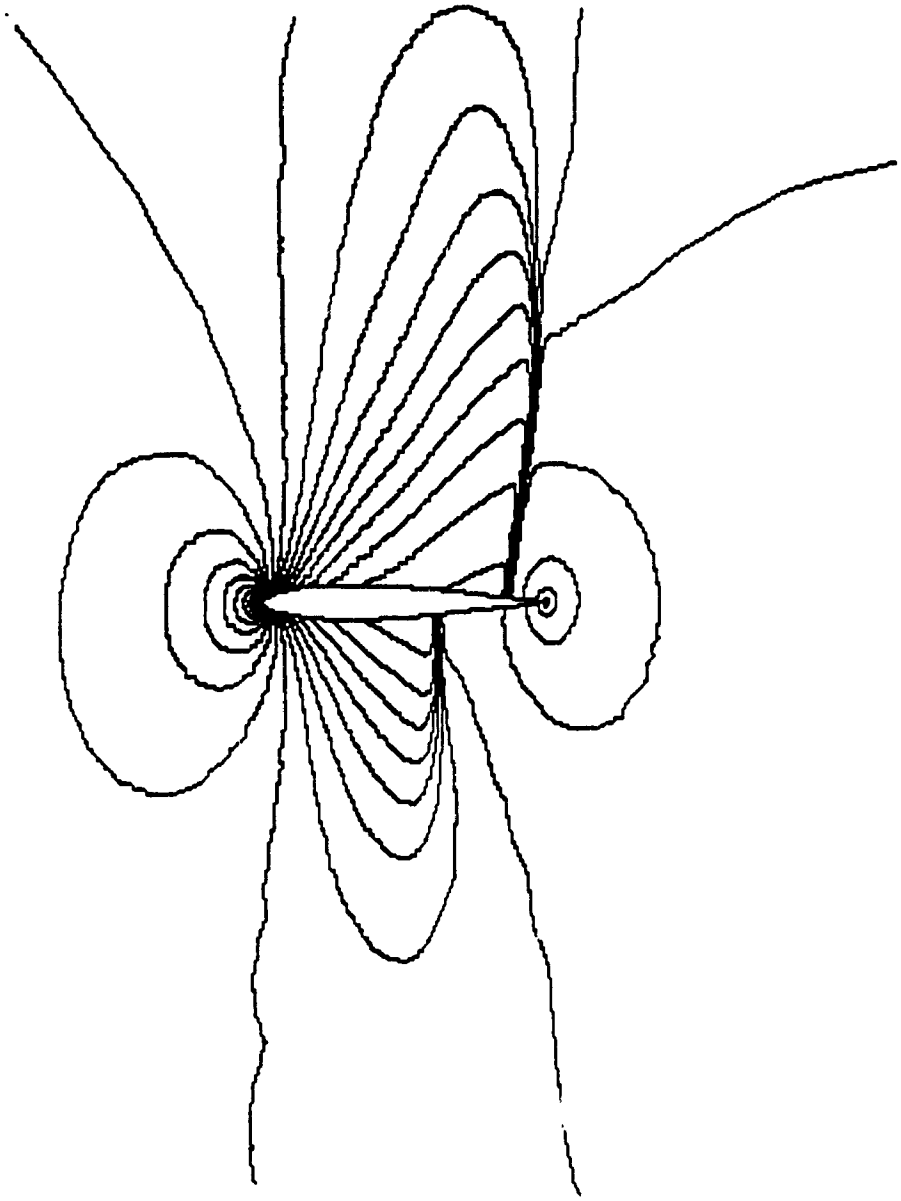

Fig. 40 Constant pressure contours fo the AGARD02 test case

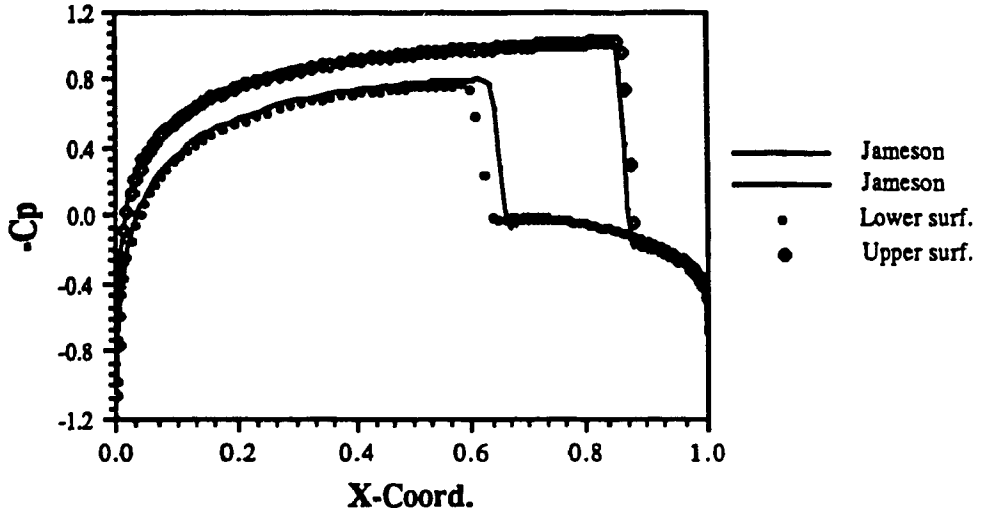

Fig. 41 Comparison of Cp with Jameson's results

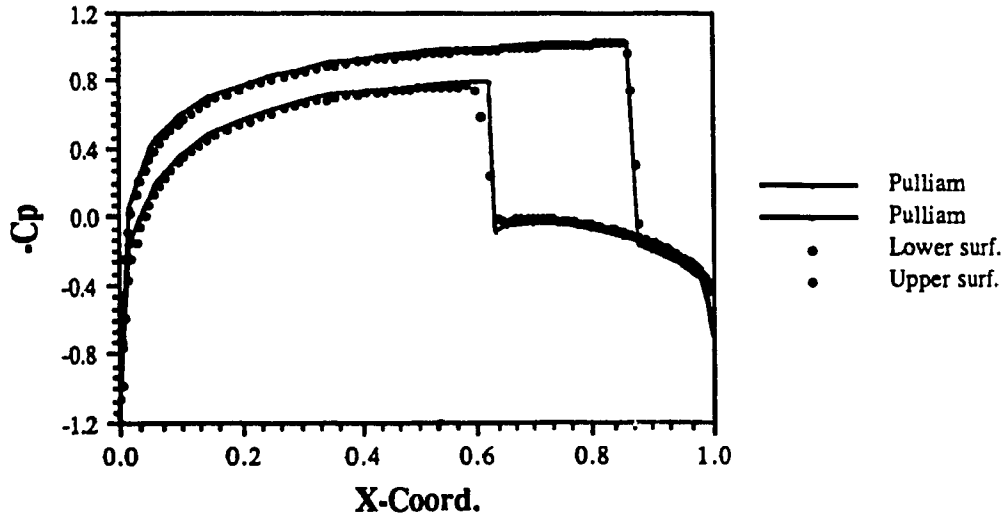

Fig. 42 Comparison of Cp with Pulliam's results

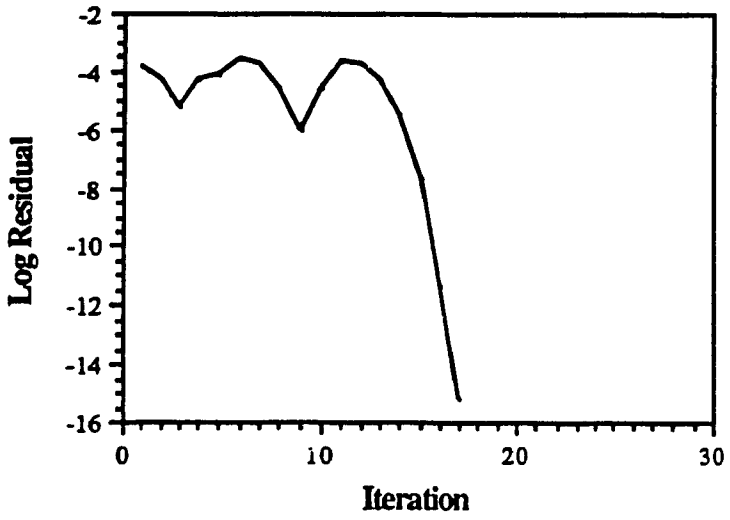

Fig. 43 Convergence curve for the AGARD02 test case

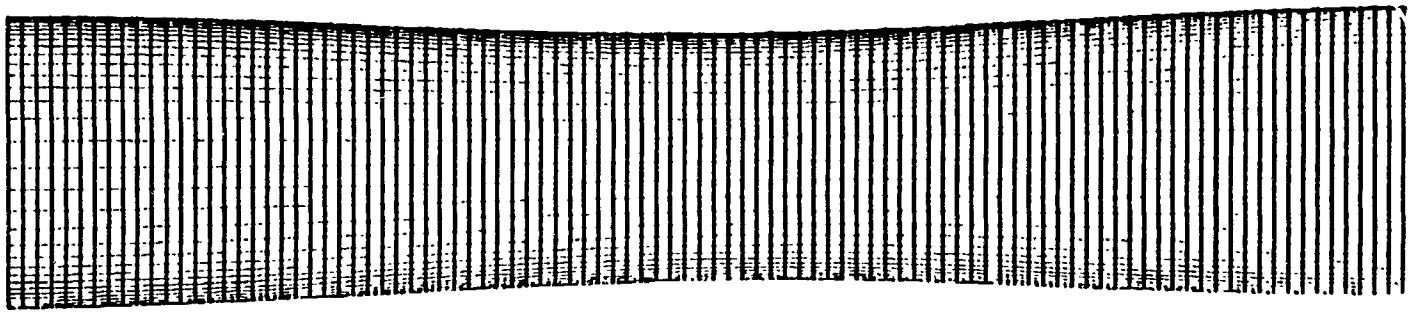

Fig. 44 Finite element mesh for a converging-diverging duct

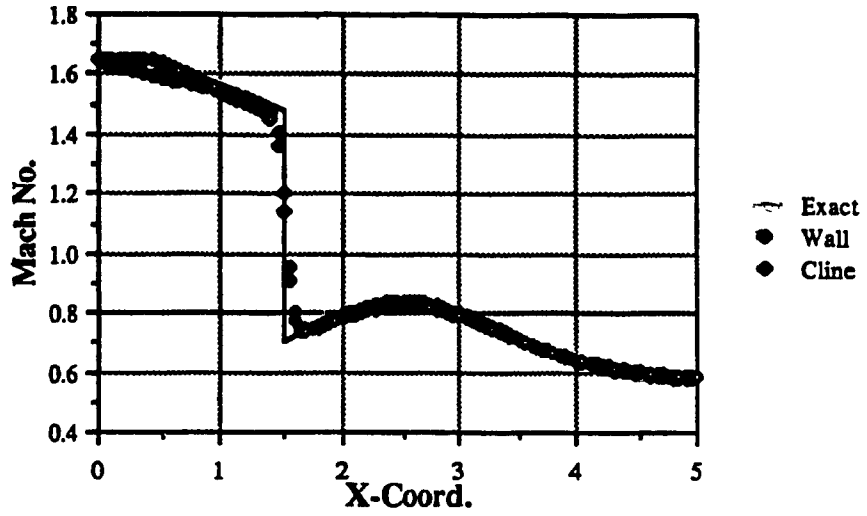

Fig. 45 Mach number distribution for a shock in the converging section

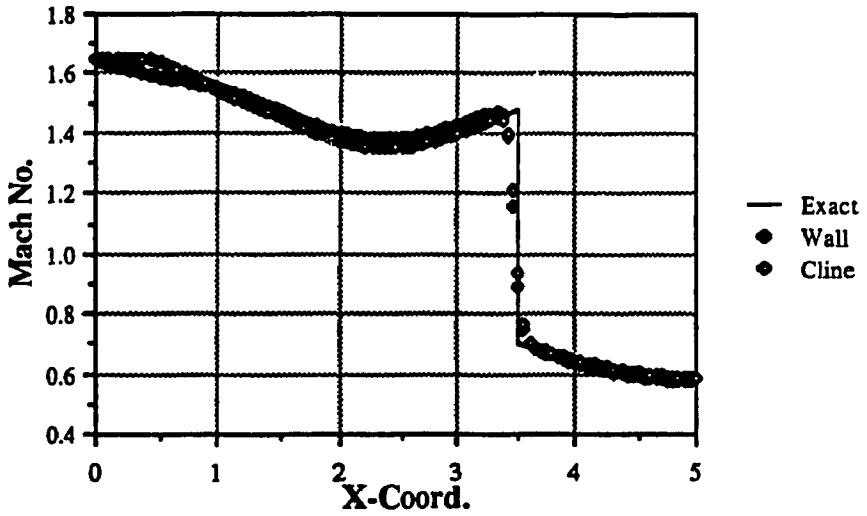

Fig. 46 Mach number distribution for a shock in the diverging section

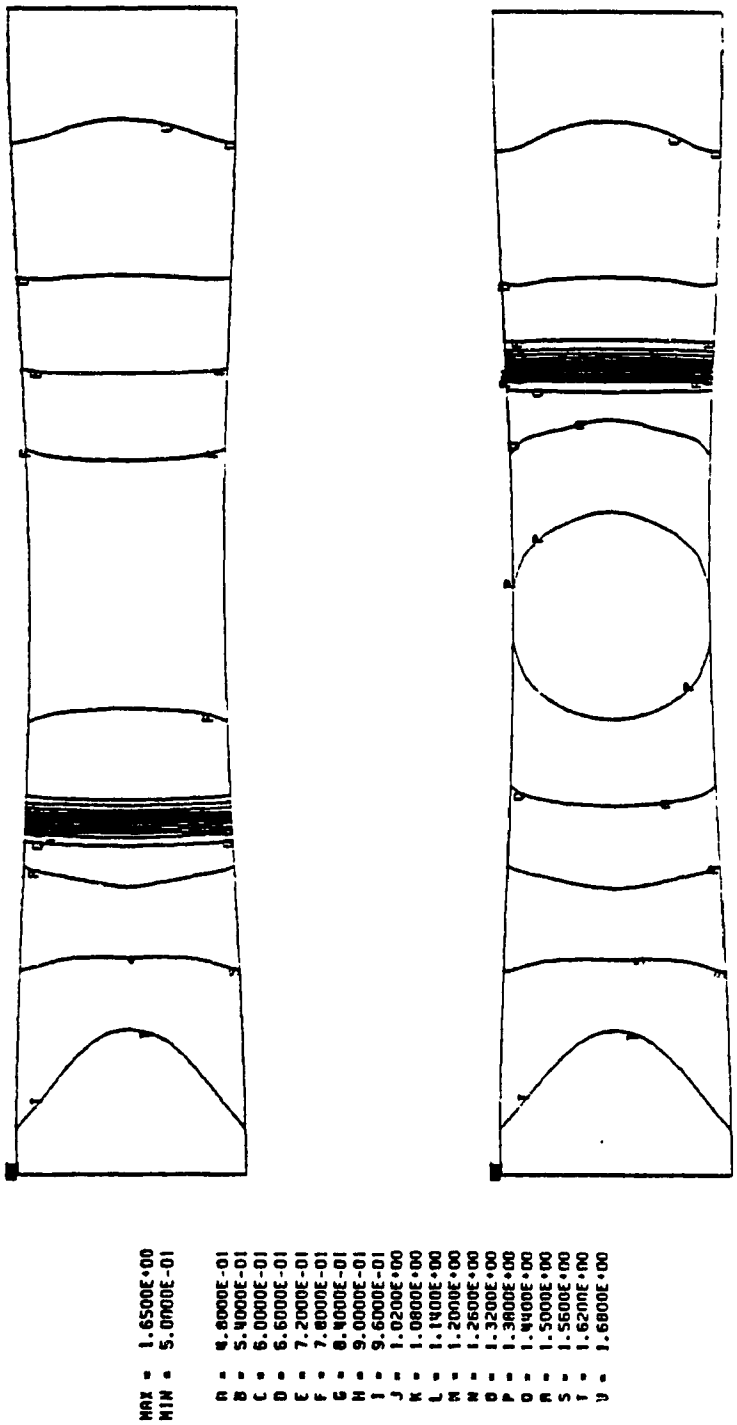

Fig. 47 Mach number contours for the non-unique solutions

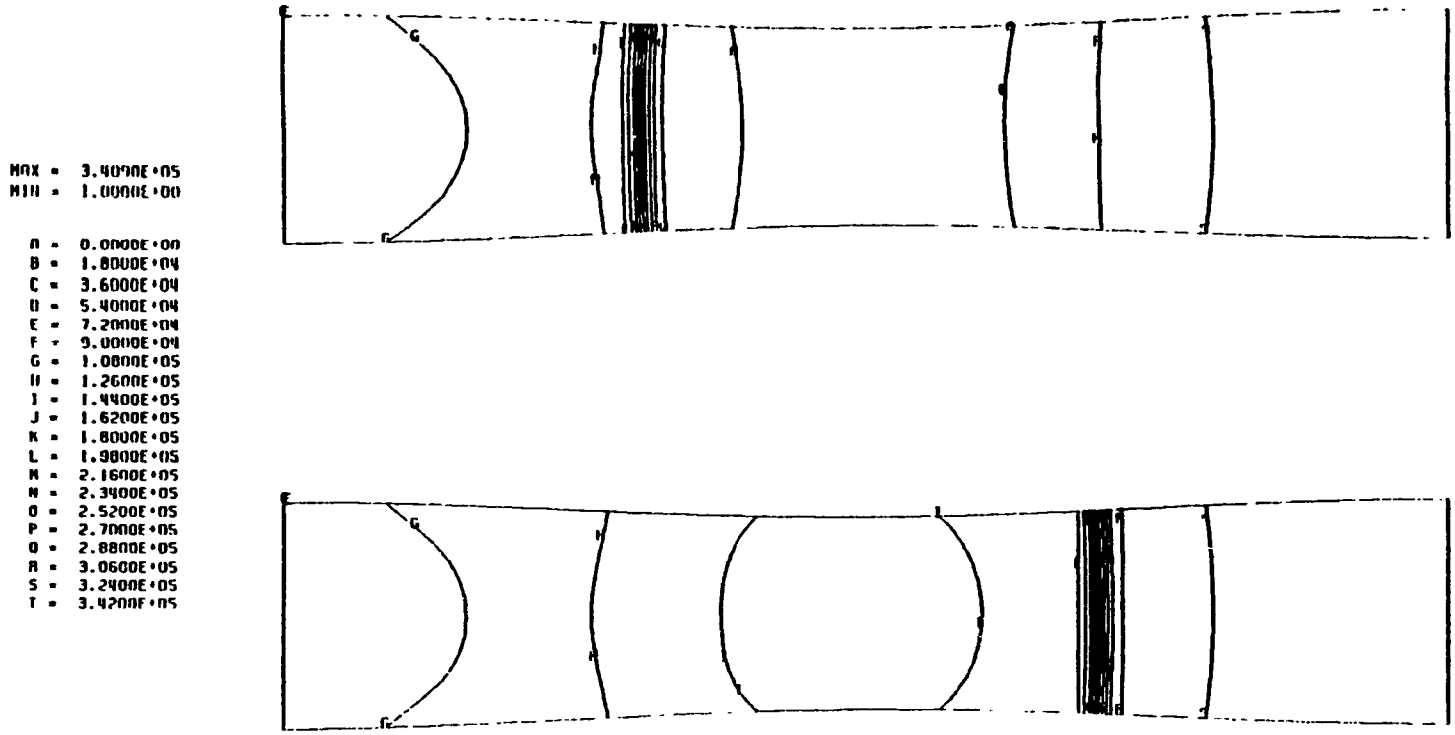

Fig. 48 Pressure contours for the non-unique solutions

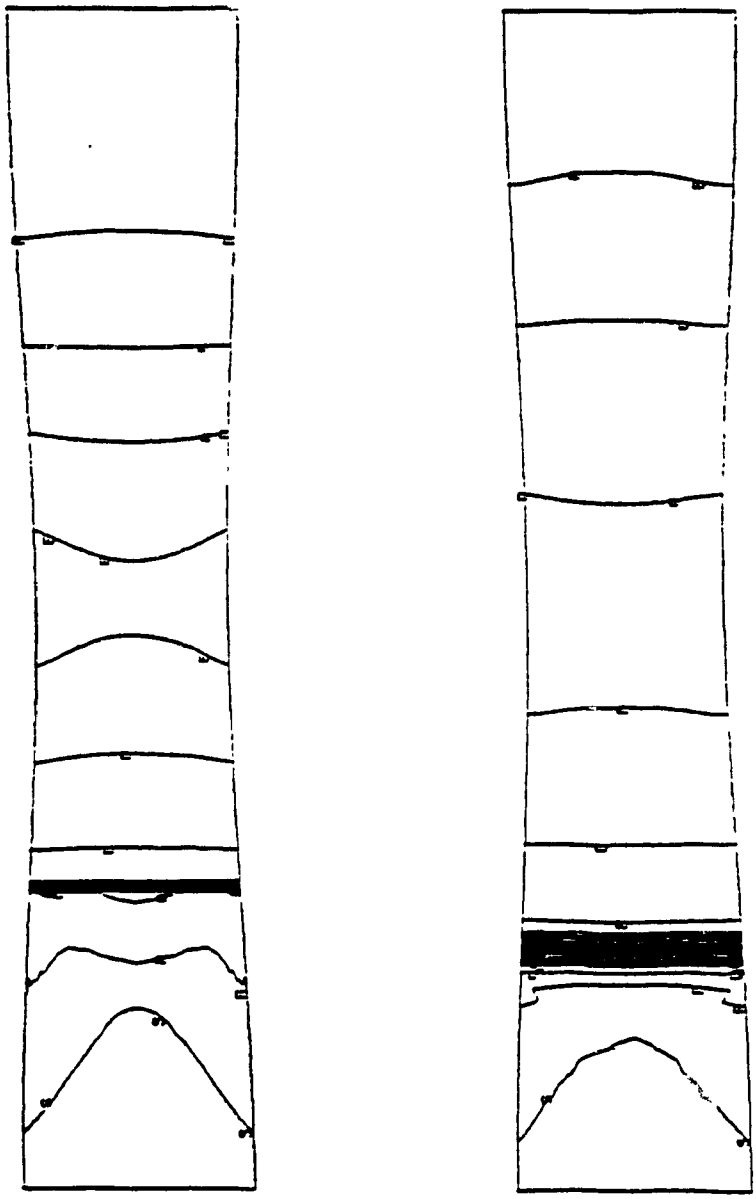

Fig. 49 Unstable shock expelled through the inlet

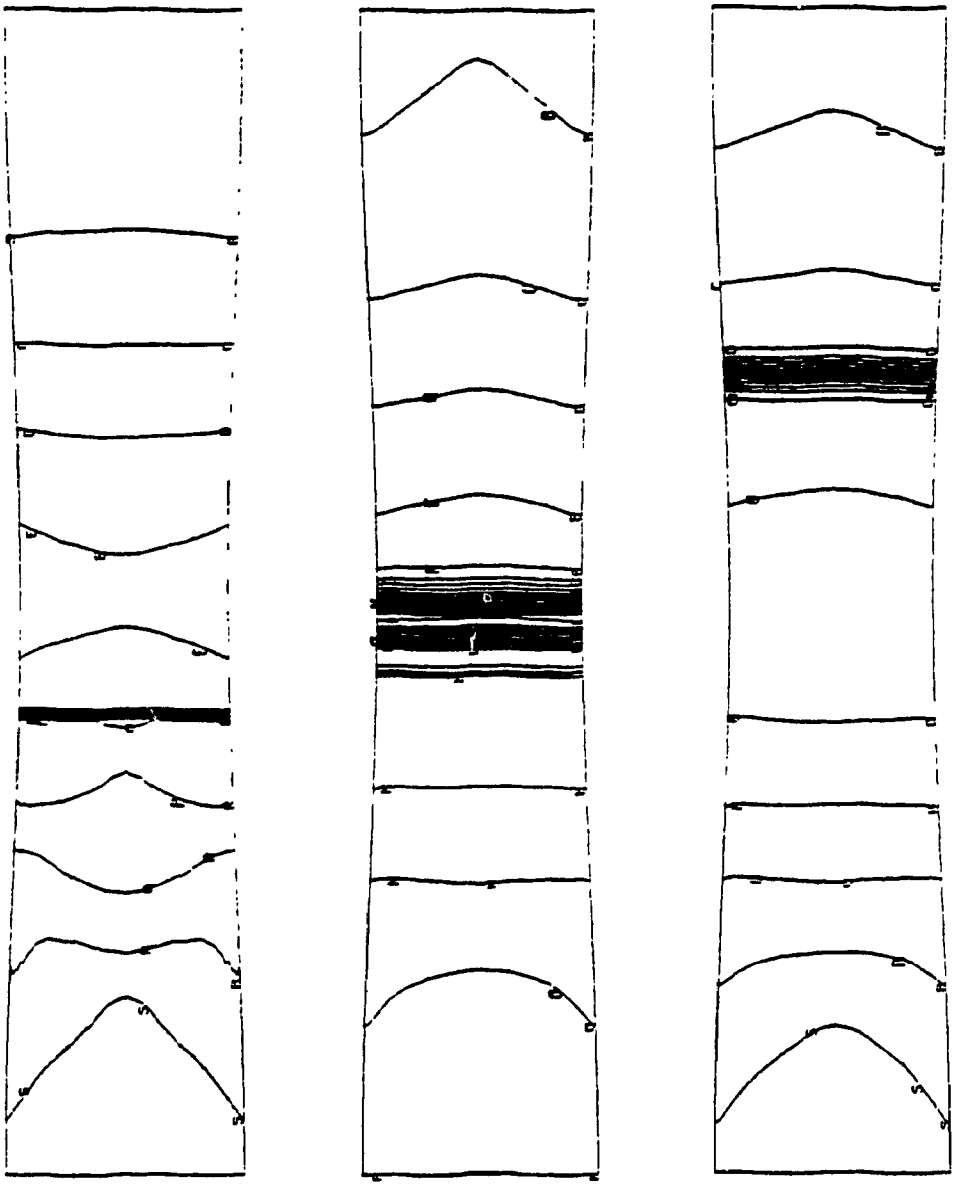

Fig. 50 Unstable shock swallowed through the throat

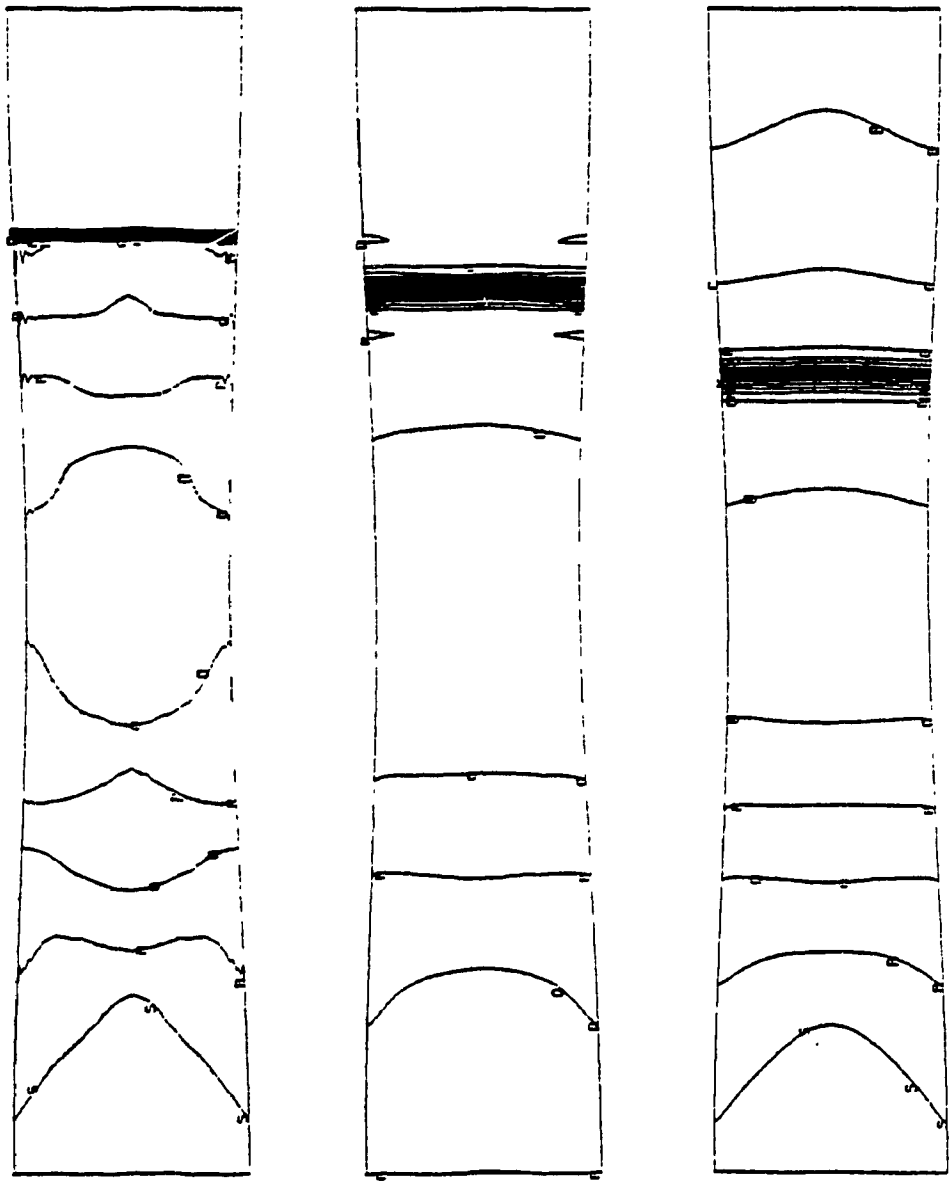

Fig. 51 Shock returning to the stable position

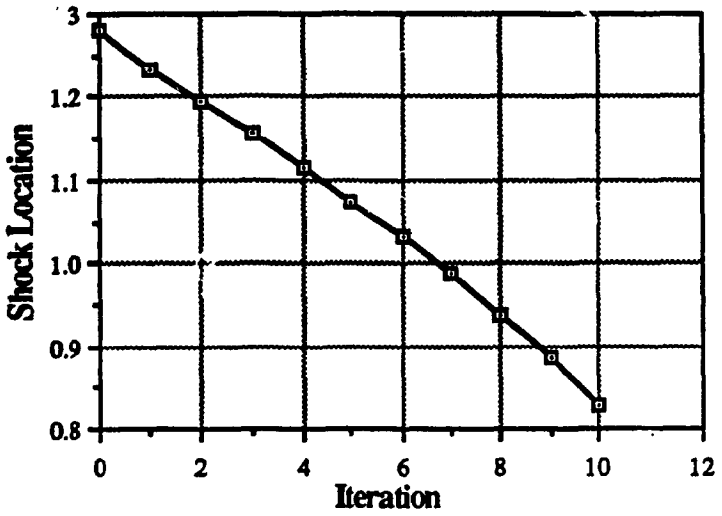

Fig. 52 Correlation between unstable shock location and time step

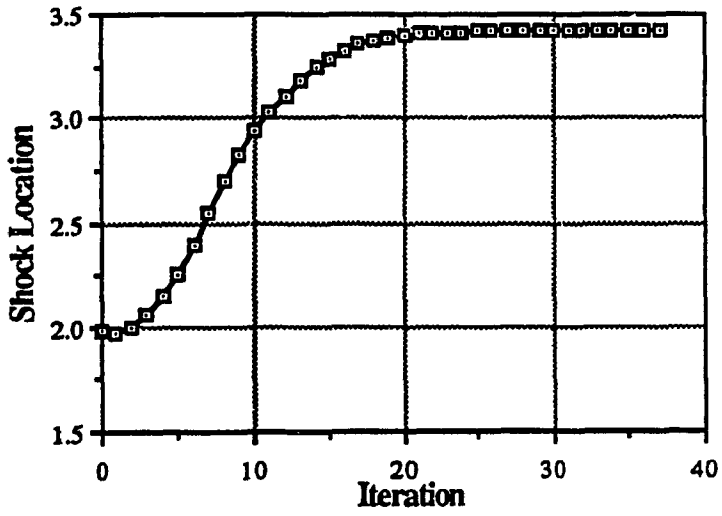

Fig. 53 Correlation between unstable shock location and time step

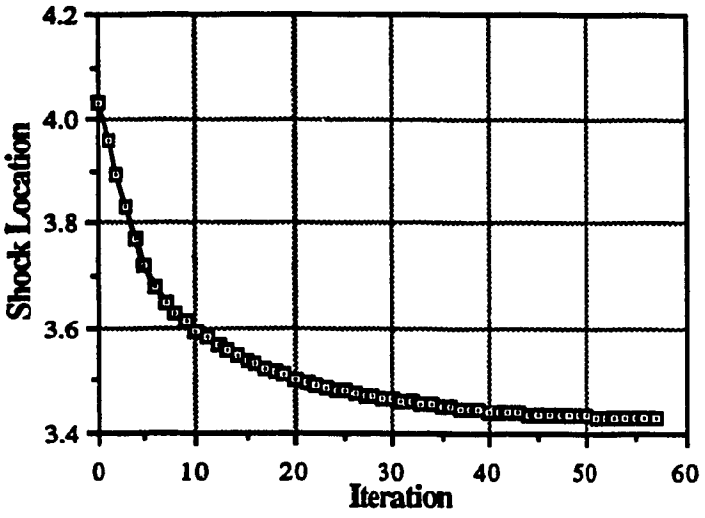

Fig. 54 Correlation between stable shock location and time step

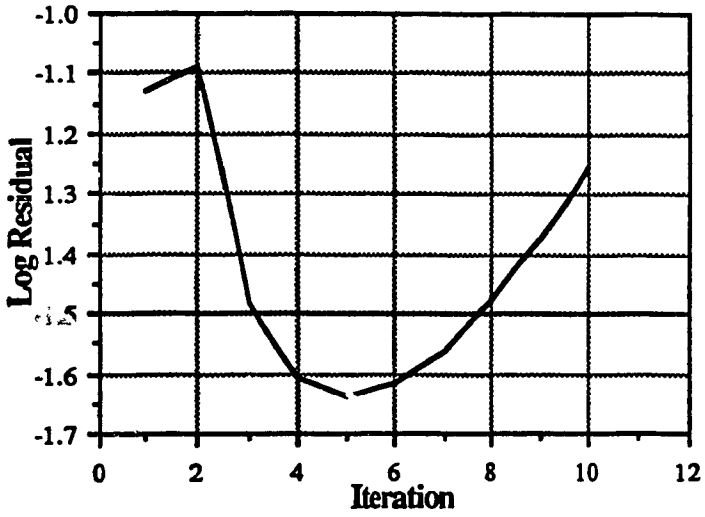

Fig. 55 Correlation between unstable shock residual and time step

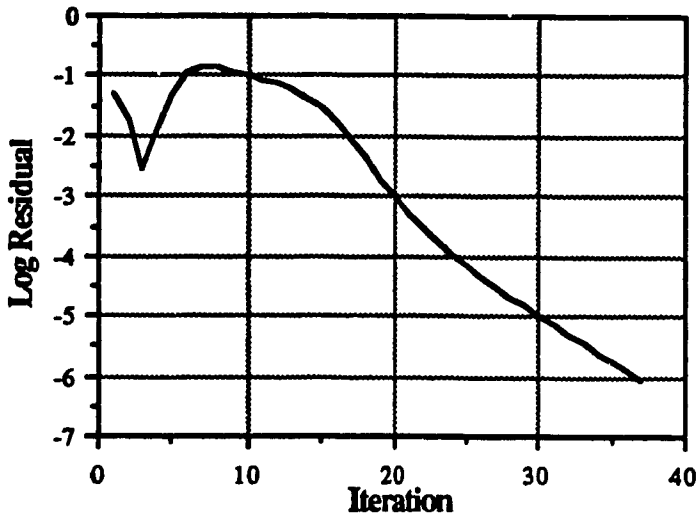

Fig. 56 Correlation between unstable shock residual and time step

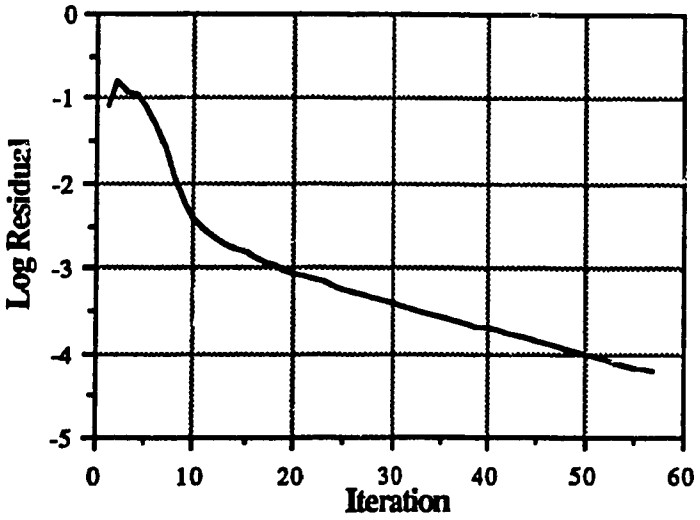

Fig. 57 Correlation between stable shock residual and time step